## *Constraining dark energy using real and mock galaxy surveys*

CAI, YANCHUAN

**Constraining dark energy using real and mock galaxy surveys**

Yanchuan Cai

## Abstract

In this thesis, we study how dark energy may be constrained by measurements of large-scale clustering in future galaxy surveys, and through the imprint of a time-varying large-scale potential on the CMB (the integrated Sachs-Wolfe effect).

We use semi-analytical galaxy formation models implemented in N-body simulations to build mock galaxy catalogues which are well suited for use in conjunction with large photometric surveys. Using mock catalogues, we predict that Pan-STARRS1 will be able to detect $10^8$ galaxies in all its 5 photometric bands. We investigate the photo-$z$ performance of the mock survey, which is a crucial factor when measuring large-scale structure statistics from a survey of this kind. We find using Pan-STARRS1 alone, photo-$z$ accuracy of $\Delta z/(1+z) \sim 0.06$ is achievable. The accuracy can be improved by combining near infrared photometry or by choosing a red galaxy sample. We implemented the photo-$z$ errors to investigate their influence on the detectability of dark energy in the survey via the baryonic acoustic oscillations.

We explore the challenges of using the ISW effect as a constraint on dark energy. In particular, we investigate the effect of non-linear gravitational evolution, using N-body simulations. We have quantified the non-linear contribution to the ISW measurements in terms of both its power spectrum and its cross-correlation with large-scale structure. We have discovered that the non-linear ISW effect is more important relative to the linear ISW effect at larger scales at higher redshifts. This draws attention to the need to accurately model the non-linear effect when using galaxy samples to do ISW tomography at high redshifts. We have developed a ray-tracing method for constructing full sky maps of the ISW effect including its non-linear aspect. Using these maps, we have developed a complete picture of the non-linear ISW effect in void and cluster regions. We quantify the total contribution of the linear and non-linear ISW effects to reported abnormal CMB cold spots and discuss possible confusion with the Sunyaev-Zel'dovich effect.

# Constraining dark energy using real and mock galaxy surveys

by Yanchuan Cai

A thesis submitted to the University of Durham
in accordance with the regulations for
admittance to the Degree of Doctor of Philosophy.

Department of Physics
University of Durham
September 2009

# Contents

# List of Figures

# List of Tables

## Declaration

The work described in this thesis was undertaken between 2006 and 2009 while the author was a research student under the supervision of Professor Carlton Baugh, Professor Shaun Cole, Professor Carlos Frenk, and Dr. Adrian Jenkins in the Department of Physics at the University of Durham. This work has not been submitted for any other degree at the University of Durham or any other University.

Chapter 2 of this thesis has been published in the form of a paper,

- Cai Y-C., Angulo R. E., Baugh C. M., Cole S., Frenk C. S and Jenkins A., "Mock galaxy redshift catalogues from simulations: implications for Pan-STARRS1". 2009, MNRAS, 395, 1185C.

Chapter 3 has been published in the form of a paper,

- Cai, Y.-C., Cole, S., Jenkins, A., and Frenk, C. "Towards accurate modelling of the integrated Sachs-Wolfe effect: the non-linear contribution". 2009, MNRAS, 396, 772C.

Chapter 4 has been submitted in the form of a paper,

- Cai, Y.-C., Cole, S., Jenkins, A., and Frenk, C. "Full-Sky map of the ISW and Rees-Sciama effect from Gpc simulations". 2009

## Acknowledgements

I would like to thank all my supervisors for offering me such a great opportunity to work with them in such a wonderful institute. They are Carlton Baugh, Shaun Cole, Carlos Frenk and Adrian Jenkins. I sincerely appreciate their great enthusiasm, patience and help. It is really enjoyable working with them. Through three years of interaction with them, my passion for cosmology and curiosity about fundamental science have been brought up to a level that I could not have reached on my own. The PhD experience I have had in Durham has been the most wonderful and enjoyable experience ever in my life.

I would like to thank to Lydia Heck for all her help and support in computing. I thank Lindsay Borrero and Dorothy Jenkins for their considerate help.

Finally, I would like to thank all my friends inside and outside Durham astronomy. With them, I have explored the amazing culture diversity of our planet, and looked deep into another fascinating world in our universe, the integrity and genuineness of the human mind.

This thesis was supported by the Marie Curie Early Stage Training Host Fellowship ICCIPPP, which is funded by the European Commission.

# Chapter 1 | *Introduction*

## 1.1 Cosmological principles

After a few billions of years of evolution, even with the great advances in science, human beings are not able to travel across large scales of the universe within a human lifetime. We cannot even go outside the solar system, which is just one of the $10^{11}$ stars in the Milky Way galaxy, while the Milky Way galaxy is one of the $10^{11}$ galaxies within the observable horizon of the universe. We can not fly to other galaxies to check what the universe would look like there. In order to understand the universe we are observing, we have to assume that the universe will look the same everywhere and in all directions on large scales. These two assumptions, the homogeneity and isotropy, are fundamental to modern cosmology. Under these assumptions, Einstein's field equations can be reduced to the Friedmann equations:

$$\frac{\ddot{a}}{a} = -\frac{4\pi G}{3}\left(\rho + \frac{3p}{c^2}\right) + \frac{\Lambda c^2}{3} \tag{1.1}$$

$$\left(\frac{\dot{a}}{a}\right)^2 = \frac{8\pi G}{3}\rho - \frac{Kc^2}{a^2} + \frac{\Lambda c^2}{3} \tag{1.2}$$

where $G$ is the gravitational constant, $c$ is the speed of light, $K$ is the curvature of the universe, $\rho$ is the mean density, $p$ is the pressure of the cosmic fluids, $\Lambda$ is the cosmological constant, and $a$ is the dimensionless scale factor normalized to be unity at present. Given the equation of state $p = p(\rho)$ for each ingredient of the universe, we can solve the above equations to obtain densities as a function of cosmic scale, $\rho = \rho(a)$ and predict the cosmic scale factor as a function of time, $a = a(t)$. If we assume the equation of state is of the general form, $p = \omega c^2 \rho$, we find

$$\rho \propto a^{-3(1+w)} \tag{1.3}$$

When the universe is dominated by a single component, $\omega$ has characteristic values, specifically

$$\begin{aligned}
\omega = 0, &\quad \rho \propto a^{-3} \propto (1+z)^3, \quad \text{matter} \\
\omega = \tfrac{1}{3}, &\quad \rho \propto a^{-4} \propto (1+z)^4, \quad \text{radiation} \\
\omega = -1, &\quad \rho \propto a^{0}, \quad \text{cosmological constant, } \Lambda \\
-1 < \omega < 0, &\quad \rho \propto a^{3(1+\omega)} \propto (1+z)^{3(1+\omega)}, \quad \text{quintessence}
\end{aligned}$$

where $a = 1/(1+z)$ and $z$ is the redshift at the time when the scale factor is $a$. Both $a$ and $z$ are commonly used as a time label to describe the evolution of the universe. We know for certain that matter and radiation ingredients exist in our universe. Yet we know very little about the cosmological constant or whether there is any other form of energy/matter with a time-varying equation of state. But there are many studies showing that by including some kind of 'dark energy' with $\omega$ close to $-1$, we are able to explain observational data nicely (see section 1.2 for more details). Therefore, in this thesis, as an example, we will explore the simplest form of dark energy, $\omega = -1$. All our numerical experiments and analysis are carried out with this form. Also, from observation of the mean cosmic microwave background temperature, we can infer that matter dominates over radiation for most of the history of the Universe, where the contribution of radiation can be neglected. We can simply drop the radiation ingredient for our analysis of the universe after the epoch of recombination. It is conventional to quantify the expansion rate of the universe by introducing the Hubble constant, $H = \dot{a}/a$, and the density parameters of cosmic fluids by taking their ratios to the square of the present Hubble constant, $H_0^2$,

$$\Omega_{\rm m} = \frac{\rho_0}{\rho_c}, \ \Omega_\Lambda = \frac{\Lambda c^2}{3H_0^2}, \ \Omega_K = -\frac{Kc^2}{a_0^2 H_0^2}, \tag{1.4}$$

where $\rho_{\rm c} = 3H_0^2/8\pi G$ is the critical density of the universe at the present time. Then the Friedmann equation, (1.2), describing the expansion history of the universe becomes

$$\frac{H^2(z)}{H_0^2} = \Omega_{\rm m}(1+z)^3 + \Omega_\Lambda + \Omega_K(1+z)^2 \tag{1.5}$$

As the curvature of the universe has been shown to be very close to zero from measurements of CMB temperature fluctuations, $\Omega_K \approx 0$, we can also drop the curvature term in the above equation to find

$$\frac{H^2(z)}{H_0^2} = \Omega_{\rm m}(1+z)^3 + \Omega_\Lambda. \tag{1.6}$$

Or equivalently, we can express the above equation as

$$\Omega_{\rm m}(z) + \Omega_\Lambda(z) = 1, \tag{1.7}$$

where $\Omega_{\rm m}(z) = \Omega_{\rm m}(1+z)^3 H_0^2/H^2(z)$ and $\Omega_\Lambda(z) = \Omega_\Lambda H_0^2/H^2(z)$ are the density parameters at redshift $z$. In this cosmology, we can infer from equation (1.1) that in the early universe when the matter density, $\rho$, is dominant over $\Lambda$, $\ddot{a}/a$ is negative, the universe is expanding at a decelerating rate. As $\rho$ is deceasing with time while $\Lambda$ remains constant, there must be a time when $\Lambda$ becomes dominant over $\rho$. Then $\ddot{a}/a$ becomes positive and the expansion of the universe starts to accelerate. The transition from being decelerating to accelerating can be determined by setting $\ddot{a}/a = 0$, which gives

$$\Lambda = 4\pi G\rho = 4\pi G\rho_0(1+z_{\rm t})^3, \tag{1.8}$$

where $z_{\rm t}$ is the redshift corresponding to the time when the transition occurs. Taking the conventional notation, we obtain

$$z_t = \left(\frac{2\Omega_\Lambda}{\Omega_{\rm m}}\right)^{1/3} - 1. \tag{1.9}$$

If we take $\Omega_{\rm m} = 0.26$ and $\Omega_\Lambda = 0.74$, we find the transition occurs at $z_{\rm t} \sim 0.8$. We can also easily obtain the age of the universe from equation (1.6):

$$t = -\frac{1}{H_0}\int_\infty^0 \frac{dz}{(1+z)\sqrt{\Omega_{\rm m}(1+z)^3 + \Omega_\Lambda}}. \tag{1.10}$$

Taking the Hubble constant as $H_0 = 71.5$ kms$^{-1}$Mpc$^{-1}$ at the present, we find $z_{\rm t} = 0.8$ corresponds to about half of the age of the universe, which is 14 Gyr. The expansion of the universe before that epoch and after recombination is dominated by the matter content, while after that, it is dominant by $\Omega_\Lambda$.

In summary, in this concordance cosmology, the dynamical history of the universe is only determined by three quantities, the Hubble constant $H_0$, the matter density parameter $\Omega_{\rm m}$ at the present time and the cosmological constant $\Omega_\Lambda$, which is normally referred to as dark energy.

## 1.2 Observational constraints for dark energy

We have mentioned in the previous section that a cosmological constant term with $\omega = -1$ is favoured by astronomical observations. This 'observational evidence for

dark energy' mainly comes from the combined constraints of CMB temperature fluctuations, the distance redshift relation from Type Ia Supernovae and the clustering of large-scale structure.

The position of the first acoustic peak in the CMB power spectrum as a function of spherical multipole moment, $l$ is sensitive to the geometry of the universe. It has been measured to be at around $l = 200$ by the WMAP satellite (Komatsu et al., 2008). Combining with the $H_0$ constraint from the nearby universe, this indicates that the curvature of the universe should be close to zero, and the total energy density of the universe is close to unity. Therefore, $\Omega_{\rm m} + \Omega_\Lambda \approx 1$, if one express the dark energy as the cosmological constant. The dark matter density can in principle be measured by higher acoustic peaks in the CMB power spectrum, yet such constraints are weaker. This leads to degeneracy between $\Omega_{\rm m}$ and $\Omega_\Lambda$. The degeneracy can be broken by independent observational constraints from the nearby universe.

Using Type Ia supernovae as a measurement of the distance redshift relation is one method. By assuming the intrinsic luminosity of Type Ia supernovae is always the same (in fact with a small scatter), one can measure the luminosity distances of many Type Ia supernovae at different redshifts, while for a given cosmology with fixed values of parameters, the distance redshift relation is known. The direct comparison of the observed distance redshift relation with that given by models enable one to distinguish different models. Constraints on model parameters are also possible given large enough samples. In 1998, it was found, assuming a a flat universe, that cosmologies with a cosmological constant provide better fits to the 42 Type Ia supernovae in the redshift range of $z = 0.18 - 0.83$ (Perlmutter et al., 1998). Such a model was also favoured by the analysis of Type Ia supernovae at $z$=0.16-0.62 (Riess et al., 1998) and by subsequent results using higher redshift samples (i.e. Riess et al., 2004). The best fit value of $\Omega_{\rm m}$ is close to 0.3 for most of these measurements, well below unity. Putting these together with the constraints from the CMB, a value of $\Omega_\Lambda \approx 0.7$ can be inferred.

Another independent constraint comes from the clustering of dark matter in large-scale structure. Using galaxies as a tracer of the underlying dark matter, one can measure the amplitude of the clustering of matter at different scales, using the two point correlation function or power spectrum methods. The shape of the matter power spectrum in the linear regime is the same as that at the epoch of recombination, while its amplitude is scaled by the linear growth factor $D(t)$. Fitting the

observed galaxy power spectrum with a certain cosmological model enables one to constrain the matter density parameter times the Hubble constant. This is able to break the degeneracy in the CMB power spectrum measurement between $\Omega_K$ and $\Omega_\Lambda$ (Efstathiou et al., 2002; Sánchez et al., 2006). Another useful feature in the galaxy power spectrum is the baryonic acoustic oscillations (BAO), which are another powerful probe of dark energy (i.e. Blake and Glazebrook, 2003; Hu and Haiman, 2003). The amount of information in the galaxy power spectrum is enormous. Measuring the galaxy power spectrum is one of the main goals of galaxy survey astronomy.

The 2dF galaxy redshift survey has measured the clustering of galaxies in the local Universe, at $\bar{z} \sim 0.1$. Power spectrum analysis of the 200k galaxies has been able to infer the matter content of the universe to great accuracy, $\Omega_{\rm m}h = 0.168 \pm 0.016$ (Cole et al., 2005). This is in good agreement with the results from the the Sloan Digital Sky Survey (SDSS) (Tegmark et al., 2004a), after taking into account the difference in galaxy colours of the two data sets (Cole et al., 2007; Sánchez and Cole, 2008).

There is a large abundance of information in large-scale structure data. While the galaxy power spectrum is one of the most useful statistics, the number density of dark matter halos as a function of halo mass and time, $dN/dMd$t, the halo mass function, also encodes information on the dynamics of the universe. Its application to constraining cosmology can be found in Jenkins et al. (e.g. 2001); Macciò et al. (e.g. 2004); Warren et al. (e.g. 2006); Reed et al. (e.g. 2007); Tinker et al. (e.g. 2008); Francis et al. (e.g. 2009). It is one of the main goals of many ongoing and future observations of galaxy clusters using radio [via the Sunyaev-Zel'dovich (SZ) effect (Sunyaev and Zeldovich, 1972)], optical and X-rays, as well as using the gravitational lensing technique.

All these observations from nearby large-scale structure tend to favour a low mass density universe, which provides another independent constraint on the value of $\Omega_\Lambda$, when combining with the flatness measurements given by the CMB power spectrum. In other words, $\Omega_\Lambda$ is needed to explain the angular positions of the acoustic peaks in the observed CMB power spectrum and at the same time being consistent with the matter density measured from nearby universe. However, combining all these observations, we still know very little about the nature of dark energy. There is nothing to stop one introducing a cosmological constant in the Einstein's field equations. However, the physics of this term remains unclear. In fact, it gives rise to the 'fine tuning

problem', in which the energy density of the constant is more than 100 orders of magnitudes smaller than the predicted vacuum energy density, and the 'coincidence problem', where the crossover of $\Omega_{\rm m}$ and $\Omega_\Lambda$ only occurs very close to the present (Copeland et al., 2006). It seems a cosmological constant is simple to formulate mathematically but difficult to explain physically. On the other hand, in dynamical dark energy models, one or other of the problems can be addressed. Therefore, distinguishing the cosmological constant from dynamical dark energy models is fundamentally important. However, the goal has not yet been achieved, even combining all the observations that we mentioned. In fact a time-varying equation of state can provide an equally good fit to those observations, as long as it converges to $-1$ at late times. Dark energy, whether it is a constant or dynamical, remains 'dark'.

## 1.3 Missing link between CMB and LSS

The mystery of dark energy is one of the most intriguing topics in modern cosmology. Our current knowledge of the history of universe is limited by the fact that we have just obtained observations from two distant epochs, one from the epoch of recombination at $z = 1100$ when the universe is only about 380,000 years old with the mean temperature of about 3,000 K, the other one from the present local universe, i.e the analysis of large-scale structure and Type Ia supernovae. Intrinsically, the constraint on the cosmology using two snapshots are not sufficient to infer the properties of dark energy, especially its dynamics. We need more observations in the intervening epochs of the Universe to shed light on dark energy. That is to perform cosmological tomography, i.e. to obtain independent cosmological constraints at many different epochs of the universe and hence determine the dynamical history of the universe.

There are in general two approaches towards cosmological tomography, both of which use galaxies as tracers of the underlying matter and rely on large and deep galaxy surveys. Galaxy surveys being large enable us to achieve fair sample statistics, while their depth enables us to probe earlier.

**1) Direct analysis of large and deep galaxy surveys**

Galaxy samples are sliced according to their redshifts. All large-scale structure statistics, power spectrum, redshift space distortion, BAO, halo mass function and so on can be performed within each redshift bin. Constraints on cosmology from

these analyses will be obtained independently.

**2) Looking for CMB secondary effects arising from large-scale structure.**

CMB photons will interact with the matter along their paths through the universe after they are emitted from the last scattering surface. Such interactions generate secondary anisotropies to the primordial CMB anisotropies. Those secondary anisotropies depend on the intervening distribution and the evolution of dark matter and dark energy as well as baryons. Therefore, they carry large amounts of information on the intervening universe. Among these CMB secondary effects, the Integrated Sachs-Wolfe (ISW) effect (Sachs and Wolfe, 1967) is a very powerful tool for constraining the dynamics of dark energy. It is the main topic of this thesis.

The ISW effect arises from the decay of the large-scale potential fluctuations as they are traversed by Cosmic Microwave Background (CMB) photons and induces secondary temperature perturbations in the CMB radiation. It occurs in both open models ($\Omega_{\rm m} < 1$) and models containing a cosmological constant ($\Omega_\Lambda > 0$) or dark energy. It has been shown to be an independent way of measuring the dynamical effect of such dark energy. Large and deep galaxy surveys can be used to do ISW tomography. The basic idea is to use galaxy samples in redshift slices to cross-correlate with the CMB and obtain independent constraints on dark energy at different epochs. Details of this techniques will be shown in Chapter 3.

## 1.4 Challenges and opportunities

Observationally, to achieve all these goals, requires challenging galaxy surveys of adequate depth and width. This requires a new generation of galaxy surveys at least one order of magnitude larger than the 2dFGRS and the SDSS. Unfortunately, measuring redshifts for tens of millions of galaxies is not feasible with current instrumentation. Attention has therefore shifted to the possibility of carrying out extremely large surveys of galaxies in which, instead of using spectroscopy, redshifts are estimated from deep multi-band photometry. Although the accuracy of these estimates is limited, this strategy can yield measurements for hundreds of millions of galaxies or more. Large and deep photometric redshift galaxy surveys such as Pan-STARRS1 (PS1)[1],

[1]The Panoramic Survey Telescope and Rapid Response System, http://www.ps1sc.org

LSST[2], are ongoing or being planned. (There are also spectroscopic redshift surveys like BOSS[3] which is ongoing and JDEM[4] being planned.) The performance of photometric redshift measurements will largely limit the accuracy of cosmological constraints given by these surveys. Understanding the effect of photo-$z$ errors on large-scale structure measurements is both important and challenging. In Chapter 2, we show an example of using experimental data to forecast the performance of Pan-STARRS1 on constraining the equation of state parameter, $\omega$.

In theory, the ISW effect is challenging to detect and the contaminations of other CMB secondary effect remains unclear. At large scales, the ISW signal suffers from cosmic variance, as there are too few independent modes, while at somewhat smaller scales, it is entangled with the Rees-Sciama (RS) effect (Rees and Sciama, 1968), which arises from the non-linear evolution of gravitational potential perturbations. Since it is impossible to evade the cosmic variance at large scales, the information at small scales becomes valuable. Hence, to extract cosmological information from such scales, one needs to disentangle the ISW and RS effects. Moreover, other CMB secondary effects may also contaminate the ISW signal at small scales.

First, the thermal SZ effect (Sunyaev and Zeldovich, 1972) that arises from the inverse Compton scattering off hot electrons in galaxy clusters shifting low energy CMB photons towards the high energy end of the spectrum. The SZ effect is the dominant CMB secondary effect at arcmin angular scales. With its strong spectral features, it can be distinguished from other CMB secondary signals. The kinetic SZ (kSZ) effect arising from the CMB photons being scattered by the bulk motion of gas in clusters, however, has the same spectral signature as the ISW effect. It may confuse the ISW signal at a certain level. A detailed discussion of the kSZ effect is given in Chapter 4. Secondly, gravitational lensing is another important CMB secondary effect, which arises from CMB rays being bent by foreground gravitational potentials. Its correlation with the ISW and RS has been addressed in the literature using analytical methods (Verde and Spergel, 2002; Giovi et al., 2003; Boubekeur et al., 2009; Mangilli and Verde, 2009). More precise study in the deep non-linear regime is needed.

Understanding the contaminations of these CMB secondary effects on the mea-

[2]The Large Synoptic Survey Telescope, http://www.lsst.org

[3]The SDSS-III's Baryon Oscillation Spectroscopic Survey, http://www.sdss3.org/cosmology.php

[4]The Joint Dark Energy Mission, http://jdem.gsfc.nasa.gov

surements of the ISW signal is essential to enable thorough exploitation of the opportunities rendered by future large and deep galaxy surveys. This is one of the main goals of this thesis.

## 1.5 Outline of the thesis

Prior to obtaining large data sets, a complete understanding of galaxy surveys as well as data analysis methods is essential. At the time when the first large photometric redshift survey, Pan-STARRS1, is commencing, this thesis aims at developing the first understanding of dark energy constraints from photometric redshift surveys.

In Chapter 2, we will explore a crucial factor for the accuracy of the large-scale structure measurement in this kind of survey, the photometric redshift performance. To achieve our goals, we construct mock galaxy catalogues from a semi-analytic model of galaxy formation implemented in N-body simulations. We will also use mock catalogues to forecast other aspects of the survey.

We mainly focus on the ISW effect, which is a direct probe of dark energy. In Chapter 3, we study the non-linear contaminations of the cross-correlation of CMB and galaxy samples. In Chapter 4, we will explore more thoroughly the linear and non-linear ISW effect using sky maps. We will address the physics of the linear and non-linear ISW effects. We try to disentangle the ISW effect from other CMB secondary anisotropies and quantify its contribution to CMB anomalies.

# Chapter 2

# *Mock galaxy redshift catalogues from simulations and their implications*

## 2.1 Introduction

Studies of the cosmic large structure were brought to a new level by the two large galaxy surveys of the past decade, the "2-degree-field galaxy redshift survey (2dFGRS; Colless et al., 2001) and the Sloan Digital Sky Survey (SDSS York et al., 2000). The former relied on photographic plates for its source catalogue while the latter was compiled from the largest CCD based photometric survey to date. Most of the large-scale structure studies carried out with these surveys made use of spectroscopic redshifts, for about 220,000 galaxies in the case of the 2dFGRS and 585,719 galaxies in the case of the SDSS (Strauss et al., 2002). These surveys achieved important advances such as the confirmation of the existence of dark energy (Efstathiou et al., 2002; Tegmark et al., 2004b) and the discovery of baryonic acoustic oscillations (Percival et al., 2001; Cole et al., 2005; Eisenstein et al., 2005). Yet, a number of fundamental questions on the cosmic large-scale structure remain unanswered, such as the identity of the dark matter and the nature of the dark energy.

Further progress in the subject is likely to require a new generation of galaxy surveys at least one order of magnitude larger than the 2dFGRS and the SDSS. Unfortunately, measuring redshifts for millions of galaxies is not feasible with current instrumentation. Attention has therefore shifted to the possibility of carrying out extremely large surveys of galaxies in which, instead of using spectroscopy, redshifts are estimated from deep multi-band photometry. Although the accuracy of these

estimates is limited, this strategy can yield measurements for hundreds of millions of galaxies or more. Several instruments are currently being planned to carry out such a programme. The most advanced is the Panoramic Survey Telescope & Rapid Response System (Chambers, 2006). Of an eventual 4 telescopes for this system, the first one, PS1, is now in its final commissioning stages and is expected to begin surveying the sky early in 2009. This telescope is likely to be quickly followed by the full Pan-STARRS system and by the Large Synoptic Survey Telescope (LSST Tyson, 2002). Several other smaller photometric surveys are currently underway (UKIDSS, Megacam etc. Lawrence et al., 2007; Boulade et al., 2003).

One of the important lessons learned from previous surveys, including 2dFGRS and SDSS, is the paramount importance of careful modelling of the survey data for the extraction of robust astrophysical results. Such modelling is best achieved using large cosmological simulations to follow the growth of structure in a specified cosmological background. The simulations can be used to create mock versions of the real survey in which the geometry and selection effects are reproduced. Such mock surveys allow a rigorous assessment of statistical and systematic errors, aid in the design of new statistical analyses and enable the survey results to be directly related to cosmological theory. Mock catalogues based on cosmological simulations were first used in the 1980s, in connection with the CfA galaxy survey (Davis et al., 1985; White et al., 1988) and redshift surveys of IRAS galaxies (Saunders et al., 1991) and have been extensively deployed for analyses of the 2dFGRS and the SDSS (Cole et al., 1998; Blaizot et al., 2006).

The recent determination of the values of the cosmological parameters by a combination of microwave background and large-scale structure data (e.g. Sánchez et al., 2006; Komatsu et al., 2008) has removed one major layer of uncertainty in the execution of cosmological simulations. N-body techniques are now sufficiently sophisticated that the evolution of the dark matter can be followed with impressive precision from the epoch of recombination to the present (Springel et al., 2005). The main uncertainty lies in calculating the evolution of the baryonic component of the Universe.

The size of the planned photometric surveys and the need to understand and quantify uncertainties in estimates of photometric redshifts and their consequences for diagnostics of large-scale structure pose novel challenges for the construction of mock surveys. The simulations need to be large enough to emulate the huge volumes that will be surveyed and, at the same time, the modelling of the galaxy population

needs to be sufficiently realistic to allow an assessment of the uncertainties introduced by photometric redshifts. At present, the only technique that can satisfy both these two requirements is the combination of large N-body simulations with semi-analytic modelling of galaxy formation.

Semi-analytic models of galaxy formation are able to follow the evolution of the baryonic component in a cosmological volume by making a number of simplifying assumptions, most notably that gas cooling into halos can be calculated in a spherically symmetric approximation (White and Frenk, 1991). Once the gas has cooled, these models employ simple physically based rules, akin to those used in hydrodynamic simulations, to model star formation and evolution and a variety of feedback processes. The analytical nature of these models makes it possible to investigate galaxy formation in large volumes and to include, in a controlled fashion, a variety of processes, such as dust absorption and emission, that are currently beyond the reach of hydrodynamic simulations. (For a review of this approach, see Baugh, 2006). It is reassuring that the simplified treatment of gas cooling in these models agrees remarkably well with the results of full hydrodynamic simulations (Helly et al., 2003; Yoshida et al., 2002).

An important feature of semi-analytic models is that they are able to reproduce the local galaxy luminosity function from first principles (e.g. Cole et al., 2000; Benson et al., 2003; Hatton et al., 2003; Baugh et al., 2005; Kang et al., 2005, 2006; Bower et al., 2006; Croton et al., 2006; De Lucia et al., 2006) and, in the most recent models, also its evolution to high redshift (Bower et al., 2006; De Lucia et al., 2006; Lacey et al., 2008). These recent models also provide a good match to the distribution of galaxy colours, which is particularly relevant for problems relating to photometric redshifts. And, of course, the models also calculate many properties which are not directly observable (e.g. rest-frame fluxes, stellar masses, etc) but which are important for the interpretation of the data.

There are currently two main approaches to the estimation of photometric redshifts. One employs an empirical relation, obtained by fitting a polynomial or a more general function derived by an artificial neural network, between redshift and observed properties, such as fluxes in specified passbands (e.g. Connolly et al., 1995; Brunner et al., 2000; Sowards-Emmerd et al., 2000; Firth et al., 2003; Collister and Lahav, 2004). The second method is based on fitting the observed spectral energy distribution (SED) with a set of galaxy templates (e.g. Sawicki et al., 1997; Gial-

longo et al., 1998; Bolzonella et al., 2000; Benítez, 2000; Bender et al., 2001; Csabai et al., 2003), obtained either from observations of the local universe (e.g. Coleman et al., 1980) or from synthetic spectra (e.g. Bruzual and Charlot, 1993, 2003). Some authors (e.g. Collister and Lahav, 2004) claim that the empirical fitting method can give smaller redshift errors, but this method relies on having a well-matched spectroscopic subsample that reaches the same depth in every band as the photometric survey. Unfortunately, for Pan-STARRS or LSST this is going to be challenging and to be conservative in this initial investigation we use Hyper-$z$ because it does not require a training set.

In this chapter, we describe a method for generating mock catalogues suitable, in principle, for the next generation of large photometric surveys. As an example, we construct mocks surveys tailored to PS1. PS1 will carry out two, 3-year long surveys in 5 bands $(g, r, i, z, y)$, the "$3\pi$ survey" which will cover three quarters of the sky to a depth of about $r = 24.5$ and the "medium deep survey" (MDS) which will cover 84 sq deg to a $5-\sigma$ point sources depth of $r = 27$ (AB system). The former will enable a comprehensive list of large-scale structure measurements, including the integrated Sachs-Wolfe effect and baryonic acoustic oscillations. The latter will be used to study clustering on small and intermediate scales, as well as galaxy evolution. To construct the mocks we use the semi-analytic model of Bower et al. (2006, hereafter B06) as implemented in the Millennium simulation (Springel et al., 2005). A sophisticated adaptive template method based on the work of Bender et al. (2001) will be employed for the genuine PS1 survey. The method has been applied in the photo-$z$ measurements of FORS Deep Field galaxies (Gabasch et al., 2004) and achieved $\Delta z/(1+z_{\rm spec}) \leq 0.03$ with only 1% outliers. However, the method requires precise calibration of zeropoints in all filters using the colour-colour plots of stars, and a control sample of spectroscopic redshifts. Consequently this method cannot be rigorously tested until genuine PS1 data is available. Therefore, for a first look at the photo-$z$ performance of PS1, we adopt the standard SED fitting method as implemented in the Hyper-$z$ for our mock catalogues.

The chapter is organised as follows. In §2.2, we briefly summarise the models and detail the process of constructing mock galaxy catalogues. In §2.3 we analyse some of their properties and in §2.4 we use the mock catalogues to assess the accuracy with which photometric redshifts will be estimated by PS1. In §2.5, we discuss how these uncertainties are likely to affect the accuracy with which baryonic acoustic

oscillations, one of the main targets for PS1, can be measured in the survey. Finally, in §2.6, we discuss our results and present our conclusions.

## 2.2 Mock catalogue construction

In this section we describe how we construct mock catalogues. In §2.2.1 we describe the semi-analytic galaxy formation code that we use. In §2.2.2 we compare the luminosities and sizes of the model galaxies to SDSS data and modify them to improve the accuracy of the mocks. Finally in §2.2.3 we describe how the mock catalogues themselves are built.

### 2.2.1 The galaxy formation model

The first step in the process of generating a mock catalogue is to produce a population of model galaxies over the required redshift range. We use the GALFORM semi-analytic model of galaxy formation (Cole et al., 2000; Benson et al., 2003; Baugh et al., 2005; Bower et al., 2006) to do this. GALFORM calculates the key processes involved in galaxy formation: (i) the growth of dark matter halos by accretion and mergers; (ii) radiative cooling of gas within halos; (iii) star formation and associated feedback processes due to supernova explosions and stellar winds; (iv) the suppression of gas cooling in halos with quasistatic hot atmospheres and accretion driven feedback from supermassive black holes (see Malbon et al. (2007) for a description of the model of black hole growth); (v) galaxy mergers and the associated bursts of star formation; (vi) the chemical evolution of the hot and cold gas, and the stars.

GALFORM uses physically motivated recipes to model these processes. Due to the complex nature of many of them, the model necessarily contains parameters which are set by requiring that it should reproduce a subset of properties of the observed galaxy population (see Cole et al., 2000; Baugh, 2006, for a discussion of the philosophy behind setting the values of the model parameters).

GALFORM predicts star formation histories for the population of galaxies at any specified redshift. These histories are far more complicated than the simple, exponentially decaying star formation laws sometimes assumed in the literature (for examples of star formation histories of GALFORM galaxies, see Baugh, 2006). The GALFORM histories have the advantage that they are produced using an astrophysical model in which the supply of gas available for star formation is set by source and

sink processes. The sources are the infall of new material due to gas cooling and galaxy mergers and gas recycling from previous generations of stars. The sinks are star formation and the reheating or removal of cooled gas by feedback processes. The metallicity of the gas consumed in star formation is modelled using the instantaneous recycling approximation and by following the transfer of metals between the hot and cold gas, and the stellar reservoirs (see Fig. 3 of Cole et al., 2000).

The model outputs the broad band magnitudes of each galaxy for a set of specified filters. In this chapter we use the PS1 filter set ($g$, $r$, $i$, $z$, $y$) (Chambers, 2006), augmented by a few additional filters where some of the PS1 galaxies may be observed as part of other observational programmes ($U$, $B$, $J$, $H$, $K$). In addition to the magnitudes of model galaxies in the observer's frame, we also output the rest frame $g-r$ colour, in order to distinguish between red and blue galaxy populations. GALFORM tracks the bulge and disk components of the galaxies separately (Baugh et al., 1996). The scale sizes of the disk and bulge (assumed to follow an exponential profile and an $r^{1/4}$-law in projection, respectively) are also calculated (Cole et al., 2000) (see Almeida et al., 2007, for a test of the prescription for computing the size of the spheroid component).

The B06 model which we use in this chapter employs halo merger trees extracted from the Millennium N-body simulation of a $\Lambda$-cold dark matter universe (Springel et al., 2005). The model gives a very good reproduction of the shape of the present day galaxy luminosity function in the optical and near-infrared. Also of particular relevance for the predictions presented here is the fact that this model matches the observed evolution of the galaxy luminosity function.

### 2.2.2 Improving the match to SDSS observations

To make the mocks as realistic as possible, we modify the luminosities and sizes of the model galaxies to give a better fit to SDSS data. Although both the $b_J$-band and K-band luminosity functions of the B06 model have been shown to agree well with observations of the local universe, the agreement is not perfect and a shift of 0.15 magnitude faintwards in all bands improves the match to the data as can be seen in Fig. 2.1. The original B06 K-band luminosity functions also match observations up to redshift $z = 1.5$ (Bower et al., 2006), although the observational error bars are relatively large. Hence, even after applying the 0.15 magnitude shift the agreement between model and high redshift observations remains reasonably good.

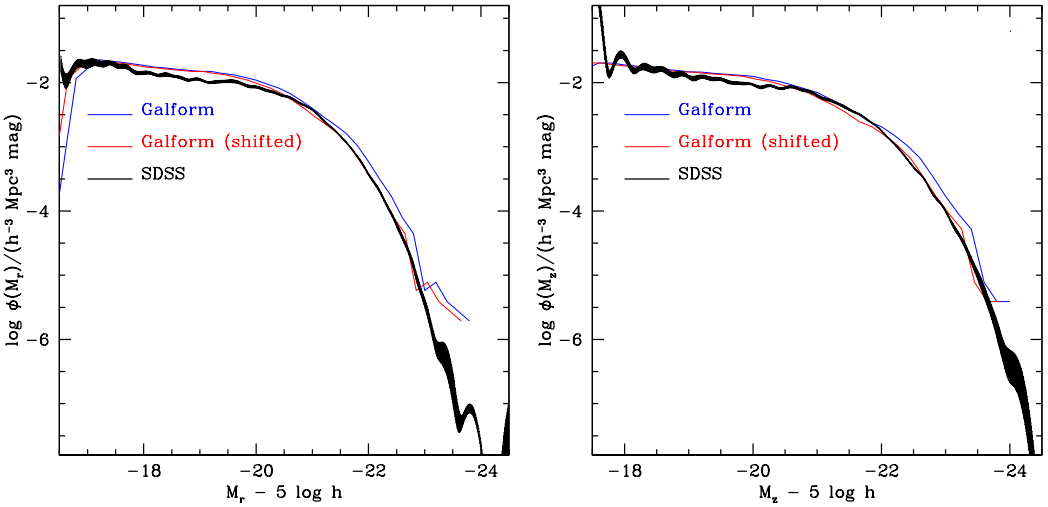


Figure 2.1: Luminosity functions predicted by GALFORM, compared with the SDSS results in the $r$-band (left) and $z$-band (right), table from Blanton et al. (2003). The black lines with error bars indicated by the shaded region are the SDSS results. The blue lines show the original GALFORM prediction, while the red lines show the GALFORM prediction globally shifted faintwards by 0.15 magnitudes.

The GALFORM magnitudes we have been dealing with so far are total integrated magnitudes. In reality all but the most distant galaxies in the survey will be resolved over several pixels and will have lower signal to noise in each of these pixels than a point source would. To take this into account it proves convenient to use Petrosian (1976) magnitudes. These have the advantage over fixed aperture magnitudes that, for a given luminosity profile shape, they measure a fixed fraction of the total luminosity independently of the angular size and surface brightness of the galaxy. The Petrosian flux within $N_p$ times the Petrosian radius, $r_P$, is:

$$F_P = 2\pi \int_0^{N_P r_P} I(r) r \mathrm{d}r, \tag{2.1}$$

where $I(r)$ is the surface brightness profile of the galaxy. The Petrosian radius is defined such that at this radius, the ratio of the local surface brightness in an annulus at $r_P$ to the mean surface brightness within $r_P$, is equal to some constant value $\eta$, specifically:

$$\eta = \frac{2\pi \int_{0.8 r_P}^{1.25 r_P} I(r)\mathrm{d}r / [\pi((1.25\mathrm{r_P})^2 - (0.8\mathrm{r_P})^2)]}{2\pi \int_0^{r_P} I(r) r \mathrm{d}r / (\pi \mathrm{r_P^2})}. \tag{2.2}$$

We choose the parameter values as $N_P = 2$ and $\eta = 0.2$ as adopted in the SDSS (e.g. Yasuda et al., 2001).

We decompose the surface brightness profile of each galaxy, $I(r)$, into the superposition of a disk and a bulge: $I(r) = I_{\rm disk}(r) + I_{\rm bulge}(r)$. The disk component is taken to have a pure exponential profile:

$$I_{\rm disk}(r) = I_0 e^{-1.68 r/r_d}, \tag{2.3}$$

and the bulge a pure de Vaucouleurs profile :

$$I_{\rm bulge}(r) = I_0 e^{-7.67[(r/r_b)^{1/4}]}. \tag{2.4}$$

Given these assumptions, and assuming the disks are face-on, we can compute the Petrosian radius by solving Eqn. (2.2) for each GALFORM galaxy.

While GALFORM does provide an estimate of the disk and bulge sizes, it has been shown by Almeida et al. (2007) that the early type galaxy sizes of the B06 model are not in particularly good agreement with the SDSS observational results. Therefore, for the purposes of producing more realistic mocks, we modify the galaxy sizes so as to match the SDSS results given by Shen et al. (2003).

To do this we need to separate the galaxies into early and late types and apply separate corrections to each population. First, we use the concentration parameter defined as $C = R_{90}/R_{50}$ to separate our galaxies into early and late types, where $R_{90}$ and $R_{50}$ are the Petrosian 90% and 50% light radii respectively. We then calculate the ratio of the GALFORM galaxy size to the mean found by Shen et al. (2003) for SDSS galaxies as a function of galaxy magnitude and obtain the average correction factor as a function of magnitude required for the GALFORM galaxies to match the SDSS size data. For early type galaxies at redshift $z = 0.1$ Shen et al. (2003) parameterised the relation between Petrosian half-light radii in the $r$-band, $R_{50}$, and absolute $r$-band magnitude, $M$, as

$$\log(R_{50}) = -0.4aM + b, \tag{2.5}$$

with $a = 0.60$ and $b = -4.63$. While for late type galaxies they found

$$\log(R_{50}) = -0.4\alpha M + (\beta - \alpha)\log[1 + 10^{-0.4(M-M_0)}] + \gamma, \tag{2.6}$$

with $\alpha = 0.21$, $\beta = 0.53$, $\gamma = -1.31$ and $M_0 = -20.52$. To correct the GALFORM galaxy sizes at other redshifts we adopt $R_{50} \propto 1 - 0.27z$ for late type galaxies and $R_{50} \propto -0.33z + 1.03$ for early type galaxies. The former is the relation given by

Bouwens and Silk (2002) which agrees with a combination of SDSS, GEMS and FIRES survey data (Trujillo et al., 2006). The relation for early type galaxies is obtained by taking a linear fit to the data given by Trujillo et al. (2006). Finally, we apply a linear relation between $R_{50}$ and the Petrosian radius, $R_{50} = 0.47 r_P$.

### 2.2.3 Building the mock catalogues

Our goal here is to generate mock catalogues which have the distribution of galaxy redshifts and magnitudes expected for the various PS1 catalogues. For the purposes of this chapter, we do not need to retain the clustering information contained in the Millennium Simulation. We are effectively generating a Monte-Carlo realisation of the redshift distribution expected for a given set of magnitude limits.

There are 37 discrete output epochs in the Millennium simulation between $z = 0$ and $z = 3$. The spacing of the output times is comparable to the typical error on the estimated value of photometric redshifts, as we will see later. To avoid the introduction of systematic errors caused by the discrete spacing of simulation output times, previous work to build mock catalogues used an interpolation of galaxy properties between output times (Blaizot et al., 2005). We follow an alternative approach in this chapter. We have generated nine additional outputs which are evenly spaced between each pair of Millennium simulation outputs. To produce GALFORM output at each of these intermediate steps, the Millennium simulation merger trees ending at the nearest simulation output are used but their redshifts are re-labelled to match the required redshift. Then GALFORM computes the star formation history up to the new output redshift, following the baryonic physics up to that point. This results in a much finer spacing of effective output redshifts which fully takes account of k-corrections, star formation and stellar evolution, but ignores the evolution in the dark matter distribution between the chosen output redshift and the nearest simulation redshift.

To generate a mock catalogue with a smooth redshift distribution we proceed as follows. At each of our closely spaced grid of redshifts, $z_i$, we have a GALFORM output dataset consisting of a set of GALFORM galaxies sampling a fixed comoving volume $V_{\rm GF}$ down to a sufficiently deep absolute magnitude. To each of these datasets we apply a magnitude limit and record the number of galaxies, $N_i$, that remain. The comoving number density of galaxies expected brighter than the limit is then $n(z_i) = N_i/V_{\rm GF}$ and the number we expect per unit redshift in the survey is $n(z)\Omega dV/dz/d\Omega$,

where $\Omega$ is the solid angle of the survey and $dV/dz/d\Omega$ is the comoving volume per unit redshift and solid angle for the adopted cosmology. This can be used to compute $N(z_i) = \int_{z-\Delta z/2}^{z+\Delta z/2}(dN(z)/dz)dz$, the number of galaxies expected in the survey in a redshift bin $\Delta z$, centred at a given redshift, $z_i$. To create a continuous redshift distribution we sample at random this number of galaxies from the corresponding GALFORM output and assign them a random redshift in the interval $\Delta z$ such that we uniformly sample the volume redshift relation. As we have perturbed the redshift of each galaxy, we correspondingly perturb its apparent magnitude according to the difference in distance modulus between the output and assigned redshift. We will see that the residual redshift quantisation in the evolutionary and k-corrections is small compared with the precision achievable for the photometric redshifts. Therefore these residual discreteness effects are not important in the photometric redshift error estimation.

For the purpose of producing predictions for the redshift distribution and number counts of galaxies in PS1 surveys, and to provide an input catalogue with which to test photometric redshift estimators, we generate a mock catalogue which corresponds to a solid angle of 10 square degrees. We generate predictions for the $3\pi$ survey and the MDS by scaling the results from this mock to take into account the difference in solid angle.

Finally we need to apply the magnitude limit. To do this, we use a Gaussian random number generator to sample the noise level $N_r$ of each galaxy for the specific survey under consideration. The galaxy source flux $S$ is also perturbed by its noise, $S_r = S+N_r$. We apply a $5\sigma$ cut for selection by rejecting galaxies with signal-to-noise ratio lower than 5.

## 2.3 PS1 mock catalogues

In this section, we apply the methodology described in §2.2 to the specific case of the PS1 survey. We begin by calculating the magnitude limits which we expect to be reached in the $3\pi$ and MDS surveys for both point and extended sources after one and three years of observations respectively.

### 2.3.1 The magnitude limits for the PS1 $3\pi$ and MDS surveys

The signal with the FWHM diameter registered on a CCD chip from a point source with total apparent magnitude $m$, after an exposure time of $t$ seconds is:

$$S = 0.5\ t \times 10^{-0.4(m-m_1)}, \tag{2.7}$$

where $m_1$ is the magnitude that produces 1 electron per second. The factor of 0.5 comes from assuming the PSF is a 2D Gaussian profile and integrating over the FWHM of this profile.

The signal-to-noise ratio for a point source is given by:

$$S/N = S/\sqrt{\sigma_{\rm P}^2 + \sigma_{\rm S}^2 + \sigma_{\rm RN}^2 + \sigma_{\rm D}^2}, \tag{2.8}$$

where $\sigma_{\rm P}^2 = 0.5t \times 10^{-0.4(m-m_1)}$ is the Poisson counting noise for a source of magnitude $m$ observed for $t$ seconds; $\sigma_{\rm S}^2 = \frac{\pi}{4}\omega^2 \times 10^{-0.4(\mu-m_1)}t$ is the variance from the sky background, where $\mu$ is the average sky brightness in magnitudes per square arcsec and $\omega$, assumed to be 0.78 arcsecs, is the FWHM of the PSF; $\sigma_{\rm RN}^2 = \frac{\pi}{4}\omega^2 \times A^2 \times N_{\rm read}^2$ is the read-out noise of the detector, where, for PS1, A=3.846 pixels/arcsec and $N_{\rm read} = 5$ is the read-out noise in electrons; $\sigma_{\rm D}^2$ is the variance due to dark current and will be assumed to be zero (Chambers, 2006). Table 2.1 lists the expected values of the parameters $\mu$ and $m_1$ and also gives the $5\sigma$ point source magnitude limits resulting from applying this formula to the $3\pi$ survey and the MDS after one and three years.

The signal-to-noise for resolved extended sources will be smaller of fixed magnitude. To estimate this we take the Petrosian radius and the redshift of a galaxy and obtain the solid angle subtended by $2r_P$ of the galaxy, $\theta_g$. Then for extended sources, we define the signal and the noise to be the values integrated over the source aperture $\theta_g$ rather than the FWHM of the PSF. Thus the signal is simply $S = t \times 10^{-0.4(m-m_1)}$, the Poisson noise $\sigma_{\rm P}^2 = t \times 10^{-0.4(m-m_1)}$, the sky background variance is $\sigma_{\rm S}^2 = \frac{\pi}{4}\theta_{\rm g}^2 \times 10^{-0.4(\mu-m_1)}t$ and the read-out noise is $\sigma_{\rm RN}^2 = \frac{\pi}{4}\theta_{\rm g}^2 \times A^2 \times N_{\rm read}^2$. Since we have not convolved the image with the PSF, this treatment would produce a sharp transition in the noise level at the PSF limit. This can be avoided by approximating the convolution of the image profile with the PSF.

Table 2.1: Estimated PS1 $3\pi$ and Medium Deep Survey (MDS) sensitivities. The $3\pi$ survey will cover three quarters of the sky, while the MDS will cover 84 sq deg of the sky in 10 separate regions. $m_1$ and $\mu$ are defined in section 3.1.

| Filter | Bandpass (nm) | $m_1$ AB mag | $\mu$ AB mag/arcsec $^2$ | exposure time in 1st yr ($3\pi$) sec | $5\sigma$ pt. source in 1st yr ($3\pi$) | $5\sigma$ pt. source in 3rd yr ($3\pi$) | $5\sigma$ pt. source in 1st yr (MDS) | $5\sigma$ pt. source in 3rd yr (MDS) |
|---|---|---|---|---|---|---|---|---|
| $g$ | 405-550 | 24.90 | 21.90 | 60× 4 | 24.04 | 24.66 | 26.72 | 27.32 |
| $r$ | 552-689 | 25.15 | 20.86 | 38× 4 | 23.50 | 24.11 | 26.36 | 26.96 |
| $i$ | 691-815 | 25.00 | 20.15 | 60× 4 | 23.39 | 24.00 | 26.32 | 26.91 |
| $z$ | 815-915 | 24.63 | 19.26 | 30× 4 | 22.37 | 22.98 | 25.69 | 26.28 |
| $y$ | 967-1024 | 23.03 | 17.98 | 30× 4 | 20.91 | 21.52 | 24.25 | 24.85 |

Table 2.2: Estimated UKIDSS sensitivities. All the magnitudes are in the AB system. The Large Area Survey (LAS) aims to map about 4000 sq deg of the Northern sky within a few hundred nights. The Deep Extragalactic Survey (DXS) aims to map 35 sq deg of the sky in three separate regions.

| Filter | $\lambda_{\rm eff}$ | $m_1$ | $\mu$ | exposure time | $5\sigma$ | exposure time | $5\sigma$ |
|---|---|---|---|---|---|---|---|
| | (nm) | AB | AB | (LAS) | pt. source | (DXS) | pt. source |
| | | mag | mag/$asec^2$ | sec | (LAS) | h | (DXS) |
| J | 1229.7 | 23.80 | 16.80 | 40× 4 | 20.5 | 2.1 | 23.4 |
| H | 1653.3 | 24.58 | 15.48 | 40× 4 | 20.2 | – | – |
| K | 2196.8 | 24.36 | 15.36 | 40× 4 | 20.1 | 1.5 | 22.86 |

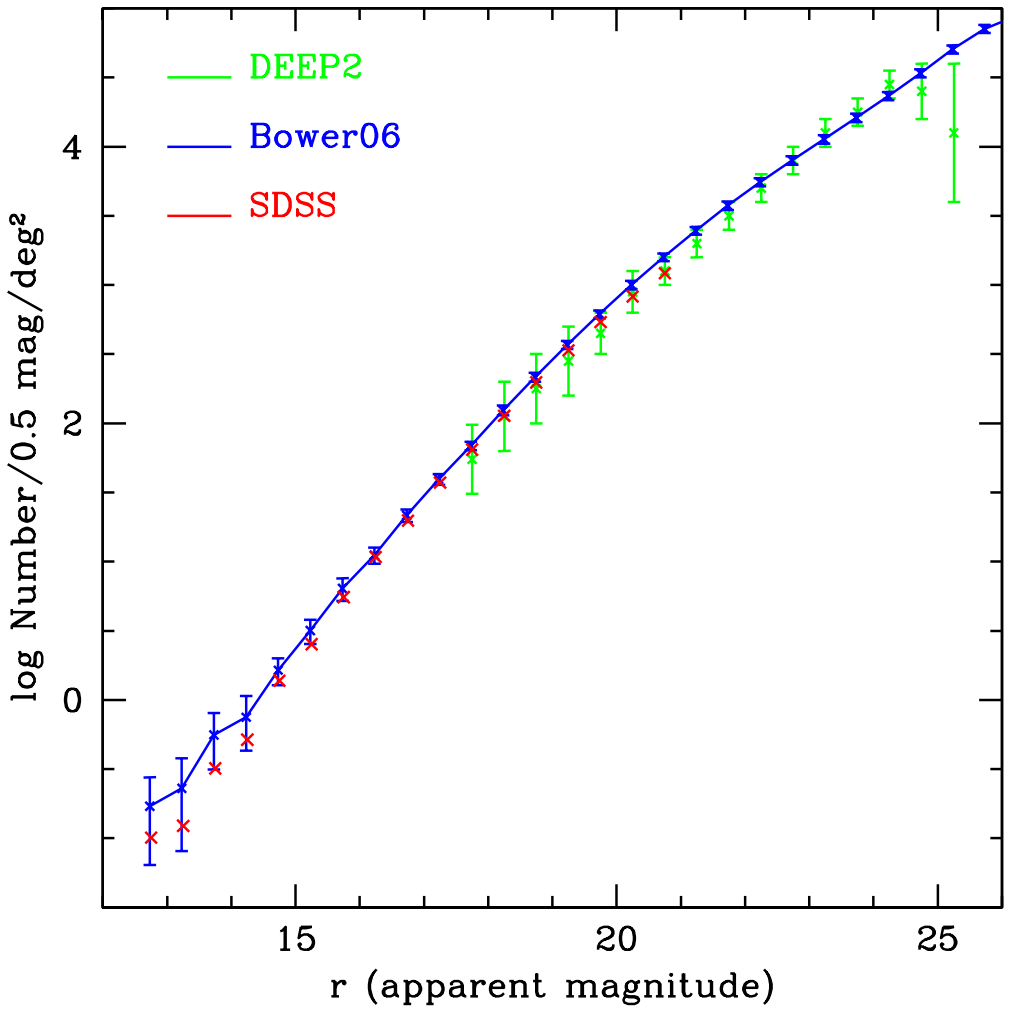


Figure 2.2: Galaxy number counts in 0.5 magnitude centred bins predicted by the GALFORM model in the $r$-band (blue solid line with error bars), compared with the SDSS commissioning data (Yasuda et al., 2001) (red crosses) and the DEEP2 survey data (Coil et al., 2004) (green dots with error bars). The agreement between the model and the data is excellent.

### 2.3.2 A test of the PS1 mock catalogues

Before discussing predictions from our mock catalogues for the $3\pi$ and MDS PS1 surveys, we first carry out a simple test of the realism of our mock catalogues. The GALFORM semi-analytic model has been shown to be consistent with various basic properties of the local galaxy population such as the luminosity functions in the $b_J$ and $K$ bands (Cole et al., 2001; Norberg et al., 2002; Huang et al., 2003). The B06 version of the model also gives an excellent match to the evolution of the rest-frame $K$-band luminosity function, including the data from the K20 (Pozzetti et al., 2003) and MUNIC surveys (Drory et al., 2003) up to redshift $z = 1.5$ (Bower et al., 2006).

Since neither the $b_J$ nor the $K$-band coincide with any of the PS1 *grizy* bands, for a more direct test we compare predicted galaxy number counts in the $r$-band with data. At the faint end we use the number counts over 5 sq deg from the DEEP2 survey (Coil et al., 2004), which are complete to 24.75 in the $R$ band. To minimise sample variance at the bright end, we use galaxy number counts in the SDSS commissioning data (Yasuda et al., 2001) which cover about 440 sq deg and are complete to $r^* = 21$. (We have checked that the difference between the commissioning data and more recent SDSS releases (Fukugita et al., 2004; Yasuda et al., 2007) is negligible). We compute the GALFORM model predictions, including uncertainties, from 10 realizations of 10 sq deg mock surveys. The results, displayed in Fig. 2.2, show that our model prediction agrees very well with both the DEEP2 and the SDSS datasets. Note that we have applied the 0.15 magnitude shift discussed in §2.2 to the model galaxies.

### 2.3.3 Expected PS1 galaxy numbers counts and redshift distributions

We now discuss the expected population statistics for the PS1 surveys predicted by our mock catalogues. We apply Petrosian magnitude cuts in each of the PS1 bands and plot the expected galaxy number counts in 0.5 magnitude bins in Fig. 2.3, for both the 3-year $3\pi$ survey and the MDS. The figure shows that, with the Petrosian magnitude cuts, the samples are no longer complete to the $5\sigma$ point source magnitude limits in the various bands, but rather only to $\sim$2 magnitudes brighter. Note that the $y$-band magnitude limit is substantially shallower than the others and so, if one requires detection in all five bands, the $y$ limit is the most restrictive.

The cumulative distributions on the right hand panels of Fig. 2.3 reveal the staggering number of galaxies that will be detected by PS1. For example, in the $g$-band after 3 years, we expect about $10^9$ galaxies in the $3\pi$ survey and nearly $10^8$ in the MDS.

The expected redshift distributions for the two surveys are shown in Fig. 2.4 for galaxies detected in all 5 bands and in Fig. 2.5 for galaxies detected only in $g, r, i$ and $z$, i.e. not requiring the shallow $y$-band detection. In the first case, the $n(z)$ distribution peaks at $z \sim 0.5$ for the $3\pi$ survey, with about $8 \times 10^7$ and $1.8 \times 10^8$ galaxies detected (in all 5 bands) in the 1- and 3-year surveys respectively. The survey is so huge, that, after 3 years, we expect about 10 million galaxies at $z > 0.9$ and 5 million at $z > 1$. For the MDS survey, the $n(z)$ distribution peaks at $z \sim 0.8$, with a total of $1.7 \times 10^7$ galaxies after 3 years of which around 0.5 million lie at $z > 2$. Removing the $y$-band constraint leads to a large increase in the number of galaxies, as shown in Fig. 2.5. In this case, the $3\pi$ survey will contain $\sim 5 \times 10^8$ galaxies after three years, with about 30 million at $1 < z < 1.3$, while the MDS will contain $\sim 3 \times 10^7$ galaxies, with 4 million at $z > 2$.

For certain applications, for example, for the estimate of photometric redshifts discussed in the next section, it might be desirable to supplement the PS1 $grizy$ filter system with other bands, particularly in the near infrared. The UKIDSS Infrared Deep Sky Survey (e.g. Lawrence et al., 2007; Hewett et al., 2006) is particularly relevant in this context. The UKIDSS Large Area Survey (LAS) aims to map about 4000 sq deg of the Northern sky (contained within the $3\pi$ survey) over the course of a few hundred nights. The Deep Extragalactic Survey (DXS) aims to cover 35 square degrees of the sky in three separate regions which have a large overlap with the fields chosen for the MDS. Details of the $J$, $H$ and $K$ magnitude limits of the UKIDSS surveys are listed in Table 2.2. In order to assess the compatibility of the PS1 and UKIDSS surveys, we show in Fig. 2.6 the reduction in galaxy counts, relative to a pure $r$-band selection, that would result from combining in turn each of the filters with the $r$-band filter. We see, once again, that the $y$-band cut (green line) is much shallower than the other PS1 bands. The UKIDSS (LAS) $J, H$ and $K$ bands are even shallower. Combining $r$-band and $U$-band detections also results in a large reduction in the counts even for an optimistic $U$-band limit of 23 mag. Fig. 2.6 suggests that, in spite of the large area overlap with the $3\pi$ survey, the UKIDSS (LAS) survey may be too shallow to pick up PS1 galaxies at high redshifts. It will be very difficult for

a $U$-band survey to pick up a significant number of PS1 galaxies.

## 2.4 Photometric redshifts in the PS1 survey

We now examine the accuracy with which redshifts are likely to be estimated using PS1 photometry. For this purpose we adopt an off-the-shelf photometric redshift code, the Hyper-$z$ code of Bolzonella et al. (2000) which is based on fitting template spectra. We do not attempt to tune the performance of the estimator in anyway, and so our results should perhaps be regarded as providing a pessimistic view of the photometric redshift performance of PS1. Once PS1 data become available, bespoke estimators will be developed which are optimized to return the smallest random and systematic errors for the PS1 filter set and galaxies by having empirically adaptive galaxy templates (e.g. Bender et al., 2001).

The basic principle behind the template fitting approach to photometric redshift estimation is the following. The observed SED of a galaxy is compared to a set of template spectra and a standard $\chi^2$ minimisation is used to obtain the best fit:

$$\chi^2(z) = \sum_{i=1}^{N} \left[ \frac{F_{\rm obs,i} - b \times F_{\rm tem,i}(z)}{\sigma_i} \right], \tag{2.9}$$

where $F_{\rm obs,i}$, $F_{\rm tem,i}$ and $\sigma_i$ are the observed fluxes, template fluxes and the uncertainty in the flux through filter $i$, respectively and $b$ is a normalization factor. For the fitting procedure, we input the PS1 $grizy$-band filter transmission curves and, when appropriate, those of the UKIDSS near infrared bands and a $U$ band filter. We consider different reddening laws and two sets of model templates: the mean spectra of local galaxies given by Coleman et al. (1980, CWW) and the synthetic spectra given by Bruzual and Charlot (1993, BC). We set a redshift range of $0 < z < 3$ for the $3\pi$ and $0 < z < 4$ for the MDS sample.

One might be concerned that the use of Bruzual & Charlot stellar population synthesis models to generate both the template spectra and the galaxy spectra in the mock catalogues might lead to an underestimate of the error on the photometric redshift. There are two key differences between the mock spectra and the templates which mean that this is not an issue: i) the complexity of the composite stellar populations of mock galaxies and ii) the differing treatments of dust extinction. The template spectra correspond to a single parameter star formation history (characterized by an exponentially decaying star formation rate, where the $e$-folding time

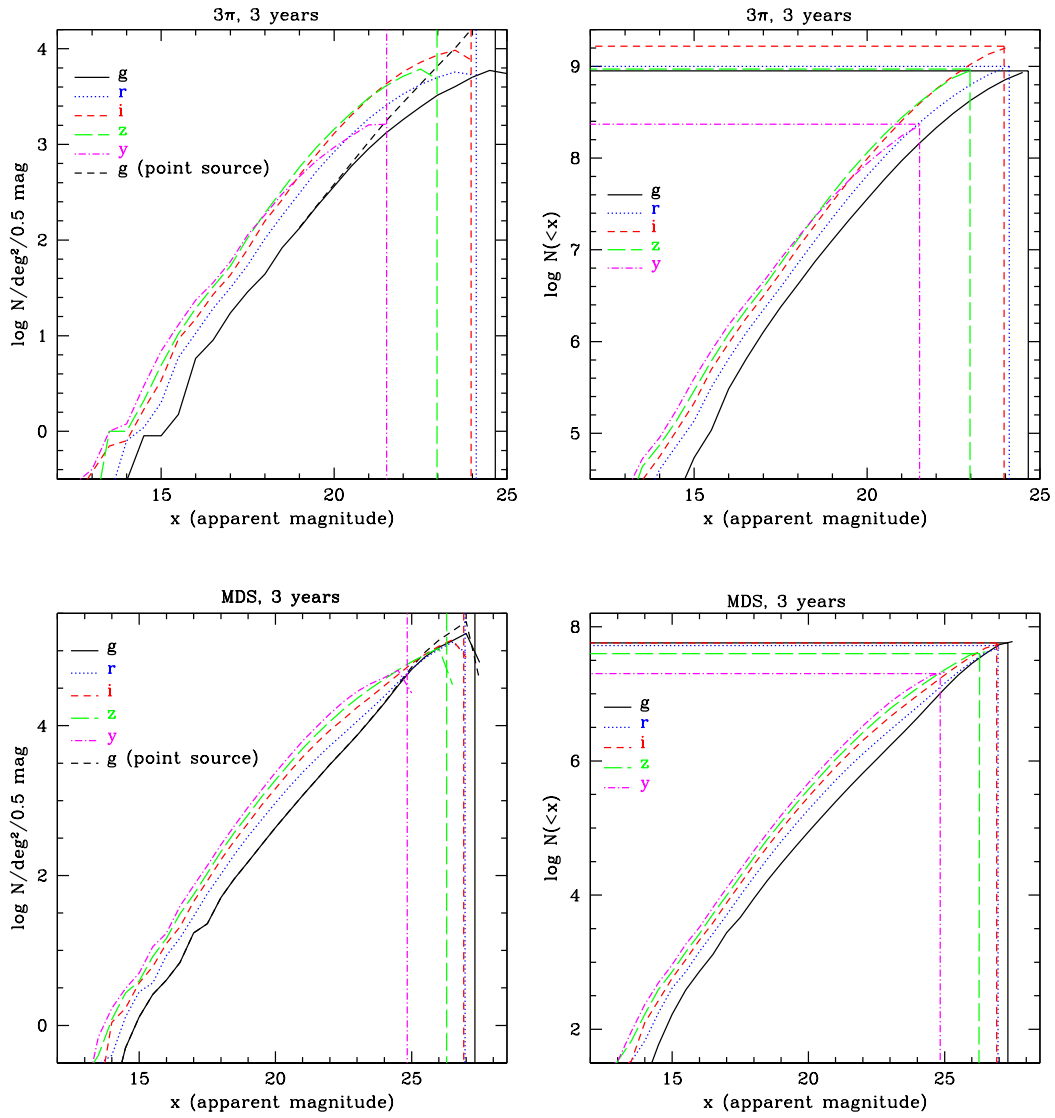


Figure 2.3: Expected galaxy number counts in the 3-year PS1 3$\pi$ survey (top panels) and the Medium Deep Survey (MDS) (bottom panels), as predicted by the GALFORM model. A 5$\sigma$ cut on Petrosian magnitudes has been used for selecting galaxies. Left: galaxy number counts in 0.5 magnitude bins per sq deg in the PS1 *g*, *r*, *i*, *z*, and *y* bands. The black dashed lines show the *g* band galaxy number counts limited only by the point source limits. Right: cumulative galaxy number counts as a function of magnitude, $N(< x)$, where $x$ denotes PS1 *g*, *r*, *i*, *z*, or *y* bands, as indicated in the legend. The straight lines show the 3-year 5$\sigma$ point source magnitude limits.

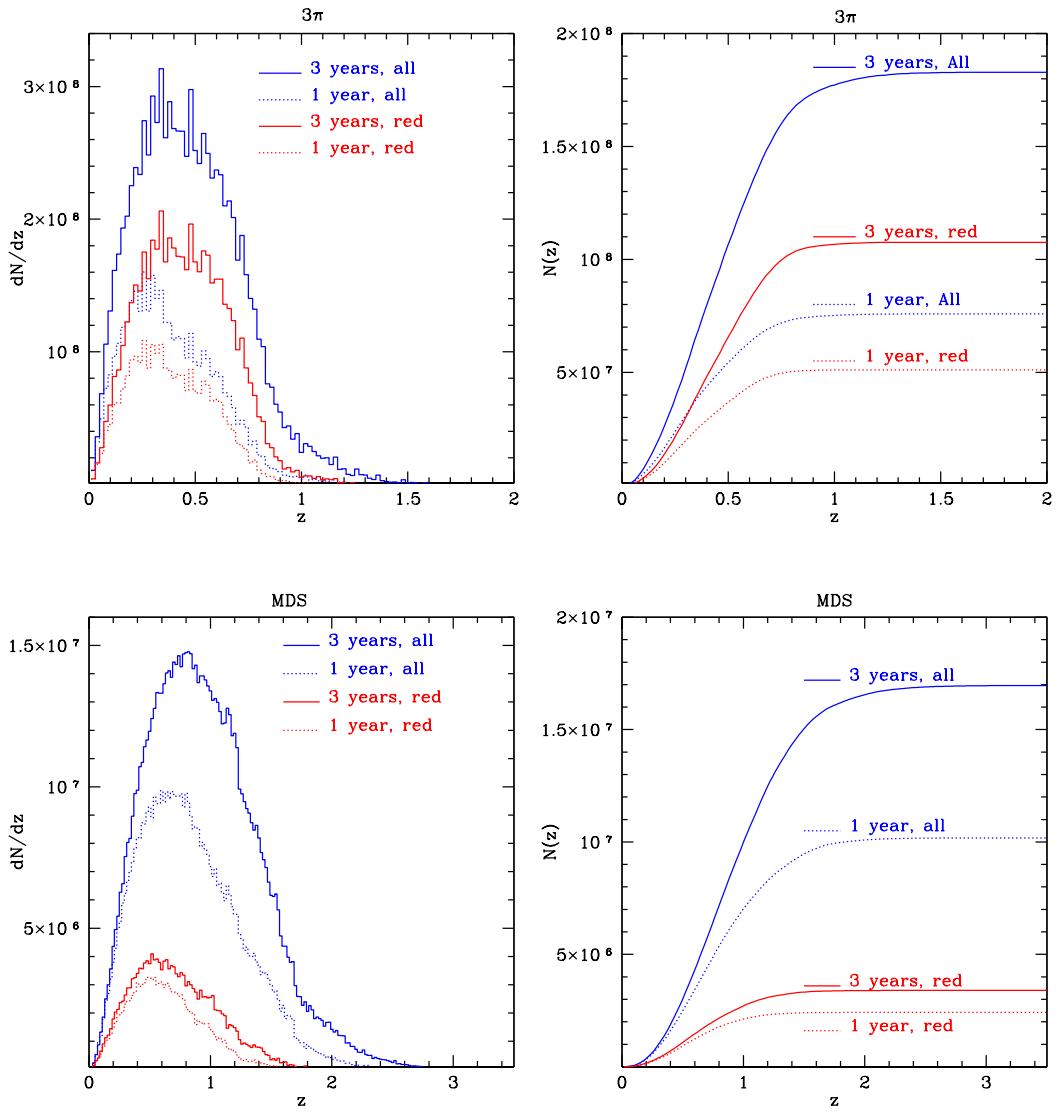


Figure 2.4: Expected galaxy redshift distributions for galaxies detected in all 5 $(g, r, i, z, y)$ PS1 bands in the $3\pi$ survey (top panels) and the Medium Deep Survey (MDS) (bottom panels), as predicted by the GALFORM model. The left-hand panels give the differential counts, in bins of $\Delta z = 0.02$. The right-hand panels give the cumulative counts. Blue lines show results for all galaxies while the red lines refer exclusively to red galaxies. Solid lines are for the 3-year surveys and dotted lines for the 1-year surveys. Red galaxies are selected by a rest-frame colour cut of $M_g - M_r > -0.04M_r - z/15 - 0.25$, where $z$ is the redshift (see Fig.2.14). Note that these predictions have been extrapolated from a mock catalogue which covers 10 square degrees, and so are noisier than would be expected for the actual survey sizes.

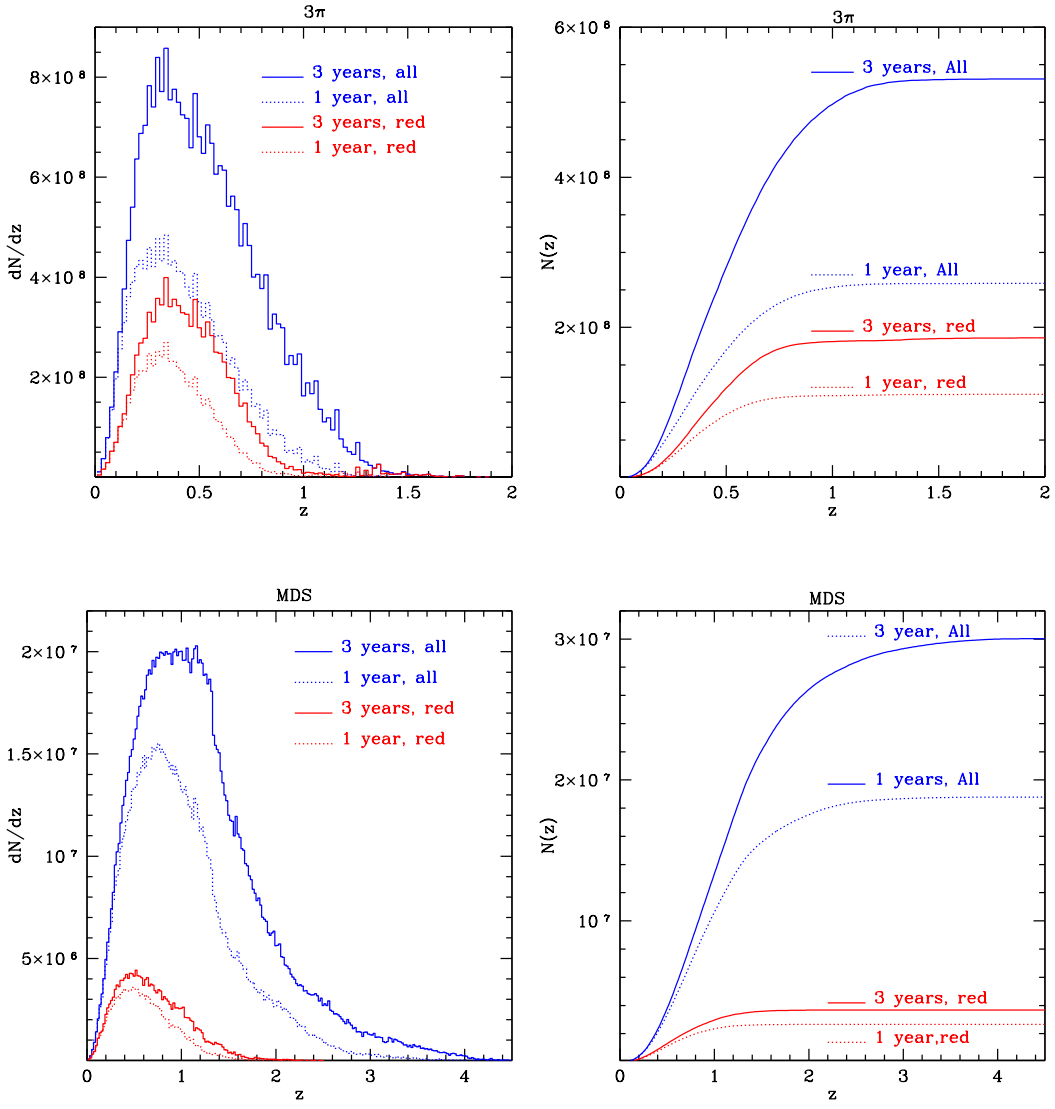


Figure 2.5: As Fig.2.4 but for galaxies required to be detected only in the $g, r, i$, and $z$ bands. Without requiring the shallow $y$-band detection the number of galaxies is about twice as large as with the full $g, r, i, z$ and $y$ constraints.

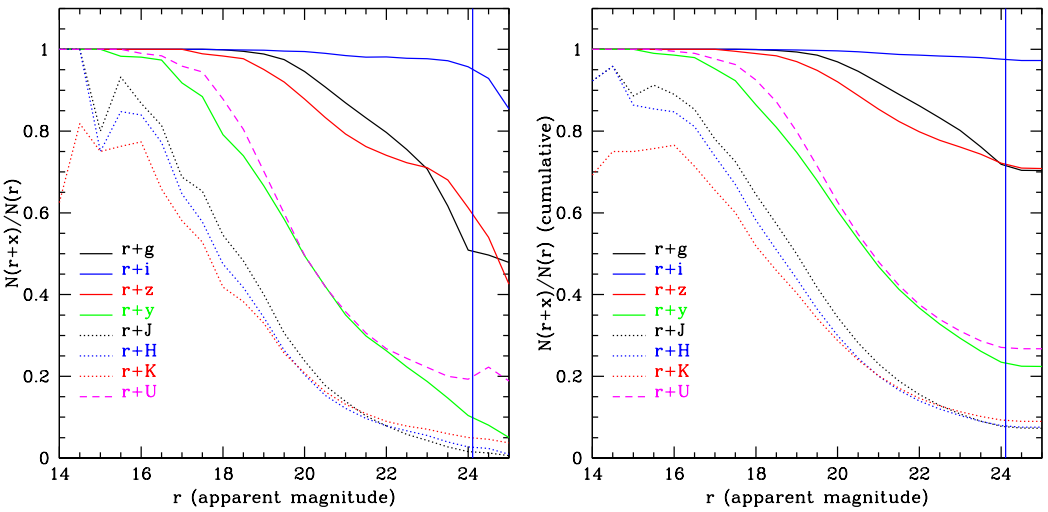


Figure 2.6: Ratio of differential (left) and cumulative (right) counts for galaxies selected using a combination of $r$-band and one other filter to the counts of galaxies selected using the $r$-band alone, as a function of $r$-band magnitude. For the additional filters, we use the UKIDSS $J, H$ and $K$ bands, the PS1 $g, i, z$, and $y$ bands and a $U$-band . For the PS1 *grizy* system, we adopt the third year magnitude cuts and for the UKIDSS bands the LAS limits; for the $U$-band we assume a limit of 23 mag. The label $r + x$ denotes that galaxies are selected by combining the $r$-band and one of the other bands. The vertical blue lines indicate the $r$-band $5\sigma$ point source detection limit after the 3-year surveys.

is treated as a parameter) and a fixed metallicity for the stars. The mock galaxies, on the other hand, have complicated star formation histories which cannot be fitted by a decaying exponential (see Baugh 2006 for examples of star formation histories predicted by the semi-analytical models). Furthermore, the stars in the mock galaxy have a range of metallicities. Hyper-$z$, in common with many other photometric redshift estimators, assumes that dust forms a foreground screen in front of the stars with a particular extinction law. In GALFORM, the dust and stars are mixed together. This more realistic geometry can lead to dust attenuation curves which look quite different from those assumed in the photometric redshift code (Granato et al., 2000).

The Hyper-$z$ code calculates a redshift probability distribution, $P(z)$, for each galaxy. Because of a degeneracy between the 4000 Å and the 912 Å breaks, the shape of $P(z)$ can have a double peak, causing some low redshift galaxies to be misidentified as high redshift galaxies and viceversa. Some of these misidentifications can be removed by applying extra constraints, for example, the galaxy luminosity function and the differential comoving volume as a function of redshift (Mobasher et al., 2007). For a given observed flux, both these functions provide an estimate of the probability that the galaxy has redshift $z$ which can be used to modulate $P(z)$. The highest peak in the combined probability distribution gives the best estimate of the photometric redshift. We use the $r$-band luminosity function of the B06 model for this purpose.

We now discuss how the accuracy and reliability of the photometric redshift estimates depends on various choices. We do this by calculating photometric redshifts for a 10 sq deg subsample of our mock PS1 $3\pi$ 3-year catalogue and comparing these with the true redshifts (which we will sometimes refer to as the "spectroscopic" redshifts.)

*1. Choice of SED template (CWW vs BC)*

Our tests show that using 5 input spectral types: burst, S0, Sa, Sc and Im, gives good results; adding more spectral types does not produce further significant improvement. We find that fitting with the CWW templates gives larger statistical uncertainties and systematic deviations from the true redshift than fitting with the BC templates, especially at high redshift ($z > 1$). The reason for this could be that the CWW templates are based on observations of the local universe and may not be sufficiently representative of galaxies at high redshift. In what follows, we will exclusively use the BC templates.

We also experimented with BC templates for different metallicities. Because of the age-metallicity degeneracy in galaxy SEDs, we did not find any improvement by allowing the metallicity to vary while letting the age of the stellar populations be a free parameter. Since the 4000 Å break only becomes detectable after a stellar population has aged beyond $10^7$ years, we exclude templates with ages smaller than this. This greatly improves the results for low redshift galaxies ($z < 0.5$).

*2. Dependence on photometric bands*

The accuracy of the redshift estimates depends on the choice of photometric bands. With our 10 sq deg 3-year mock catalogues, we can explore which combination of bands gives optimal results for PS1. We have considered many combination of the PS1 *grizy* photometry with UKIDSS (LAS) $JHK$ and fiducial $B$ and $U$ photometry. Note that, if the flux through any of the $U$, $B$, $J$, $H$ or $K$ filters drops below the $5\sigma$ flux limit, the noisy measured flux is still used with its appropriate uncertainty.

We find that the $B$-band (whose effective wavelength is very close to the $g$ band) does not improve the fits if $U$ is available, but the $U$-band is still useful even when $B$-band data are included. We also find that the $H$-band is not important provided $J$ and $K$ are available. However, both $J$ and $K$ are important for improving the quality of the fits. Therefore, in what follows we will ignore $B$ and $H$. Our results are displayed in Figs. 2.7 and 2.8. In Fig. 2.7, we plot the "spectroscopic" redshifts against our estimated photometric redshifts for the 4 cases above. For clarity, rather than plotting each galaxy on these plots, we have instead displayed contours that indicate the region in each bin of photo-$z$ that contains 50%, 70%, 90% and 95% of the galaxies. Galaxies with "spectroscopic" redshifts falling outside the 95% contours are shown individually by green dots. To evaluate the $1\sigma$ scatter we eliminate extreme outliers through standard $3\sigma$ clipping. Typically over $f_{\rm ret} = 95\%$ of the galaxies are retained, as indicated in the legend. Fig. 2.7 plots the true or "spectroscopic" redshift against our estimated photometric redshift for the PS1 *grizy* photometry alone and when supplemented by $U$-band photometry, UKIDSS (LAS) photometry, or both. Fig. 2.8 (left panel) shows $\Delta z/(1+z)$ plotted against redshift where $\Delta z$ is the $1\sigma$ error from Fig. 2.7. The bias in the mean of each redshift bin relative to the true value is also shown (right panel).

The PS1 *grizy* bands alone give relatively accurate photometric redshifts in the range $0.25 < z < 0.8$, with typical *rms* values of $\Delta z/(1+z) \sim 0.06$. The random and systematic errors increase at both lower and higher redshifts and there is a population

of low redshift ($z < 1$) galaxies which are incorrectly assigned high redshifts. Adding the $U$-band produces only a moderate improvement at all redshifts. Using both the $J$ and $K$ bands results in a significant improvement at $z < 0.5$, but not at higher redshifts. Finally, combining the $U$, $J$ and $K$, produces the best results. For this best case, the *rms* error, $\Delta z/(1+z) \sim 0.05$, in the range $0.5 < z < 1$ and, for $z < 1.2$, it is never larger than 0.15.

We saw in §2.3.3 that requiring that galaxies be detected in $y$, the shallowest PS1 filter, reduces the sample size by factors of 2-3. The deeper sample that we achieve by only requiring *griz* detections has significantly less accurate photo-$z$s. This is shown in Fig. 2.9, in which we measure photometric redshifts using only *griz* photometry. In this, the *rms* in the redshift range $0.25 < z < 0.8$ increases from 0.06 to 0.075 and the bias changes little.

Photometric redshift estimates for the MDS are shown in the top 2 panels of Fig. 2.12 and their accuracy is quantified by the green and blue lines in Fig. 2.13. If only the PS1 *grizy* are available, an accuracy of $\Delta z/(1+z) \sim 0.05$ is achievable for $0.02 < z < 1.5$. Adding the UKIDSS (DXS) and the $U$-band improves the estimates considerably, but there is still a clear bias at very low and high redshifts. This is mainly because the depths of the UKIDSS (DXS) and our assumed $U$ band is insufficient to match the depth of the MDS so faint galaxies are not detected in the UKIDSS $J$ and $K$ band nor in the $U$ band.

For certain applications, for example, the measurement of baryonic acoustic oscillations discussed in the next section, smaller *rms* errors than those found above are required. This can be achieved by selecting subsamples of galaxies whose spectra are particularly well suited for the determination of photometric redshifts, such as red galaxies which have strong 4000 Å breaks. The most direct way to define a red subsample is by using the rest frame $g-r$ colours. In Fig 2.14, we plot the predicted rest-frame $g-r$ against $r$-band luminosity at four different redshifts in our mock MDS catalogue. A cut at $M_g - M_r > -0.04M_r - z/15.0 - 0.25$ neatly separates out the red sequence, particularly at $z < 1$. The redshift distributions of red galaxies defined this way are shown by the red lines for both the $3\pi$ survey and the MDS in Figs. 2.4 and 2.5. The distributions peak at slightly lower redshifts than the full samples, but there is still an impressive number of red galaxies in the two surveys. For example, in the $3\pi$ survey we expect about 200 million galaxies after 3-years if detection in $y$ is not required or 100 million if it is.

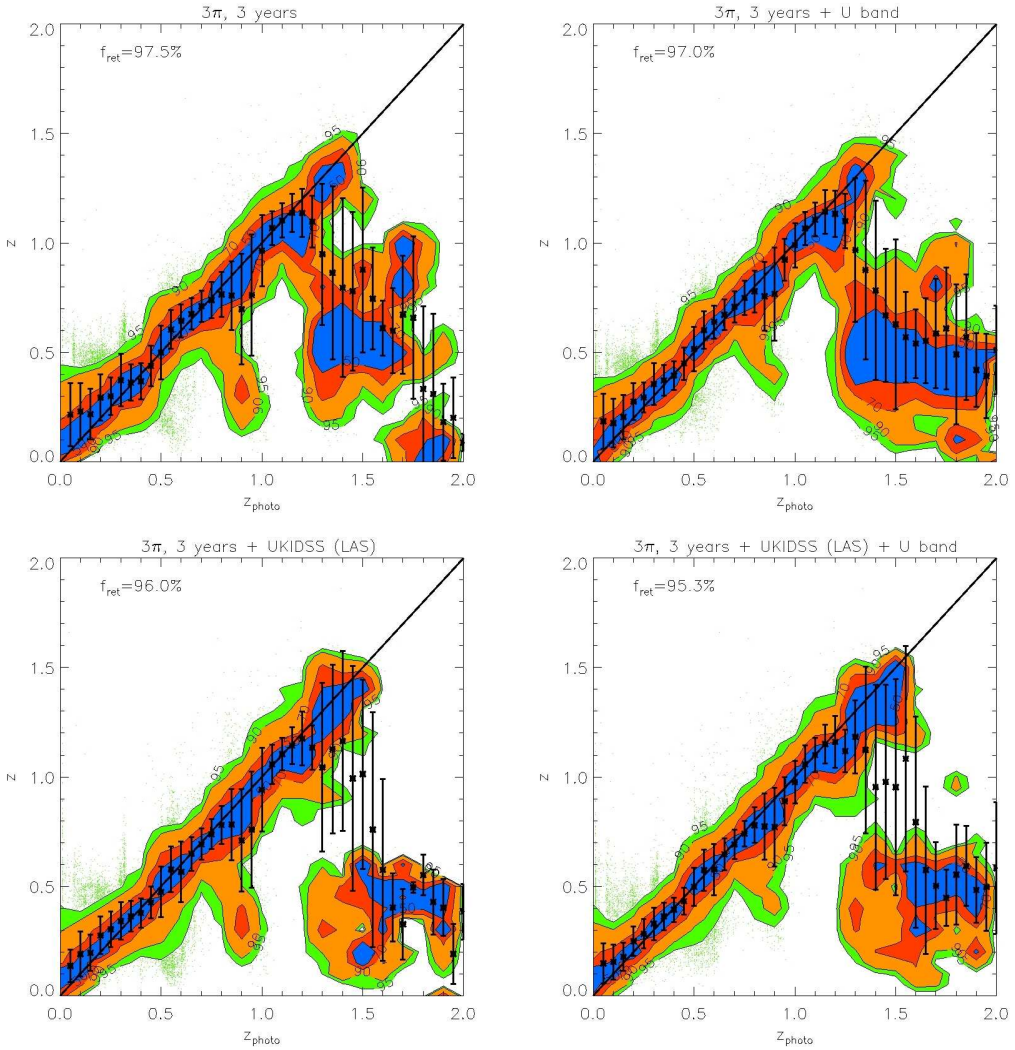


Figure 2.7: True ("spectroscopic") redshifts plotted against photometric redshifts in a 10 sq deg mock PS1 $3\pi$ 3-year galaxy catalogue. In each bin of photo-$z$ the contours show the regions containing 50% (blue), 70% (red), 90% (orange) and 95% (green) of the galaxies. Galaxies with true redshifts falling outside the 95% contours are shown by the green dots. Galaxies are selected by applying $5\sigma$ Petrosian magnitude cuts for all 5 PS1 *grizy* bands. If the flux in some other filters ($U$, $B$, $J$, $H$ or $K$) drops below its $5\sigma$ limit, the detected flux is still used with its uncertainty. The error bars show the *rms* scatter after $3\sigma$ clipping. The percentages of galaxies retained after the clipping are given in the legend. Top left: PS1 *grizy* band data only. Top right: PS1 *grizy* combined with $U$-band. Bottom left: PS1 *grizy* combined with UKIDSS (LAS) $J$ and $K$. Bottom right: PS1 *grizy*, $U$-band and UKIDSS (LAS) $J$ and $K$. The "island" at $z_{\rm photo} > 1.2$ and $z < 1$ contains only a few percent to about 10% of those galaxies within that true redshift bin.

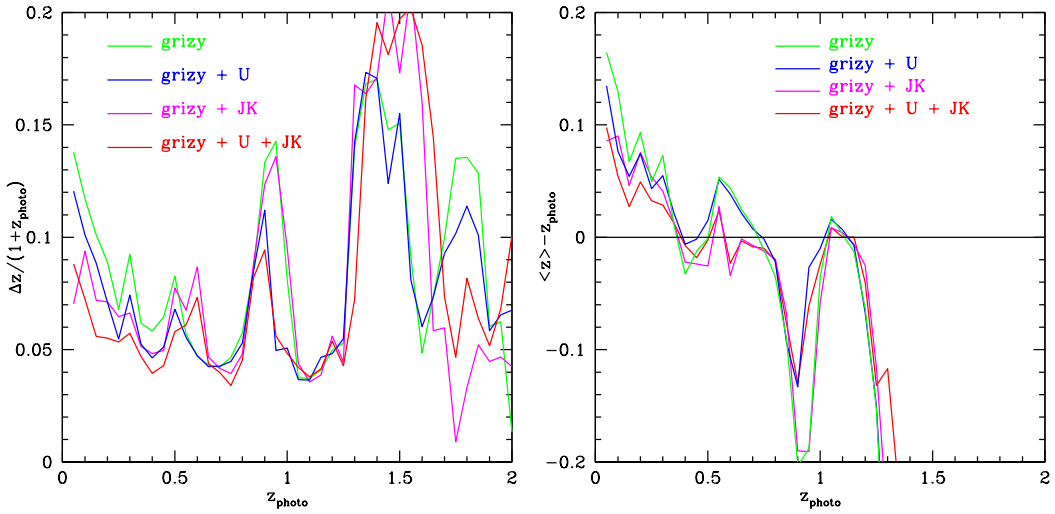


Figure 2.8: Accuracy of the photometric redshift estimates in a 10 sq deg mock PS1 $3\pi$ 3-year galaxy catalogue. Only galaxies remaining after applying a $3\sigma$ clipping procedure to the binned data are retained in the estimate. The retained fractions are given in the legend of Fig. 2.7. We use a redshift bin size of $\Delta z = 0.05$. Left panel: $1\sigma$ uncertainty divided by $(1+z)$ plotted against the photo-$z$ Right panel: Systematic deviation of the mean photometric redshift in each bin from the true value, as a function of photo-$z$.

In practice, rest-frame $g - r$ colours are difficult to estimate from the observations. An alternative method for identifying red galaxies is to use the spectral type determined by Hyper-$z$. We define a red sample by the following criteria, galaxies which are best fit with the 'Burst' spectral type and a stellar population older than $10^9$yr.

Fig. 2.15 shows the redshift distribution for this sample which can be seen to be very similar to the redshift distribution of a red sample selected by rest-frame $g - r$ colour. This suggests that it will be possible to select a red galaxy sample directly from the observational data alone.

Fig. 2.10 and Fig. 2.12 show photometric redshift estimates for red galaxies in the 3-year $3\pi$ survey and the MDS respectively. Their accuracy is illustrated by the magenta (*grizy* photometry only) and red lines (*grizy*+*JK*+*U*) in Figs. 2.11 and Fig. 2.13 respectively. Results without the $y$-band photometry are shown in the top

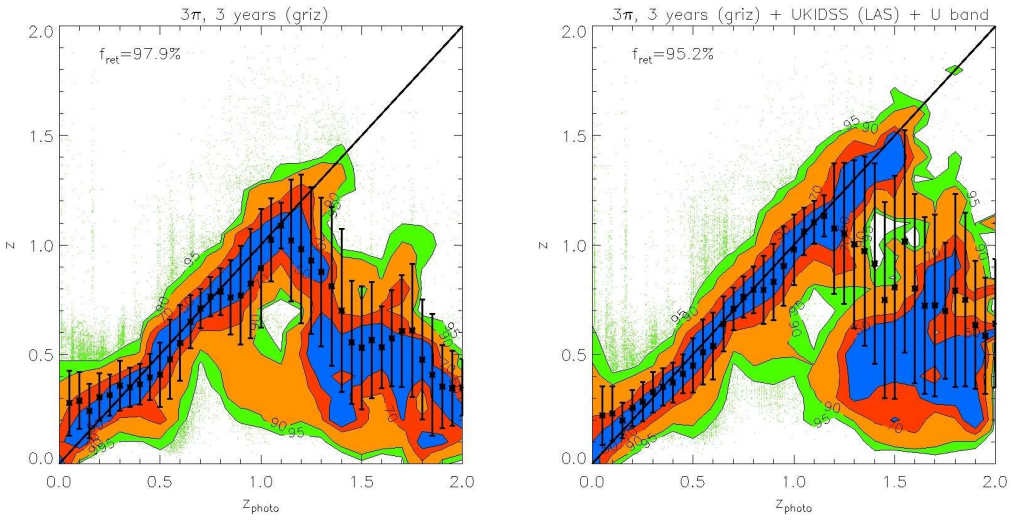


Figure 2.9: As Fig. 2.7, but using a larger, deeper sample by not requiring a $y$ band detection and using only $griz$ fluxes in the determination of photometric redshifts. Without the $y$-band, more galaxies are detected, but the error and bias in the photometric redshifts increase. Left panel: results when using only the PS1 photometry. Right panel: results when adding UKIDSS (LAS) $J, K$-band and with $U$-band photometry.

panels of Fig. 2.10 and in green ($griz$ photometry only) and blue ($griz$+$JK$+$U$) lines in Fig. 2.11. These figures show the dramatic improvement in photometric redshift accuracy for red galaxy samples. For example, for the $3\pi$ survey, the *rms* value of $\Delta z/(1+z)$ can be as low as 0.02 at $z \sim 0.8$ when combining $grizy$ with UKIDSS (LAS) and $U$ bands measurements. Similarly, in the MDS with the same combination of filters, the accuracy for red galaxies is much higher than for the sample as a whole and can be as good as $\Delta z/(1+z) \sim 0.03$ in the redshift range $0.75 < z < 2.5$.

Finally, we consider the form of the distribution of the photo-$z$ errors in Fig. 2.16. The photo-$z$ error distributions are well fitted by a Gaussian function, with variance $\sigma_z \approx \Delta_z$. The error distribution could also be equally well fitted by a Lorentzian function. Example distributions are shown at $z \sim 0.3$ and $\sim 0.5$ in Fig. 2.16. An application of our results for the size and form of the photo-$z$ errors is presented in the next section, in which we investigate their effect on the baryonic acoustic oscillation measurements.

To summarise this sub-chapter, we have assessed the photo-$z$ performance of PS1 using our mock catalogues. We found an accuracy in the $3\pi$ survey of $\Delta z/(1+z) \sim$

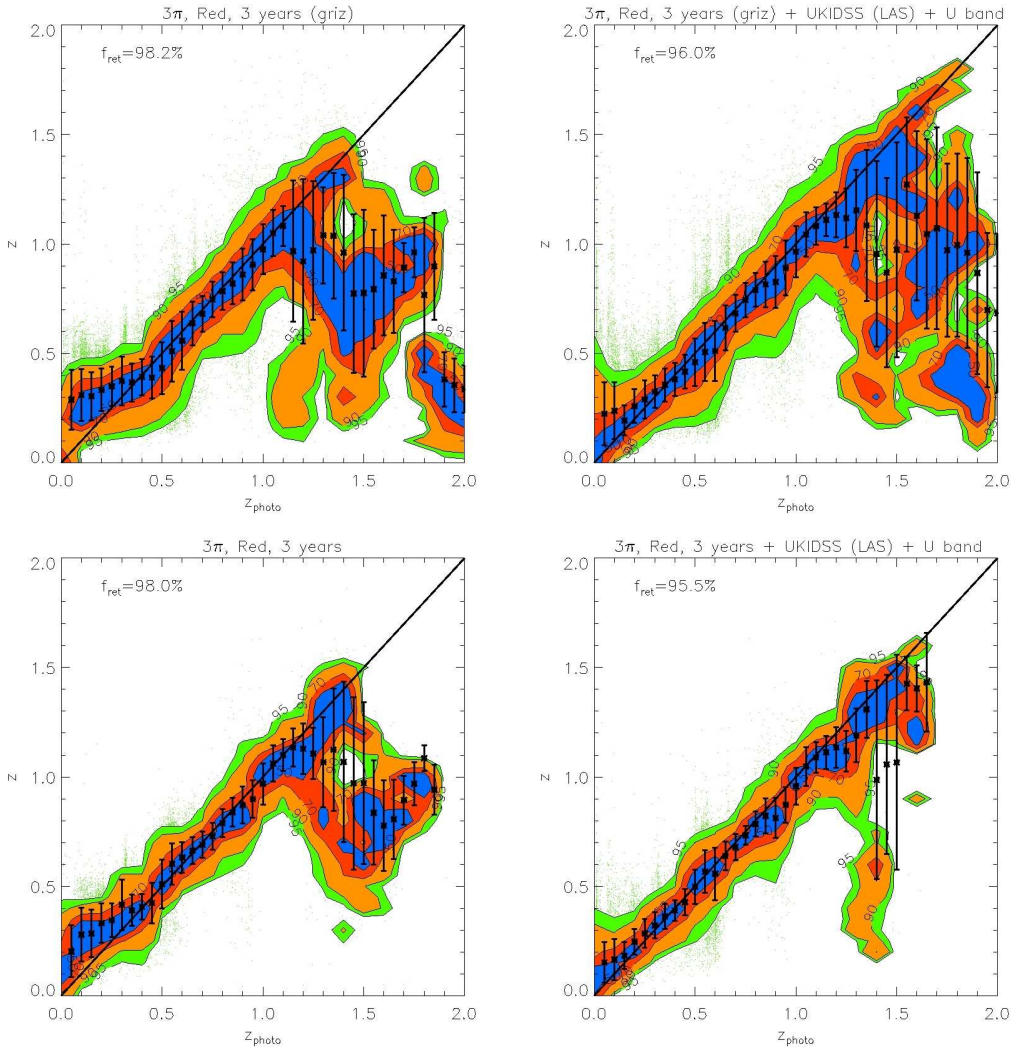


Figure 2.10: "Spectroscopic" versus photometric redshifts, as in Fig. 2.7 and Fig. 2.9, but for galaxies that are required to be red in their rest frame $g-r$ colour. Top panels: deep samples in which no $y$-band detection is required. The left hand panel makes use of only PS1 $griz$ photometry, while the right hand panel makes use of additional UKIDSS (LAS) $J, K$-band and fiducial $U$-band photometry. Bottom panels: These panels show the results for the shallower sample in which detections in all 5 ($grizy$) PS1 bands are required. Again the left hand panel uses only PS1 data and the right hand panel makes use of additional UKIDSS (LAS) $J, K$-band and fiducial $U$-band photometry.

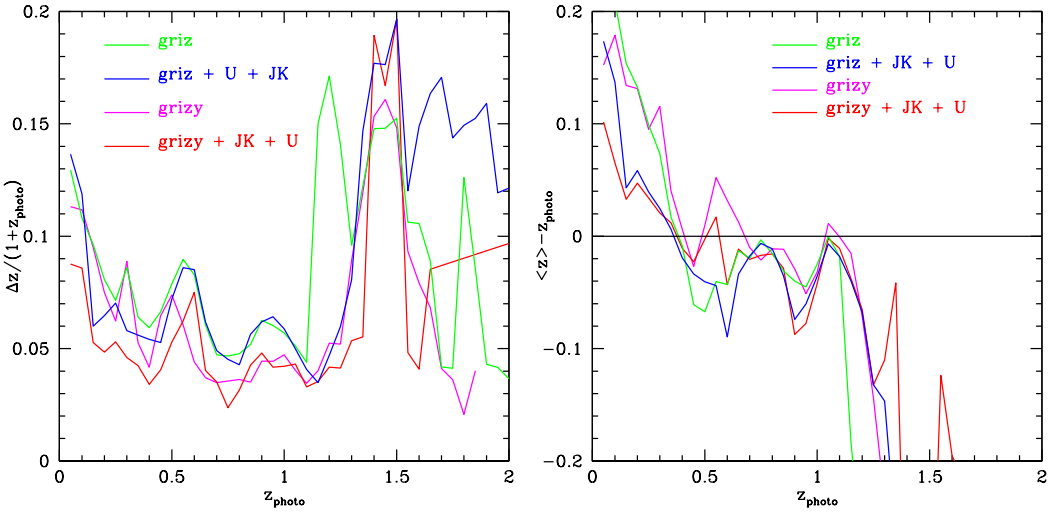


Figure 2.11: Accuracy of the photometric redshift estimates in a 10 sq deg mock PS1 $3\pi$ 3-year red galaxy catalogue. Results using only *griz* fluxes in the determination of photometric redshifts are shown together. Without the *y*-band, more galaxies detected, but the error and bias in the photometric redshifts increase. Only galaxies remaining after applying a $3\sigma$ clipping procedure to the binned data are plotted. We use a redshift bin size of $\Delta z = 0.05$. Left panel: $1\sigma$ uncertainty divided by $(1 + z)$ plotted against the photo-$z$. Right panel: Systematic deviation of the mean photometric redshift in each bin from the true value, as a function of photo-$z$.

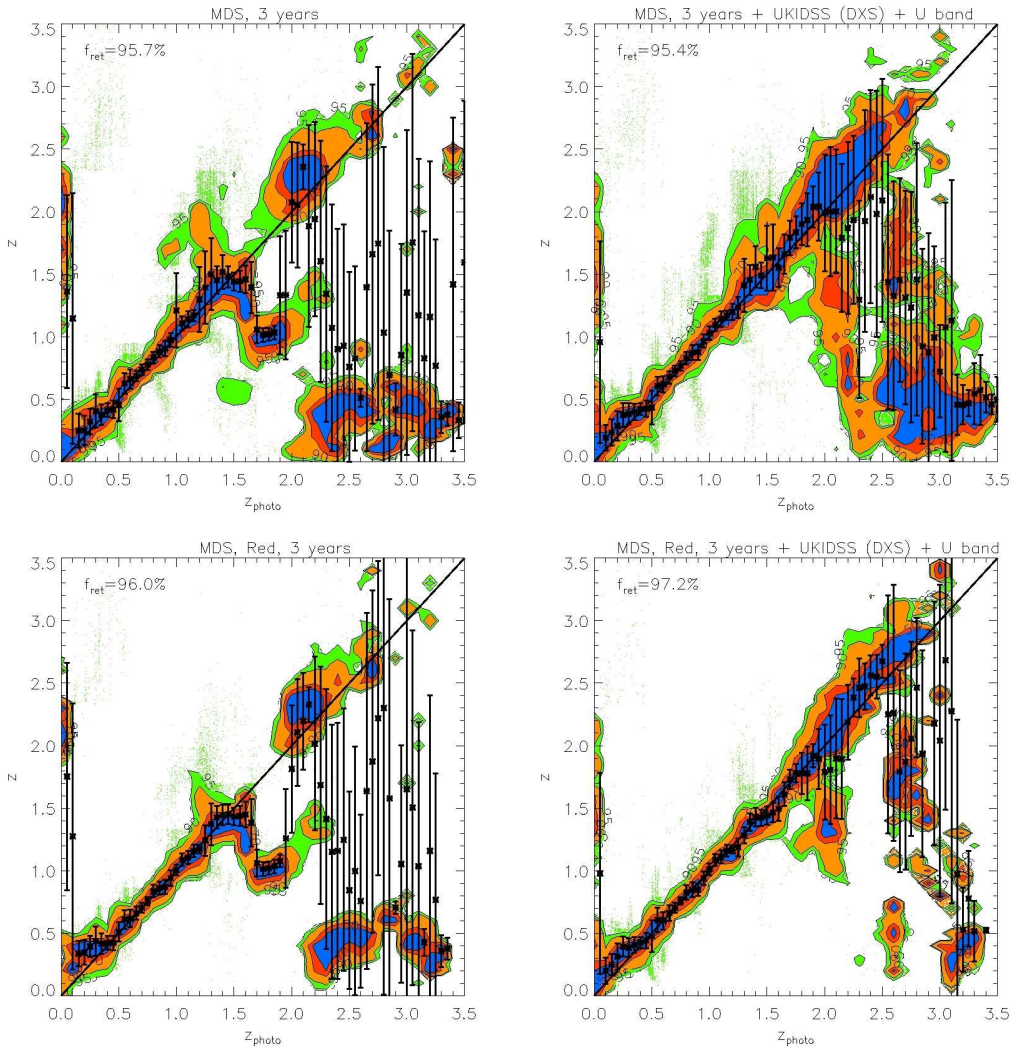


Figure 2.12: True ("spectroscopic") redshifts plotted against photometric redshifts for the 3-year MDS survey. The data are presented in the same fashion as in Figs 2.7,2.8 and 2.12, but for the MDS we extend the redshift range to $z = 3.5$. Top panels: predictions for the 3-year MDS using 1 sq deg mock catalogues. Bottom panels: predictions for samples of red galaxies. Left panels, results by using only the *grizy* photometry. Right Panels, results by adding UKIDSS (DXS) $J, K$-band and with $U$-band photometry. Galaxies are selected applying $5\sigma$ Petrosian magnitude cuts for all 5 PS1 *grizy* bands. If the flux in some other filters ($U$, $B$, $J$, $H$ or $K$) drops below its $5\sigma$ limit, the detected flux is still used with its uncertainty. The error bars show the *rms* scatter after $3\sigma$ clipping. The percentages of galaxies retained after the clipping are given in the legend.

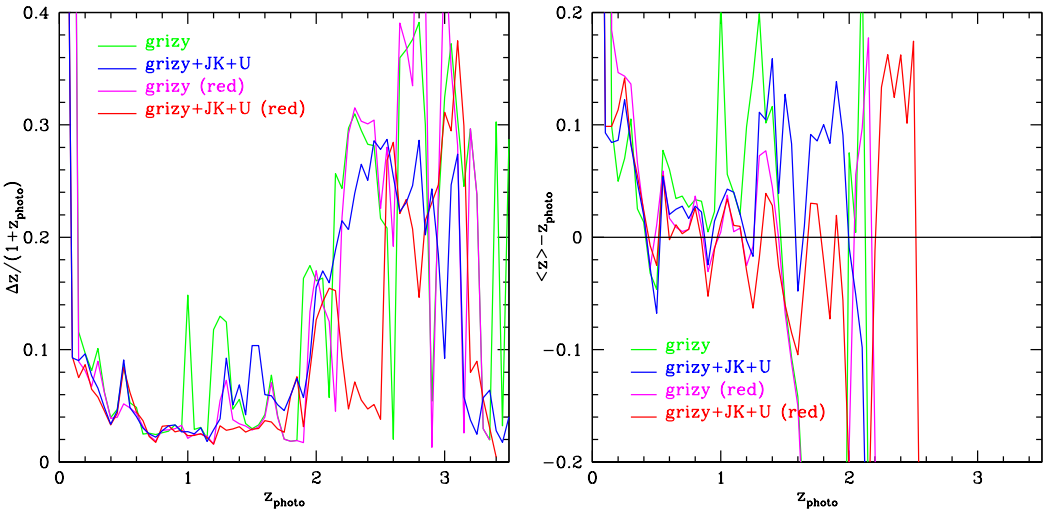


Figure 2.13: Accuracy of the photometric redshift estimates for the 3-year MDS survey shown in Fig. 2.12. Only galaxies remaining after applying a $3\sigma$ clipping procedure to the binned data are plotted. Galaxies are binned in the spectroscopic redshift axis with bin size $\Delta z = 0.05$. Left panel: $1\sigma$ uncertainty divided by $(1+z)$ plotted against the photo-$z$. Right panel: Systematic deviation of the mean photometric redshift in each bin from the true value, as a function photometric redshift.

0.06 in the range $0.25 < z < 0.8$ is achievable. Adding near infrared bands and blue band photometries can help to improve the photo-$z$ accuracy, but they need to be very deep. A great improvement in photometric redshift accuracy can be achieved for samples containing only red galaxies.

## 2.5 Implications for BAO Detection

In this section we investigate the impact of using photometric redshifts on the accuracy with which the baryonic acoustic oscillation (BAO) scale can be measured from the power spectrum of galaxy clustering. BAOs have been proposed as a standard ruler with which the properties of the dark energy may be measured (Blake and Glazebrook, 2003; Linder, 2003). Our aim here is to provide a simple quantification of the factor by which the effective volume of a survey is reduced when photometric redshifts are used in place of spectroscopic redshifts. This will provide a rule of thumb indicator of the relative performance of photometric and spectroscopic sur-

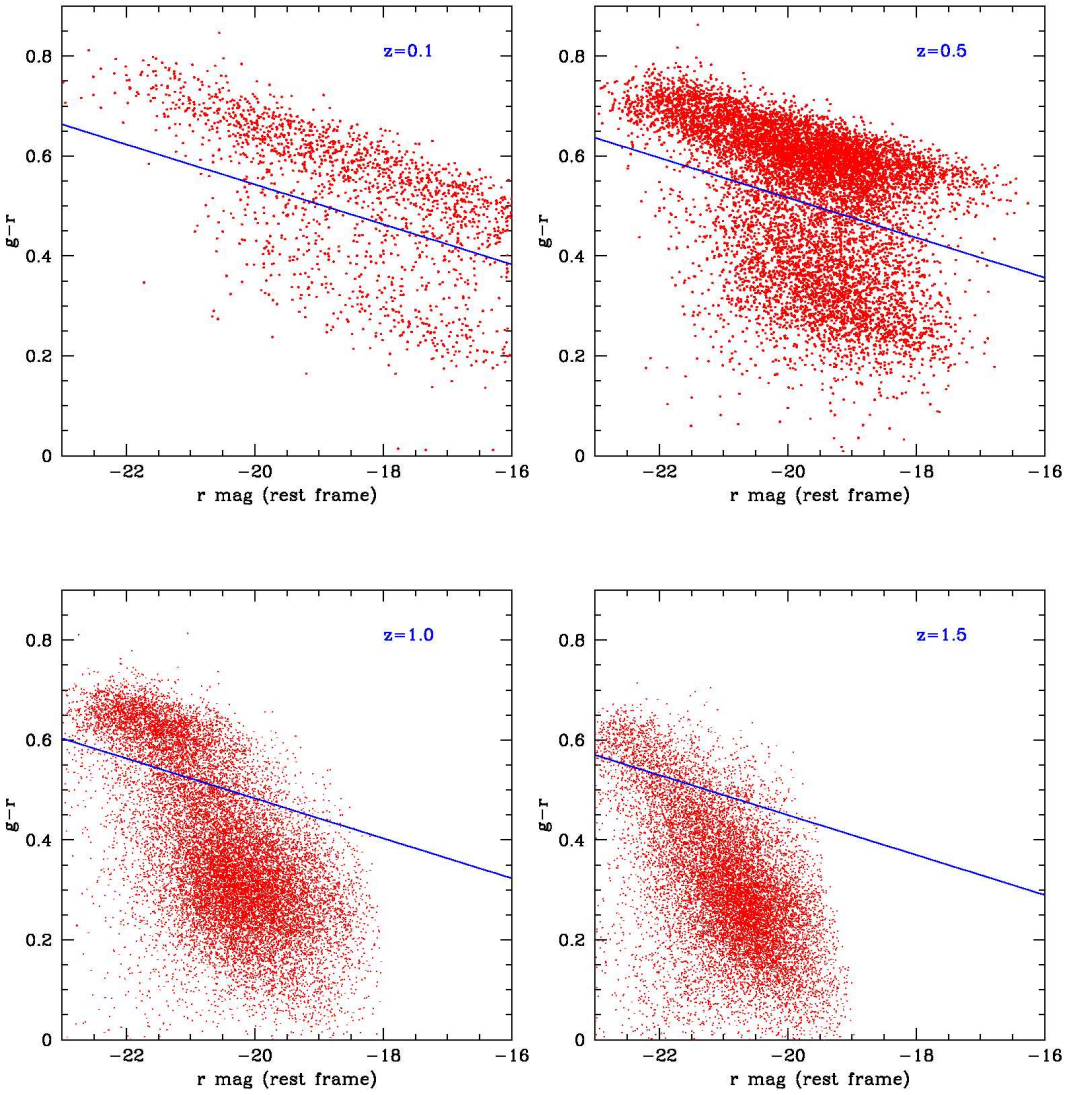


Figure 2.14: Expected colour-magnitude relation for the MDS 3-year mock catalogue. The plots show rest-frame $g - r$ colour *versus* rest-frame $r$-band magnitude predicted by GALFORM at the redshifts given in each panel. The blue line is $M_g - M_r = -0.04M_r - z/15.0 - 0.25$, where $z$ is the redshift. Galaxies above the line make up the "red" sample.

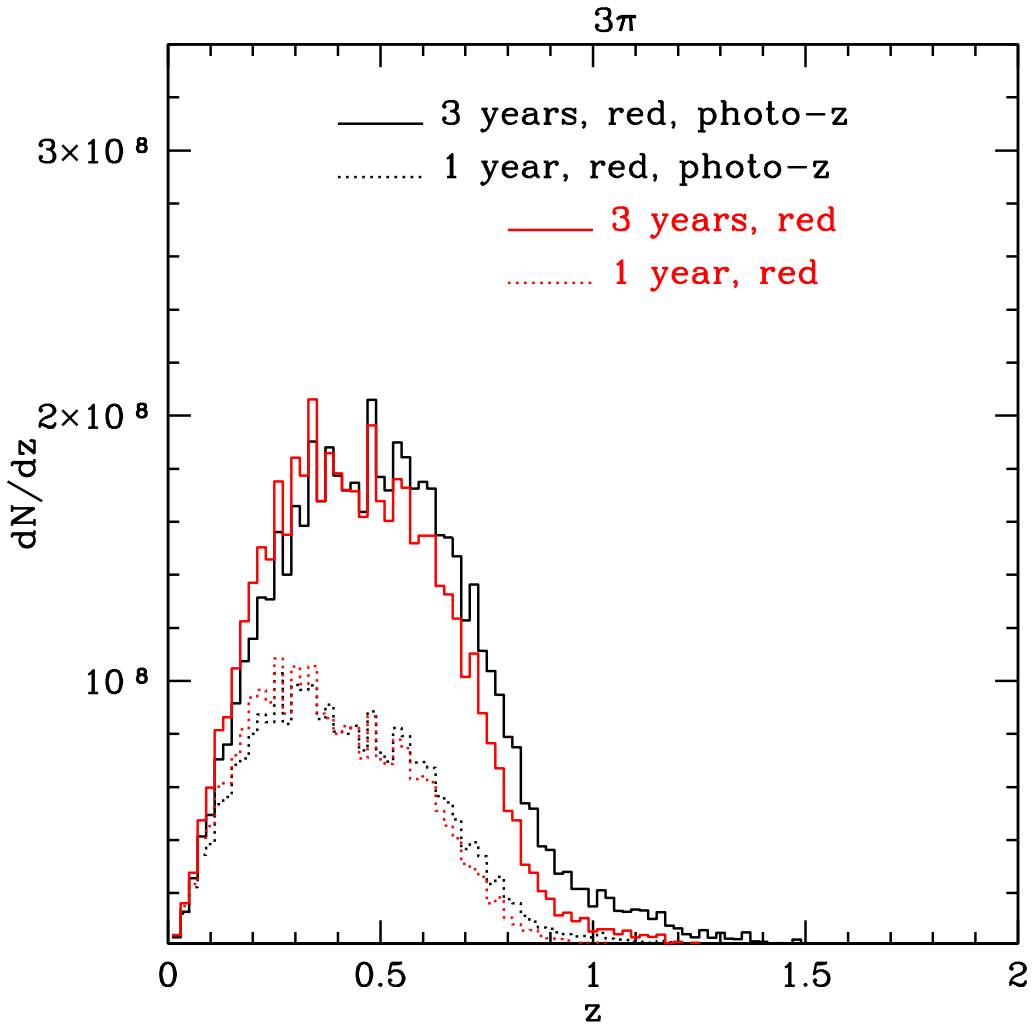


Figure 2.15: Predicted redshift distributions for "red" galaxies in the PS1 3$\pi$ survey, selected in two different ways. The red lines show results for a sample selected by rest-frame $g - r$ colour (according to $M_g - M_r > -0.04M_r - z/15 - 0.25$); the black lines show results for a sample selected by the best fit photo-$z$ spectral type, with detail in the text. The redshift bin is $\Delta z = 0.02$. The good agreement between the two selection methods suggests that it may be possible to select the red sample directly from the observed photometry.

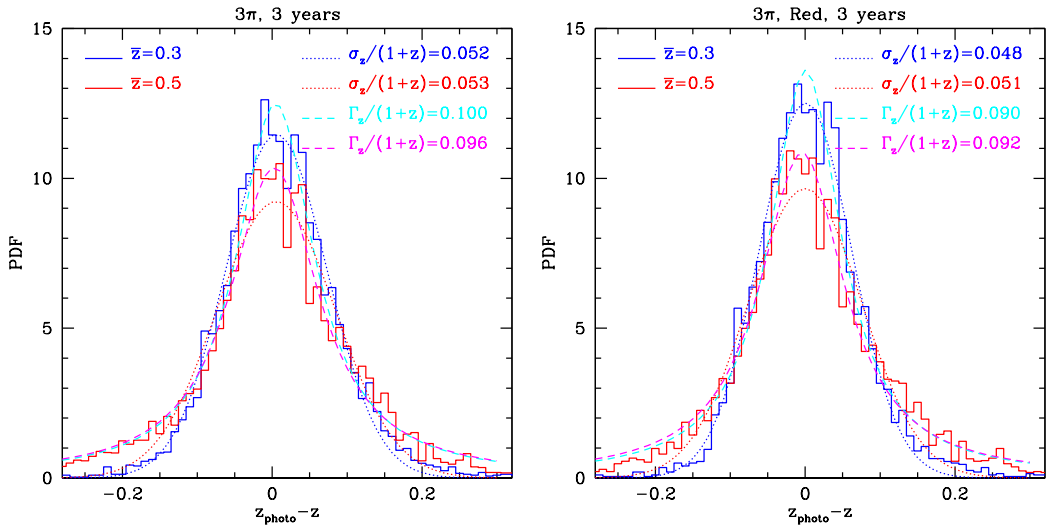


Figure 2.16: The distribution of photo-$z$ errors at redshift $z \sim 0.3$ and $z \sim 0.5$ for the 3-year $3\pi$ galaxy catalogues. The histograms are normalized to integrate to unity. Histograms in blue ($z \sim 0.3$) and red ($z \sim 0.5$) show the errors resulting from combining the *grizy* bands with UKIDSS (DXS) $J, K$-band and with $U$-band photometry. They could be equally well fitted by Gaussian and Lorentzian distributions. $\sigma_z$ is the *rms* width of the Gaussian function and $\Gamma_z$ is the FWHM of the Lorentzian function. Dotted lines show the best-fit Gaussians and the dashed lines illustrate the best-fit Lorentzian functions. Left: All galaxies, Right: Red galaxies.

veys for the measurement of BAO. We defer a more extensive treatment of the full impact of the survey window function on the measurement of BAOs to a later work. Mocks with clustering will play an important role in assessing the optimal way to measure the clustering signal in photometric surveys.

The photometric redshift technique allows large solid angles of sky to be covered to depths exceeding those accessible spectroscopically at a low observational cost. However, the inaccurate determination of a galaxy's redshift results in an uncertainty in its position and this leads to a distortion in the pattern of galaxy clustering. We shall refer to a measurement of the power spectrum which uses photometric redshifts to assign radial positions as being in "photo-$z$" space.

The errors introduced by photometric redshifts can be modelled as random perturbations to the radial positions of galaxies. As we have found from our photo-$z$ measurements that the photo-$z$ errors can be well fitted by a Gaussian function, if we assume that these perturbations are Gaussian distributed with mean equal to the true redshift and width $\sigma_{\rm z} \approx \Delta z$, then the Fourier transform of the measured density field, $\delta_{\rm pz}(\underline{k})$, can be written as

$$\delta_{\rm pz}(\underline{k}) = \delta_{\rm z}(\underline{k})\ \exp(-0.5 k_{\rm z}^2\, \sigma_{\rm z}^2), \tag{2.10}$$

where $k_{\rm z} = \underline{k}.\underline{\hat{z}}$, $\underline{\hat{z}}$ is the line-of-sight direction and $\delta_{\rm z}(\underline{k})$ is the density field measured in redshift space. From this expression, the spherically averaged power spectrum can be approximately[1] written as:

$$P_{\rm pz}(k) = P_{\rm z}(k)\, \frac{\sqrt{\pi}}{2}\, \frac{{\rm Erf}({\rm k}\, \sigma_{\rm z})}{k\sigma_{\rm z}}, \tag{2.11}$$

where ${\rm Erf}(x) = \frac{2}{\sqrt{\pi}} \int_0^x \exp(-t^2){\rm dt}$ is the error function. In addition, the power spectrum in photo-$z$ space can be seen as that in redshift space with additional damping on small scales due to the large value of $\sigma_z$. On very large scales the main contribution to the power spectrum comes from modes with wavelengths larger than the typical size of the photometric redshift errors. Therefore, the clustering on these scales is essentially unaffected. On the contrary, on scales comparable to and smaller than the photo-$z$ errors, structures are smeared out along the line-of-sight. The modes describing these scales along the line-of-sight contain little information about the true distribution of galaxies and contribute only noise to the power spectrum.

[1]It is an approximate expression since the redshift space distortions and photometric redshift errors do not commute under a spherical average (see Peacock and Dodds, 1994).

We investigate these effects directly on the measurement of the matter power spectrum using large N-body simulations. We use the L-BASICC ensemble of Angulo et al. (2008), which consists of 50 low-resolution, large volume simulations. Each has a volume of $2.4(\mathrm{Gpc}/h)^3$ and resolves halos more massive than $1 \times 10^{13}\,\mathrm{M}_\odot/h$. The assumed cosmological parameters are $\Omega_m = 0.25$, $\Omega_\Lambda = 0.75$, $h = 0.73$, $n = 1$ and $\sigma_8 = 0.9$. Their huge volume makes the L-BASICC simulations ideal to study the detectability of BAO in future surveys. Photometric redshift errors are mimicked as a random perturbation added to the particles' position along one direction (line-of-sight). The perturbations are drawn from a Gaussian distribution with various widths representing different degrees of uncertainty in the photometric redshift. Despite their large volume, the L-BASICC boxes are more than an order of magnitude smaller than the volume which will be covered by the $3\pi$ survey. Hence, we present results for the *relative* change expected in the random errors for different photometric redshift errors. Angulo et al. found that any systematic error in the recovery of the BAO scale was comparable to the sampling variance between L-BASICC realizations. To address the question of systematic errors we will need to use even larger volume simulations. Furthermore, new estimators are likely to be developed to extract the optimal BAO signal from photometric surveys.

In the upper panels of Fig. 2.17 we show the mean, spherically averaged power spectrum of the dark matter measured from the L-BASICC simulations at $z = 0.5$, along with its variance, in photo-$z$ space (solid blue lines). The size of the photo-$z$ errors are $\sigma_z = 0.01$ and $\sigma_z = 0.04$ (equivalent to 15.8 and 63.4 $h^{-1}$Mpc at $z = 0.5$) in the left- and right-hand panels respectively. We have also plotted the power spectrum measured in redshift-space (solid red lines) and the analytical expression of Eq. 2.11 (dashed red line). By comparing the spectra in redshift and photo-$z$ spaces, the additional damping described above is evident. Also, we see that Eq. 2.11 describes quantitatively this extra damping on scales where the power spectrum is not shot-noise dominated.

In the lower panels of Fig. 2.17 we take a closer look at the BAO by isolating them from the large-scale shape of the power spectrum. We do this by dividing the power spectrum by a smoothed version of the measurement. It is clear that since the number of "noisy modes" increases with the size of the photometric redshift errors, the error on the power spectrum and therefore on the BAO also increases. The visibility of the higher harmonic BAO is also reduced as the photometric redshift

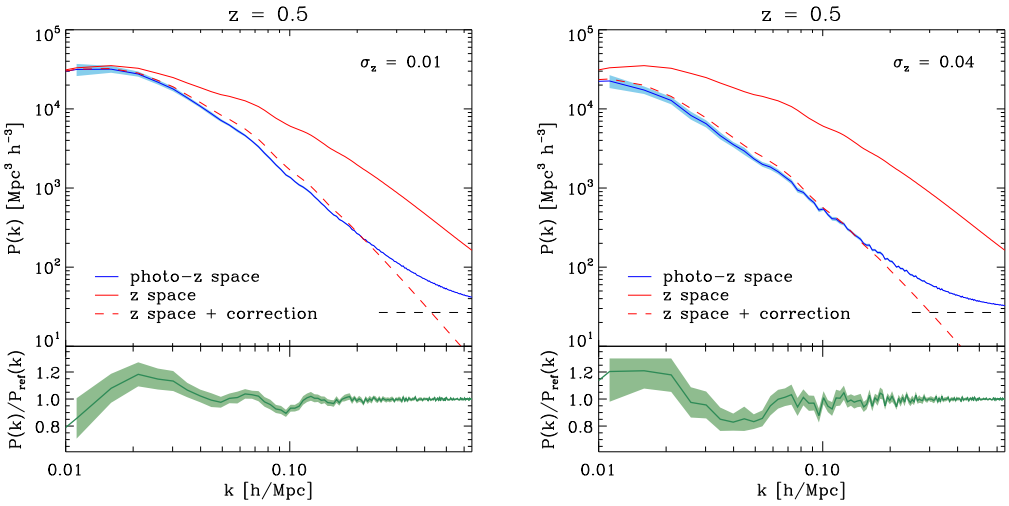


Figure 2.17: The mean and standard deviation of the dark matter power spectrum averaged over an ensemble of 50 N-Body simulations at $z = 0.5$. The top-panels display the power spectrum in three different cases: (i) redshift space (solid red line), (ii) photo-$z$ space (blue line) in which the position of each dark matter particle has been perturbed to mimic the effect of photometric redshift errors, and (iii) the photo-$z$ space power spectrum derived from Eq. (2.11) and the measured redshift space power spectrum (red dashed lines). The horizontal dashed line illustrates the shot-noise level. In the bottom panels we plot the photo-$z$ power spectrum divided by a smooth reference spectrum. This reveals the impact of photometric redshift errors directly on the baryonic acoustic oscillations (BAO). An increase in these errors causes an increase in the noise and a decrease in the amplitude of the BAO at high wavenumber. This implies that photometric redshifts affect scales much larger that the photometric redshift errors due to an effective reduction of the number of Fourier modes and the smearing of the underlying true clustering.

error increases. In order to quantify the loss of information, we have followed a standard technique to measure BAO as described in Angulo et al. (2008) (see also Percival et al., 2007 and Sanchez et al., 2008). The method basically consists of dividing the measured power spectrum by a smoothed version of the measurement. In this way, any long wavelength gradient or distortion in the shape of the power spectrum is removed which diminishes the impact of possible systematic errors due to redshift space distortions, galaxy bias, nonlinear evolution and, in the case described in this chapter, photometric redshift distortions. Then, we construct a model ratio using linear perturbation theory, $P_{\rm lt}/P_{\rm smooth}$, which we fit to the measured ratios. In the fitting procedure there are two free parameters: (i) a damping factor to account for the destruction of BAO peaks located at high $k$ by non-linear effects and redshift-space distortions and (ii) a stretch factor, $\alpha$, which quantifies how accurately we can measure the BAO wavelength. The latter gives a simple estimate of how well we can constrain the dark energy equation of state from BAO measurements alone.

Fig 2.18 shows the results of applying our fitting procedure to the L-BASICC ensemble at different redshifts. On the $x$-axis we plot the size of the photometric redshift error divided by $(1 + z)$, whilst on the $y$-axis we plot the predicted error on $\alpha$ divided by the error we infer for an ideal spectroscopic survey (i.e. from the power spectrum in redshift-space). Since the error on $\alpha$ scales with the error on the power spectrum and the latter is proportional to the square root of the volume of the survey, the $y$-axis should be roughly equal to the square root of the factor by which the volume of a photometric redshift needs to be larger than the volume of a spectroscopic survey to achieve the same accuracy.

Several authors have investigated the implications of photometric redshift errors on the clustering measurements in general and on the BAO in particular (Seo and Eisenstein, 2003; Amendola et al., 2005; Dolney et al., 2006; Blake and Bridle, 2005). Our analysis improves upon these studies in several ways: (i) we have included photometric redshift errors directly into realistic distribution of objects; (ii) by using N-body simulations, our calculation takes into account the effects introduced by nonlinear evolution, nonlinear redshift-space distortions and shot noise; (iii) the use of 50 different simulations enables a robust and realistic estimation of the errors on the power spectrum measurements; (iv) we have investigated how our results change if we use the actual distribution of photometric redshift errors (the cyan and brown circles in Fig 2.18), instead of a Gaussian fit and we find only a small additional

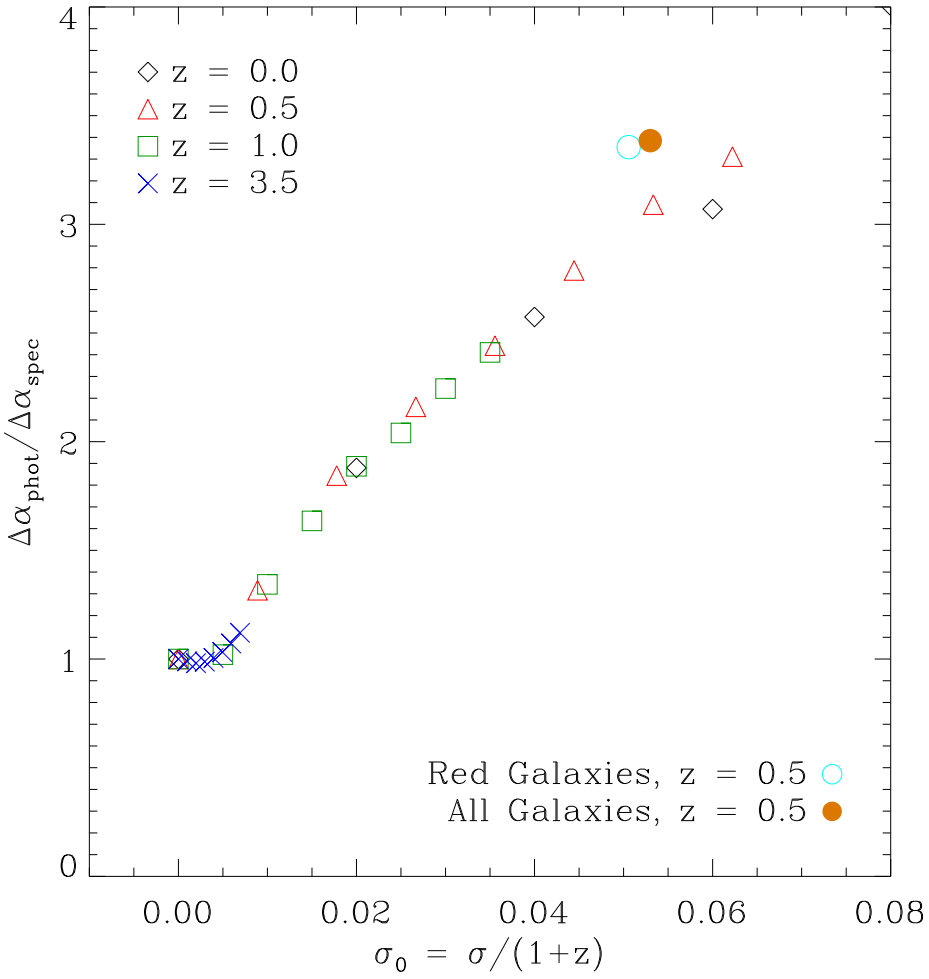


Figure 2.18: The ratio of the error on the measurement of the BAO scale in photo-$z$ space to that in redshift space (i.e. from a perfect spectroscopic redshift) as a function of the magnitude of the photometric redshift error. Assuming that the error on the measurement scales with the square root of the volume, then the $y$-axis gives the square root of the ratio of volumes of photometric to spectroscopic surveys which achieve the same accuracy in the measurement of the BAO scale. Note that this quantity is independent of the redshift at which the measurement is made, i.e. it is independent of the degree of nonlinearity present in the dark matter distribution. The cyan and brown circles give the results from using the actual distribution of photometric redshift errors, while the others assume a Gaussian error distribution shown in Fig. 2.16.

degradation.

These improvements lead to predictions that are somewhat different from previous ones. For example, for $\Delta z = 0.03$, Blake and Bridle (2005) predict a factor of $\sim$10 for the reduction of the effective volume of a photometric survey. Here, as shown in Fig. 2.18, we find a reduction which is a factor 2 times smaller than this (i.e. a volume reduction factor of $\sim$5). The main difference between our analyses is that Blake and Bridle (2005) use only modes larger than $k_{\rm max} = 2/\sigma_z$, arguing that wavelengths shorter than the size of the photometric redshift errors contribute only noise. In reality, there is a smooth transition around $k_{\rm max}$, with signal coming from all wavenumbers (with different weighting, of course). In addition, the neglect of nonlinear evolution (which erases the BAO at high wavenumbers) also contributes to Blake and Bridle (2005) overestimating the reduction in effective volume. These two effects together explain the disagreement between our results.

## 2.6 Discussion and conclusions

We have described a method for constructing mock galaxy catalogues which are well suited to aid in the preparation, and eventually in the interpretation of large photometric surveys. We applied our mock catalogues specifically to the data that will shortly begin to be collected with PS1, the first of the 4 telescopes planned for the Pan-STARRS system.

Our mock catalogue building method relies on the use of two complementary theoretical tools: cosmological N-body simulations and a semi-analytic model of galaxy formation. For this study, we have employed the Millennium N-body simulations of Springel et al. (2005) together with galaxy properties calculated using the GALFORM model with the physics described by Bower et al. (2006). Although this model gives quite a good match to the local galaxy luminosity function in the B- and K-band, we refined the match by applying a small correction of 0.15 mag to the luminosities of all galaxies, so that the agreement with the SDSS luminosity function is excellent. Similarly, we applied a correction to the predicted galaxy sizes as a function of redshift in order to match the SDSS distribution of Petrosian half-light radii in the $r$-band. As a simple test, we showed that our galaxy formation model agrees very well with the $r$-band number counts in the SDSS Commissioning and DEEP2 data over a range of 12 magnitudes.

We adopt a similar magnitude system as the SDSS, based on the use of Petrosian magnitudes and use these to calculate the expected magnitude limits for extended objects in the two surveys that PS1 will undertake, the "$3\pi$" survey and the MDS. We find that, after 3 years, the $3\pi$ survey will have detected $\sim 2 \times 10^8$ galaxies in all 5 photometric bands ($g, r, i, z$ and $y$), with a peak in the redshift distribution of $\sim$0.5 and an extended tail containing about 10 million galaxies with $z > 0.9$. The MDS will detect $\sim 2 \times 10^7$ galaxies, the redshift distribution peaking at $z \sim 0.8$, with 0.5 million galaxies lying at $z > 2$. Of the 5 PS1 bands $y$ is the shallowest and removing the requirement that a galaxy be detected in this band more than doubles the total numbers in the sample.

We have used our mock catalogues to take a first look at the accuracy of photometric redshifts in the PS1 photometric system. Photometric redshifts can be readily estimated using the public Hyper-$z$ code of Bolzonella et al. (2000). With the PS1 $grizy$ bands alone it is possible, in principle, to achieve an accuracy in the $3\pi$ survey of $\Delta z/(1+z) \sim 0.06$ in the range $0.25 < z < 0.8$. This could be reduced to $\sim$0.05 by adding $J$ and $K$ photometry from the UKIDSS (LAS) and could be improved even further with a hypothetical $U$ band survey to 23 mag, although the samples become progressively smaller as these additional bands are added. Cutting at the relatively shallow depth of the $y$-band is important in achieving these errors. Going deeper than the $y$-band data would increase the sample size substantially, but the errors would increase to $\sim$0.075. There is therefore a balance to be struck between reducing the sample size (by about a factor of 2) which increases the accuracy of all the photometry, allows the $y$-band to be used and has the combined effect of increasing the photometric redshift accuracy. For the MDS an accuracy of $\Delta z/(1+z) \sim 0.05$ is achievable for $0.02 < z < 1.5$ using the PS1 bands alone, with similar fractional improvements as for the $3\pi$ survey by the inclusion of $U$ and near infrared bands.

A dramatic improvement in photometric redshift accuracy can be achieved for samples containing only red galaxies. We have shown that it should be possible to identify a red sample (i.e. with red rest-frame $g - r$ colours) directly from the photometric data using the best-fit Hyper-$z$ templates. These samples can still contain large numbers of galaxies. For example, an accuracy of $\Delta z/(1+z) \sim 0.02 - 0.04$ may be achievable for $\sim$100 million red galaxies at $0.4 < z < 1.1$ in the $3\pi$ survey. Similarly, for the MDS, this sort of accuracy could be achieved for $\sim$30 million galaxies at $0.4 < z < 2$. These estimates are all based on the "off-the-shelf" Hyper-$z$

code, without any tuning of the code for the PS1 setup. We expect that further improvements should be possible by refining the photometric redshift estimator and tailoring it specifically to the PS1 bands.

Our analysis is based on the use of the GALFORM semi-analytic galaxy formation model. Although this model gives a good match to a large range of observed galaxy properties, it is based on a number of approximations and has uncertain elements which could be relevant to the estimation of photometric redshifts. These include the effects of reddening, assumptions about the frequency and duration of bursts and the use of the Bruzual and Charlot (1993) stellar population synthesis libraries which are the same as assumed in our implementation of Hyper-$z$. We note that the star formation histories predicted by the model are much more varied and have a richer structure than those assumed to construct the Hyper-$z$ templates, and that the treatment of dust extinction is very different in GALFORM. Abdalla et al. (2008) carried out a similar study to ours and reached similar conclusions about the size of the photometric redshift errors and the usefulness of additional filters in the NIR or far-UV. This is encouraging as Abdalla et al. used a completely different photometric redshift estimator, ANNz, an artificial neural network code written by Collister and Lahav (2004). Furthermore, instead of using a galaxy formation model to generate a mock catalogue, these authors used a mixture of empirical and theoretical techniques to produce a set of galaxies on which to test their estimator.

One of the main applications of the PS1 $3\pi$ survey will be to the determination of the scale of baryonic acoustic oscillations used to constrain the properties of the dark energy. We have investigated how uncertainties in the photometric redshifts will degrade the determination of the BAO scale and, in particular, we have quantified the factor by which the effective volume of a photometric survey is reduced by these uncertainties. We find that, with the sorts of photometric redshift uncertainties that we have estimated for a red sample, PS1 will achieve the same accuracy as a spectroscopic galaxy survey containing 1/5 as many galaxies (Assuming that the $N(z)$ is the same for the photo-$z$ survey and the spectroscopic survey, the photo-$z$ survey will gain more survey volume by covering a larger area.). Unfortunately, spectroscopy for 20 million galaxies at $z \sim 1$ is not likely to be feasible for some time. PS1 should be able to provide competitive estimates of the BAO scale in the next few years.

# Chapter 3

# *The ISW cross-correlation and its non-linear contribution*

## 3.1 Introduction

The Integrated Sachs-Wolfe (ISW) effect (Sachs and Wolfe, 1967), in which the decay of the large-scale potential fluctuations induces CMB temperature perturbations, provides a direct measure of the dynamical effect of dark energy. In principle, the ISW effect could be detected directly in the CMB power spectrum at very low multiples. In the ΛCDM cosmology, it would boost the plateau in the power spectrum at $l \sim 10$. However, as the increase of the power is not large in comparison to the cosmic variance, it cannot be unambiguously detected even in the WMAP data (Hinshaw et al., 2008). A more sensitive technique is to search for the ISW signal in the cross-correlation of the LSS with the CMB. As the expected signal is weak and occurs on large scales, a very large galaxy survey is needed to trace the LSS. Currently individual detections based on surveys such as APM, 2MASS, NVSS and SDSS (e.g. Fosalba et al., 2003; Afshordi et al., 2004; Fosalba and Gaztañaga, 2004; Padmanabhan et al., 2005; Cabré et al., 2006; McEwen et al., 2007; Rassat et al., 2007; Raccanelli et al., 2008) are not of very high statistical significance (but see Granett et al., 2008) and precise measurements await the construction of new, larger surveys (BOSS[1], Pan-STARRS1[2]). If such surveys are to place robust, meaningful constraints on the properties of the dark energy it is important to take full account of other processes beyond the (linear) ISW effect that may contribute to the cross-correlation signal. Here, we focus on deviations caused by non-linear gravitational

[1] http://www.sdss3.org/cosmology.php

[2] http://www.ps1sc.org/

evolution, the Rees-Sciama effect (Rees and Sciama, 1968).

Other processes are known to contribute to the cross-correlation signal. First, the thermal Sunyaev-Zel'dovich (SZ) effect (Sunyaev and Zeldovich, 1972) caused by hot ionized gas in galaxy clusters induces an anti-cross-correlation signal which can cancel the ISW effect on small scales. Its statistical contribution can be modelled and subtracted given the value of $\sigma_8$ (the *rms* linear mass fluctuations within a sphere of 8 $h^{-1}$ Mpc) which determines the abundance of galaxy clusters (e.g. White et al., 1993; Fan and Chiueh, 2001; Mei and Bartlett, 2004). Also, since the thermal SZ effect is frequency dependent, it can be subtracted in frequency space given sufficient spectral coverage. Second, the redshift dependence of galaxy bias, if not properly taken into account, can introduce systematic effects in the determination of dark energy parameters. Other effects such as lensing magnification and the Doppler redshift effect can also boost the cross-correlation signal, but are only important at high redshift (Loverde et al., 2007; Giannantonio and Crittenden, 2007). These effects are well documented and can be calibrated and removed.

In this chapter we will solely explore the contribution of the non-linear terms, or the Rees-Sciama (RS) effect, on the cross-correlation signal. The RS effect arises from the non-linear evolution of the potential (Rees and Sciama, 1968). It is believed to be much smaller than the CMB signal at all scales (Seljak, 1996; Puchades et al., 2006). Indeed, compared with the CMB power spectrum, the RS effect is orders of magnitude lower. Also, compared with the complete integrated ISW power spectrum, the RS effect has been shown, using the halo model approach (e.g. Cooray, 2002a,b), to be unimportant at $l < 100$. However, the RS effect has not been taken into account in cross-correlation analyses and it is important to assess its importance ahead of the completion of the next generation of large deep galaxy surveys.

We use a large N-body simulation to investigate the effect of the non-linear contribution on the interpretation of the ISW cross-correlation signal. We use the $488^3$-particle L-BASICC simulation described by Angulo et al. (2008) which, with a box size of 1340 $h^{-1}$ Mpc, is ideal for this purpose because not only does it enable us to extrapolate our analysis to non-linear scales at different redshifts, but it includes the very large scale power necessary to check the agreement with linear theory. The cosmology adopted in the L-BASICC simulation is ΛCDM, with $\Omega_\Lambda = 0.75$, $\Omega_\mathrm{m} = 0.25$, $\Omega_\mathrm{b} = 0.024$, $\sigma_8 = 0.9$ and $H_0 = 73$ km s$^{-1}$ Mpc$^{-1}$.

This chapter is organised as follows. In §3.2, we compute the power spectrum of

the ISW plus RS effects from our simulation and compare them with linear theory. In §3.3, we analyse these two effects in terms of the cross-correlation of the LSS with the CMB. Finally, in §3.3, we discuss our results and present our conclusions.

## 3.2 Time derivative of the potential

The integrated Sachs-Wolfe effect results from the late-time decay of gravitational potential fluctuations. The net induced ISW temperature fluctuation along a direction $\hat{n}$ can be written as an integral of the time derivative of the gravitational potential, $\dot{\Phi}$, from last scattering surface to the present (i.e. Sachs and Wolfe, 1967; Martinez-Gonzalez et al., 1990),

$$\Delta T(\hat{n}) = \frac{2}{c^2}\bar{T_0}\int_{t_{\rm L}}^{t_0} \dot{\Phi}(t,\hat{n})\, dt, \tag{3.1}$$

where $t$ is cosmic time, $t_{\rm L}$ is the age of the universe at the last scattering surface, $t_0$ the present age, $\dot{\Phi}$ is the time derivative of the gravitational potential, $\bar{T_0}$ is the mean CMB temperature and $c$ is the speed of light. This is equivalent to the integral over radial comoving distance, $r$,

$$\Delta T(\hat{n}) = \frac{2}{c^3}\bar{T_0}\int_{0}^{r_{\rm L}} \dot{\Phi}(r,\hat{n})\, a\, dr, \tag{3.2}$$

where $r_L$ is the comoving distance to the last scattering surface and $a$ the expansion factor. The net blueshift or redshift of the CMB photons caused by the change in the potential during the passage of the photons induces net temperature fluctuations of the black body spectrum, The angular power spectrum of these temperature fluctuations (see the Appendix) is given by

$$\begin{aligned} C_l = \frac{4}{c^6}\frac{2}{\pi}\int\int_0^{t_L}\int_0^{t_L} aa'k^2 P_{\dot{\Phi}\dot{\Phi}}(k,r,r') j_l(kr) j_l(kr') dt' dt dk \\ \approx \frac{4}{c^5}\int_0^{t_L} a P_{\dot{\Phi}\dot{\Phi}}(k=\frac{l}{r},t)/r^2\, dt, \end{aligned} \tag{3.3}$$

where $r$ is the comoving distance to lookback time, $t$, $j_l$ is the spherical Bessel function and $P_{\dot{\Phi}\dot{\Phi}}(k,r)$ is the 3-D power spectrum of $\dot{\Phi}$ fluctuations. To derive the final expression we have used Limber's approximation by assuming $k \approx l/r$ (Limber, 1954; Kaiser, 1992; Hu, 2000; Verde et al., 2000, also see the Appendix).

The ISW effect consists of the temperature fluctuations described by these equations when linear theory is used to compute $\dot{\Phi}$ and its fluctuation power spectrum $P_{\dot{\Phi}\dot{\Phi}}$. Using a simulation to determine the non-linear contributions we can quantify

the full ISW plus Rees-Sciama effect. In Fourier space, the time derivative of the gravitational potential can be expressed as:

$$\dot{\Phi}(\vec{k},t) = \frac{3}{2}\left(\frac{H_0}{k}\right)^2 \Omega_{\rm m}\left[\frac{\dot{a}}{a^2}\delta(\vec{k},t) - \frac{\dot{\delta}(\vec{k},t)}{a}\right], \tag{3.4}$$

where $a$ is the expansion factor, $H_0$ is the Hubble constant, $\Omega_{\rm m}$ is the present mass density parameter and $\dot{\delta}$ is the time derivative of the density fluctuation. Combining this with the Fourier space form of the continuity equation, $\dot{\delta}(k,t) + i\vec{k}\cdot\vec{p}(\vec{k},t) = 0$ gives:

$$\dot{\Phi}(\vec{k},t) = \frac{3}{2}\left(\frac{H_0}{k}\right)^2 \Omega_{\rm m}\left[\frac{\dot{a}}{a^2}\delta(\vec{k},t) + \frac{i\vec{k}\cdot\vec{p}(\vec{k},t)}{a}\right], \tag{3.5}$$

where $\vec{p}(\vec{k},t)$ is the Fourier transform of the momentum density divided by the mean mass density, $\vec{p}(\vec{x},t) = [1+\delta(\vec{x},t)]\vec{v}(\vec{x},t)$. This enables us to estimate the Fourier transform of the $\dot{\Phi}$ field of the simulation from the Fourier transforms of the density and momentum fields. Using equation (3.4), the resulting power spectrum, $P_{\dot{\Phi}\dot{\Phi}}(k,t) = (2\pi)^{-3}\langle\dot{\Phi}(k,t)\dot{\Phi}^*(k,t)\rangle$, can be written as

$$\begin{aligned} P_{\dot{\Phi}\dot{\Phi}}(k,t) &= \frac{9}{4}\left(\frac{H_0}{k}\right)^4 \Omega_{\rm m}^2 \times \\ &\left[\left(\frac{\dot{a}}{a^2}\right)^2 P_{\delta\delta}(k,t) - 2\frac{\dot{a}}{a^3}P_{\delta\dot{\delta}}(k,t) + \frac{1}{a^2}P_{\dot{\delta}\dot{\delta}}(k,t)\right]. \end{aligned} \tag{3.6}$$

In linear theory, $P_{\dot{\delta}\dot{\delta}}(k,t) = k^2 P_{vv}(k,t) = \dot{D}(t)^2 P^{\rm lin}_{\delta\delta}(k)$ and $P_{\delta\dot{\delta}}(k,t) = kP_{\delta v}(k,t) = D(t)\dot{D}(t)P^{\rm lin}_{\delta\delta}(k)$, where $P^{\rm lin}_{\delta\delta}(k)$ is the linear density power spectrum at the present time and $D(t)$ is the growth factor normalised to be unity at present. Therefore, the power spectrum of the linear ISW effect is

$$P^{\rm lin}_{\dot{\Phi}\dot{\Phi}}(k,t) = \frac{9}{4}\left(\frac{H_0}{k}\right)^4 \Omega_{\rm m}^2\left[\frac{H(t)D(t)(1-\beta)}{a}\right]^2 P^{\rm lin}_{\delta\delta}(k), \tag{3.7}$$

where $\beta = \frac{{\rm d}\ln D}{{\rm d}\ln a} \simeq \Omega_{\rm m}^{0.6}(t)$. For easy comparison at different redshifts in the simulation, we defined a scaled $\dot{\Phi}$ power spectrum, $\mathcal{P}_{\dot{\Phi}\dot{\Phi}} = P_{\dot{\Phi}\dot{\Phi}}/[\frac{9}{4}\left(\frac{H_0}{k}\right)^4\Omega_{\rm m}^2]$ which from Eq. (3.6) is simply

$$\mathcal{P}_{\dot{\Phi}\dot{\Phi}}(k,z) \equiv P_{\delta\delta}(k,z) - 2\frac{P_{\delta\dot{\delta}}(k,z)}{H(z)} + \frac{P_{\dot{\delta}\dot{\delta}}(k,z)}{H^2(z)}. \tag{3.8}$$

Our measurements of the $\mathcal{P}_{\dot{\Phi}\dot{\Phi}}(k,z)$ power spectrum are shown in Fig. 3.1. The results from linear theory are also plotted. We find the total scaled $\dot{\Phi}$ power spectrum can be well fitted by a broken power law plus the linear scaled $\dot{\Phi}$ power spectrum $\mathcal{P}_{\dot{\Phi}\dot{\Phi}} = \mathcal{P}^{\rm nonlin}_{\dot{\Phi}\dot{\Phi}} + \mathcal{P}^{\rm lin}_{\dot{\Phi}\dot{\Phi}}$, where

$$\mathcal{P}^{\rm nonlin}_{\dot{\Phi}\dot{\Phi}}(k,z) = \frac{A}{(10k)^{-4/0.75} + (10k)^{-4/B}}. \tag{3.9}$$

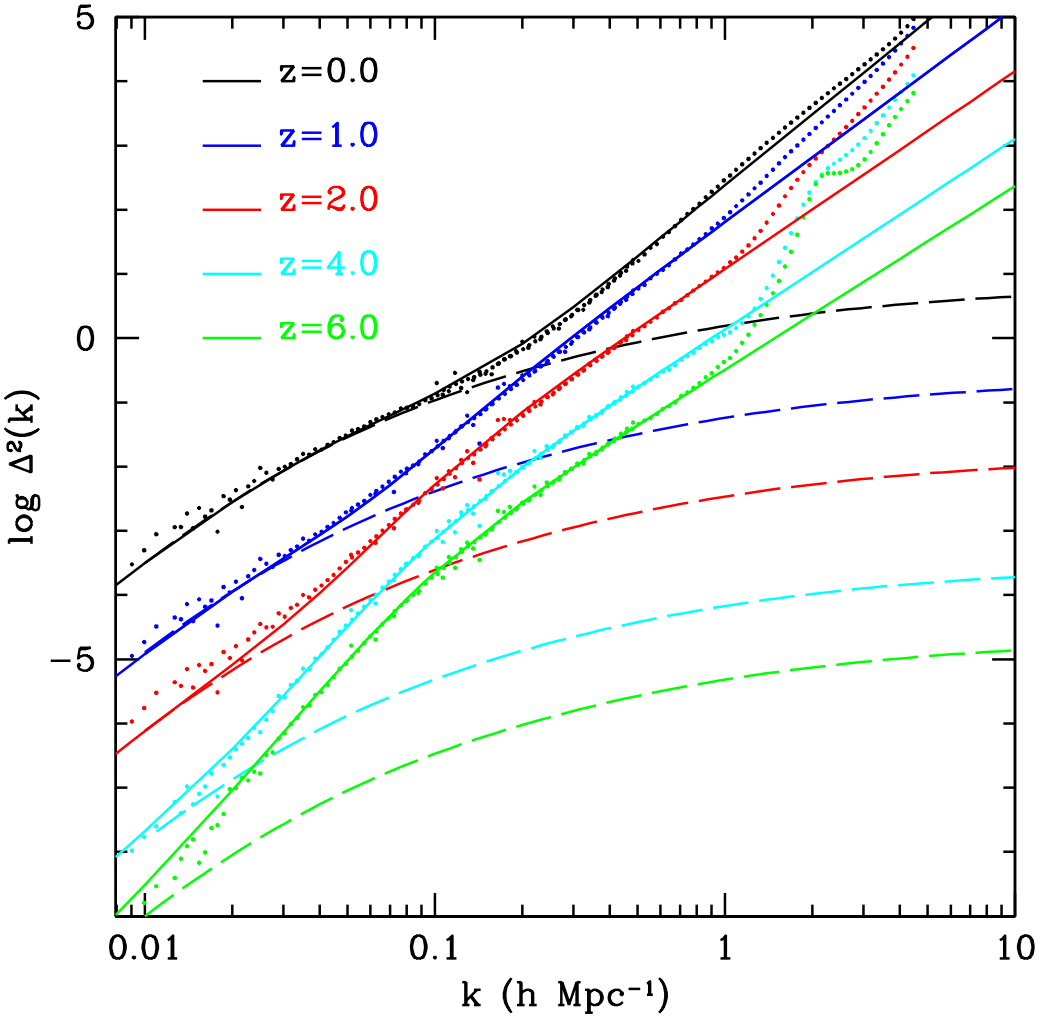


Figure 3.1: Scaled $\dot{\Phi}$ power spectrum, $\mathcal{P}_{\dot{\Phi}\dot{\Phi}}(k)$, at different redshifts, $\Delta^2(k) \equiv k^3\mathcal{P}_{\dot{\Phi}\dot{\Phi}}(k)/2\pi^2$. The dotted lines are the measurements from the L-BASICC simulation. The solid lines are our model, while the dashed lines are the linear theory. The deviation of the simulation results from linear theory happens at larger scales as redshift increases. We also find that the deviation from linear theory for the $\dot{\Phi}$ field occurs at larger scales than that of the density field at all redshifts.

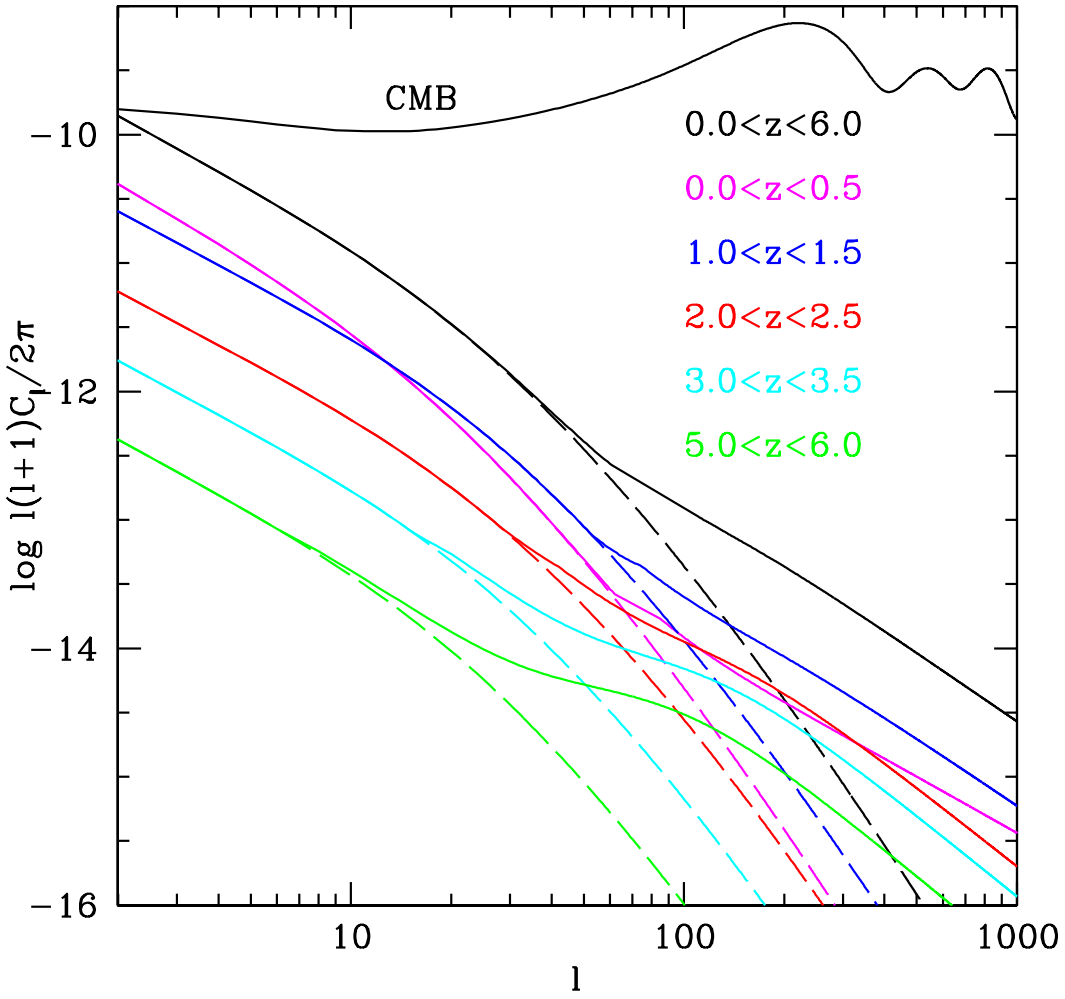


Figure 3.2: ISW angular power spectrum coming from different redshift intervals, where $l(l+1)C_l/2\pi = (\Delta T/T)^2$. The solid lines are given by Eq. (3.3) and Eq. (3.6), evaluated using our model of the measurements from the L-BASICC simulation. The dashed lines are linear theory. The power spectrum at $0 < z < 6$ shows that the deviation of the simulation results from linear theory starts at $l < 100$. The deviation starts at smaller $l$ as redshift increases.

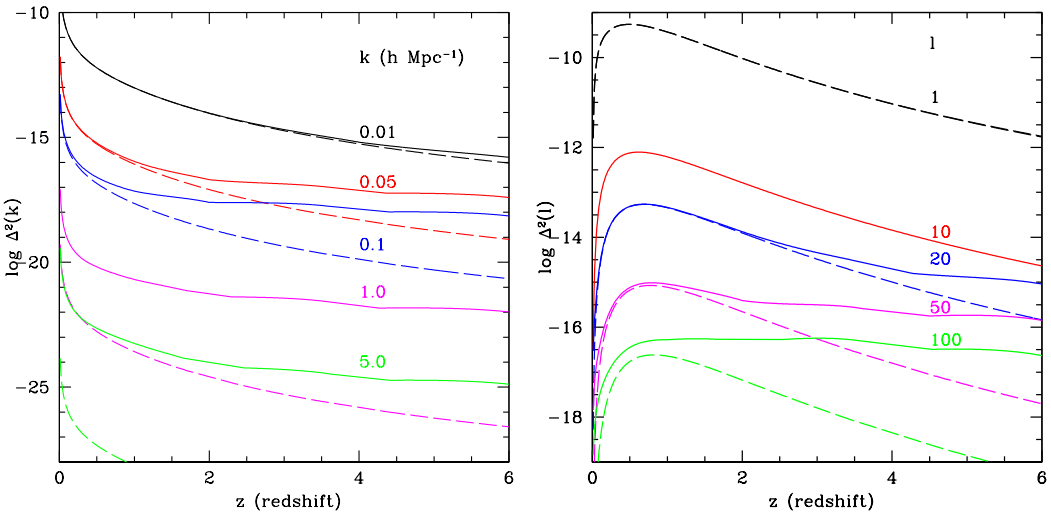


Figure 3.3: Evolution of the $\dot{\Phi}$ power spectrum $\Delta^2(k) \equiv k^3 \mathcal{P}_{\dot{\Phi}\dot{\Phi}}(k)/2\pi^2$ for specific spatial (left) and angular (right) modes. The solid lines show our model of the simulation results. The dashed lines show the results of linear theory. The power $\Delta^2(k)$ decreases monotonically as a function of $z$ at all scales in linear theory. However, the total power seems to be independent of $z$ at high redshift. The deviation from linear theory increases with $z$ and $k$. The angular power spectrum $\Delta^2(l)$ shows no deviation from linear theory up to $l = 10$. For $l > 50$, deviations appear at all redshifts.

Here A and B are two free parameters that we use to fit the model to the simulation results at each redshift up to $z = 6$. To interpolate the model to intermediate redshifts we linearly interpolate the values of A and B from the nearest two simulation outputs. Our model is compared to the simulation results in Fig. 3.1.

We see in Fig. 3.1 that the linear theory reproduces the ISW+RS $\mathcal{P}_{\dot{\Phi}\dot{\Phi}}$ at $z = 0$ only at $k < 0.1$ $h$ Mpc$^{-1}$. It fails at progressively larger scales as the redshift increases. By $z = 2$, linear theory agrees with the simulation results only at $k < 0.02$ $h$ Mpc$^{-1}$. The reason for this surprising behaviour is that the linear part of the $\mathcal{P}_{\dot{\Phi}\dot{\Phi}}$ drops quickly to zero as the relative importance of $\Omega_\Lambda$ diminishes at high redshift, while the non-linear part evolves more slowly with redshift. Therefore, the deviation of the total power spectrum from linear theory happens at larger scales at higher redshifts. We find that the momentum power spectrum, $P_{\dot{\delta}\dot{\delta}}$, and the correlation power spectrum of the density and momentum, $P_{\delta\dot{\delta}}$, behave similarly to the $P_{\dot{\Phi}\dot{\Phi}}$

power spectrum, namely, their deviation from linear theory occurs at larger scales at higher redshift. This is in contrast with the power spectrum of the density field which deviates from linear theory on progressively larger scales at lower and lower redshift. In another words, at the same redshift, the deviation from linear theory occurs at smaller scales for the density field than for the other fields.

The sharp increase of $\mathcal{P}_{\dot{\Phi}\dot{\Phi}}$ measured from the simulation at small scales ($k > 1$ $h$ Mpc$^{-1}$) is due to discreteness in the $448^3$ particle L-BASICC simulation. We used the much higher resolution $2160^3$ particle Millennium simulation (Springel et al., 2005) to verify that our model remains accurate at smaller scales and is robust to shot noise corrections.

We can now compute the induced angular power spectrum of CMB temperature fluctuations by performing the integral in equation (2) over the redshift range $0 < z < 6$ using our model for the 3-D power spectrum, $P_{\dot{\Phi}\dot{\Phi}}(k, z)$. The overall result is shown in Fig. 3.2 along with the contributions coming from different redshift intervals. For the overall angular power spectrum the deviation of the model from the linear theory happens at $l \sim$100. This result confirms the prediction of Cooray (2002b) based on the halo model. However, we also see that the failure of linear theory, as judged by our simulation results, occurs at smaller and smaller $l$ as redshift increases. For example, above $z = 5$, the deviation occurs at $l < 20$ and, for larger values of $l$ than this, linear theory becomes extremely inaccurate.

In order to evaluate how the breakdown of linear theory depends on redshift, we plot the evolution of the $\dot{\Phi}$ power at a given scale as a function of redshift in Fig. 3.3. Generally, the deviations of linear theory from the simulation results decrease with scale and increase with redshift. At $k = 0.01$ $h$ Mpc$^{-1}$, deviations start to be seen at $z \sim 3$ and, at $k = 0.1$ $h$ Mpc$^{-1}$, linear theory has become inaccurate at all redshifts. In the right-hand panel, which shows results in $l$ space, we find no deviations up to $l \sim 10$, but for $l > 50$, linear theory has clearly broken down at all redshifts. Interestingly, at high redshift, the $\dot{\Phi}$ power in the simulation appears to be independent of $z$ while, in linear theory, this quantity drops monotonically with $z$.

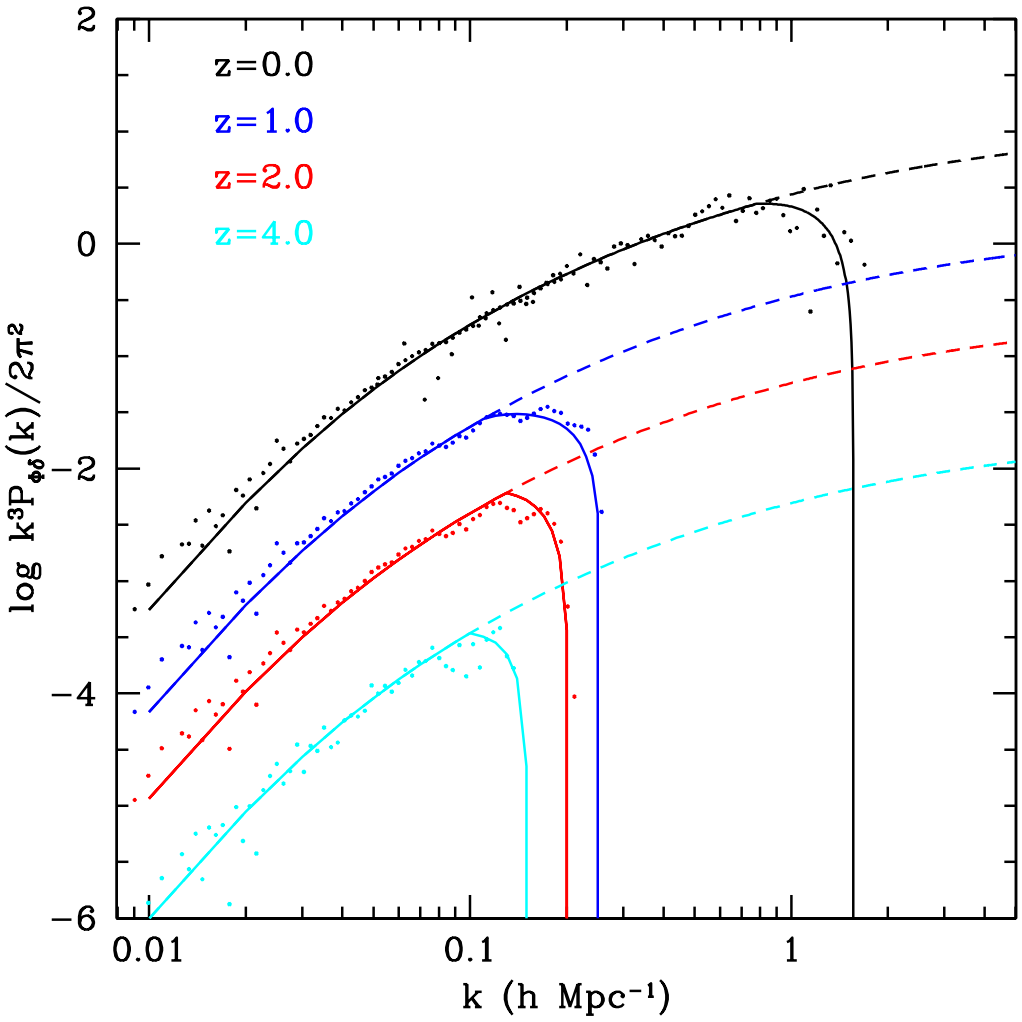


Figure 3.4: The cross power spectrum of $\dot{\Phi}$ with $\delta$ at different redshifts. The dotted lines represent the measurements from the L-BASICC and the dashed lines linear theory. The solid lines are our model fit to the sum of the linear theory and the non-linear contribution in the L-BASICC simulation. The non-linear effect begins to appear at $k \sim 1\ h\ \mathrm{Mpc}^{-1}$ at $z = 0$, and at larger scales at higher redshifts. It rapidly suppresses the cross power spectrum and causes it to become negative on small scales.

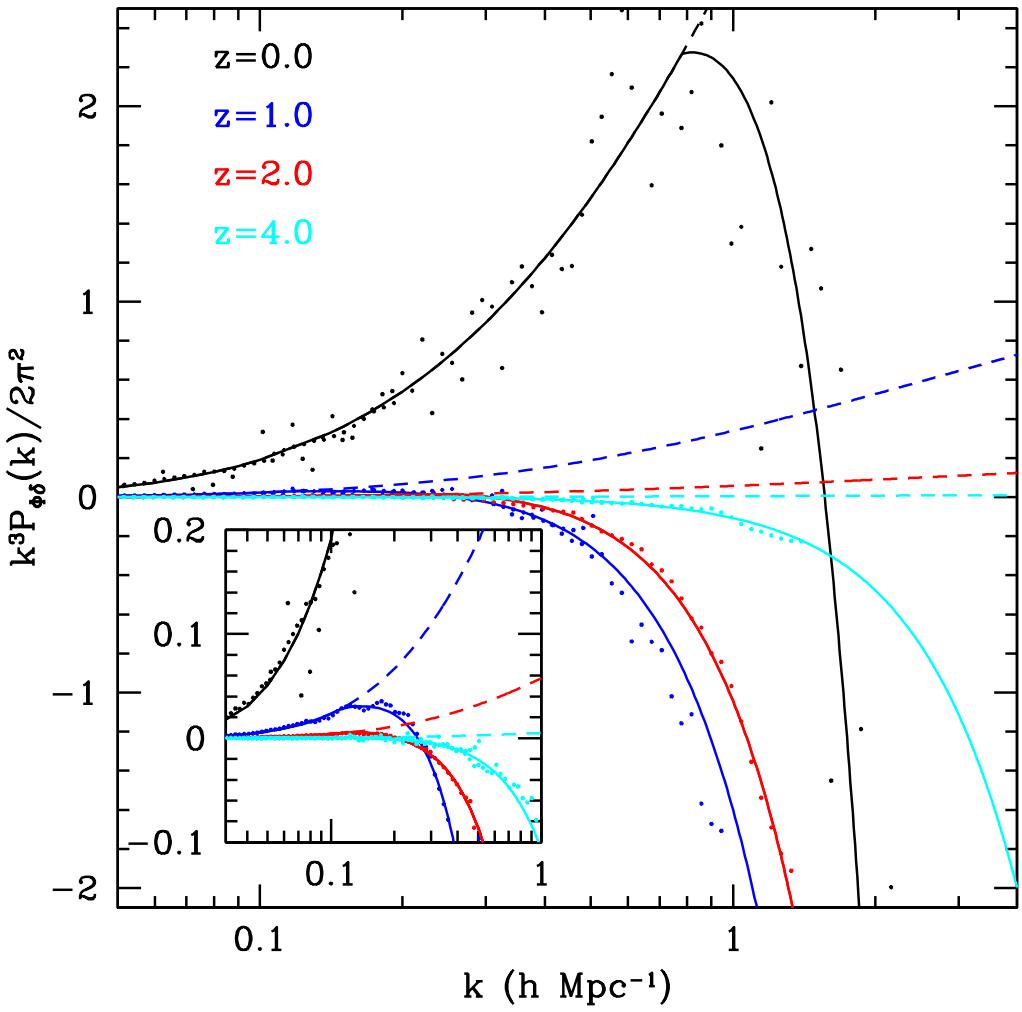


Figure 3.5: The same as in Figure (3.4) but on a linear scale.

## 3.3 The LSS-CMB cross-correlation

To illustrate the contribution of the Rees-Sciama effect to the cross-correlation of the density field $\delta$ with $\dot{\Phi}$, we can compute the 3-D cross-correlation power spectrum $P_{\dot{\Phi}\delta}(k,z) =< \dot{\Phi}(\vec{k},z)\delta^*(\vec{k},z) >$ from our simulations:

$$\mathcal{P}_{\dot{\Phi}\delta}(k,z) = P_{\delta\delta}(k,z) - \frac{P_{\dot{\delta}\delta}(k,z)}{H(z)} \tag{3.10}$$

In linear theory, $\mathcal{P}_{\dot{\Phi}\delta}(k,z) = D^2(1-\beta)P^{\rm lin}_{\delta\delta}(k)$, where $P^{\rm lin}_{\delta\delta}(k)$ is the linear density power spectrum at the present time. Results from our simulations are shown in Fig. 3.4 and Fig. 3.5. Comparing with linear theory, we find that the non-linear contribution appears at somewhat smaller scales than that of the autocorrelation power spectrum of $\dot{\Phi}$. At $z = 0$, the deviation occurs at $k \sim 1\ h\ {\rm Mpc}^{-1}$. However, it then dominates rapidly, making the cross-correlation power spectrum negative. This indicates that once the non-linear effect dominates, the potential of overdense regions evolves faster than the expansion of the universe, becoming deeper and thus imparting a net redshift to CMB photons passing through them. This induces a negative cross-correlation between the CMB and the LSS. To quantify the effect on the large-scale ISW cross-correlation measurements, we model the 3-D cross power spectrum from the simulations at each redshift output. We use linear theory to model the linear regime but once the cross power spectrum starts to deviate from linear theory, we fit it with a function of the form $k^3P_{\dot{\Phi}\delta}(k) = A_1 + A_2k + A_3k^2$, where $A_1, A_2$ and $A_3$ are free parameters. Interpolating to intermediate redshifts, we are then able to calculate the projected 2-D power spectrum.

The cross-correlation between LSS and CMB maps has been shown to be a powerful tool for verifying the existence of dark energy and constraining its properties. Current measurements of the cross-correlation have low statistical significance because the volumes probed by LSS surveys are relatively small, but this situation will improve greatly with upcoming surveys. For example, Pan-STARRS1 will survey three quarters of the sky, obtaining photometry for galaxies up to $\sim 24.6$ mag in the $g$-band. The mean galaxy redshift in this "$3\pi$ survey" will be $\bar{z} \sim 0.5$. Pan-STARRS1 will also carry out a deeper but smaller "MDS" survey covering 84 sq deg of the sky to $\sim 27.3$ mag in $g$ for which $\bar{z} \sim 0.8$ (Cai et al., 2009a). Cross-correlating such photometric redshift galaxy samples with a CMB map (from WMAP or Planck) will make it possible for the first time to perform ISW tomography. Galaxy samples would be divided into different redshift slices and each one cross-correlated with the

CMB map. Values of the dark energy equation of state parameter, $w$, could then be measured using the results from the different redshift slices, effectively constraining the evolution of $w$.

To illustrate how ISW tomography may work, we follow Baugh and Efstathiou (1993) and model the redshift distribution of galaxies tracing the LSS as

$$N(z) \propto \begin{cases} (z - z_c)^2 \exp\left[-(\frac{z-z_c}{z_0})^{3/2}\right] & \text{if } z \leq z_c \\ 0 & \text{if } z > z_c, \end{cases} \tag{3.11}$$

but then choose the parameters $z_0$ and $z_c$ to emulate plausible photometric redshift slices. (The same functional form was also taken by Cabré et al. (2006) to model the SDSS LRG sample.) We assume $z_0 = 0.2$ so that the width of $N(z)$ is much greater than the expected photometric redshift errors. We shift the function into different redshift intervals by using $z_c = 0, 1, 2$ and 3. The median redshift of these samples is $\bar{z} \approx 1.4z_0 + z_c = 0.28, 1.28, 2.28$ and 3.28 respectively. The cross-correlation power spectrum (derived in an analogous way to the auto-correlation function detailed in the appendix) is given as:

$$C_l^{\dot{\Phi}-g} \approx \frac{2}{c^2} \int_0^{z_L} P_{\dot{\Phi}\delta}(k = \frac{l}{r}, z) b(z) N(z) H(z)/r^2 dz, \tag{3.12}$$

where $P_{\dot{\Phi}\delta}(k, z)$ is the cross power spectrum of the potential field and the galaxy density field, $b(z)$ is the galaxy bias parameter at redshift $z$, and $N(z)$ is the normalised galaxy selection function, where $\int N(z)dz = 1$. We adopt the small-angle approximation in which $k = l/r(z)$, where $r(z)$ is the comoving distance. For simplicity, in this illustration, we assume the galaxy bias parameter to be unity. In angular space, the cross-correlation becomes:

$$w^{\dot{\Phi}-g}(\theta) = \sum_l \frac{2l+1}{4\pi} P_l(\cos\theta) C_l^{\dot{\Phi}-g}, \tag{3.13}$$

where $P_l$ are Legendre polynomials. In actual measurements of CMB fluctuations, the monopole and dipole are subtracted. Therefore, we set the power at $l = 0$ and $l = 1$ to zero before converting the signal into real space. To ensure that the results at smaller angles ($\theta < 1^\circ$) converge accurately, we sum the power up to $l = 10\,000$.

The cross-correlation results are shown in Fig. 3.6 and Fig. 3.7. The contribution from the non-linear RS effect can be seen to become increasingly important as the redshift of the sample increases. The cross-correlation power spectrum decreases and deviates from linear theory rapidly at $l \sim 500$ due to the non-linear effect. It

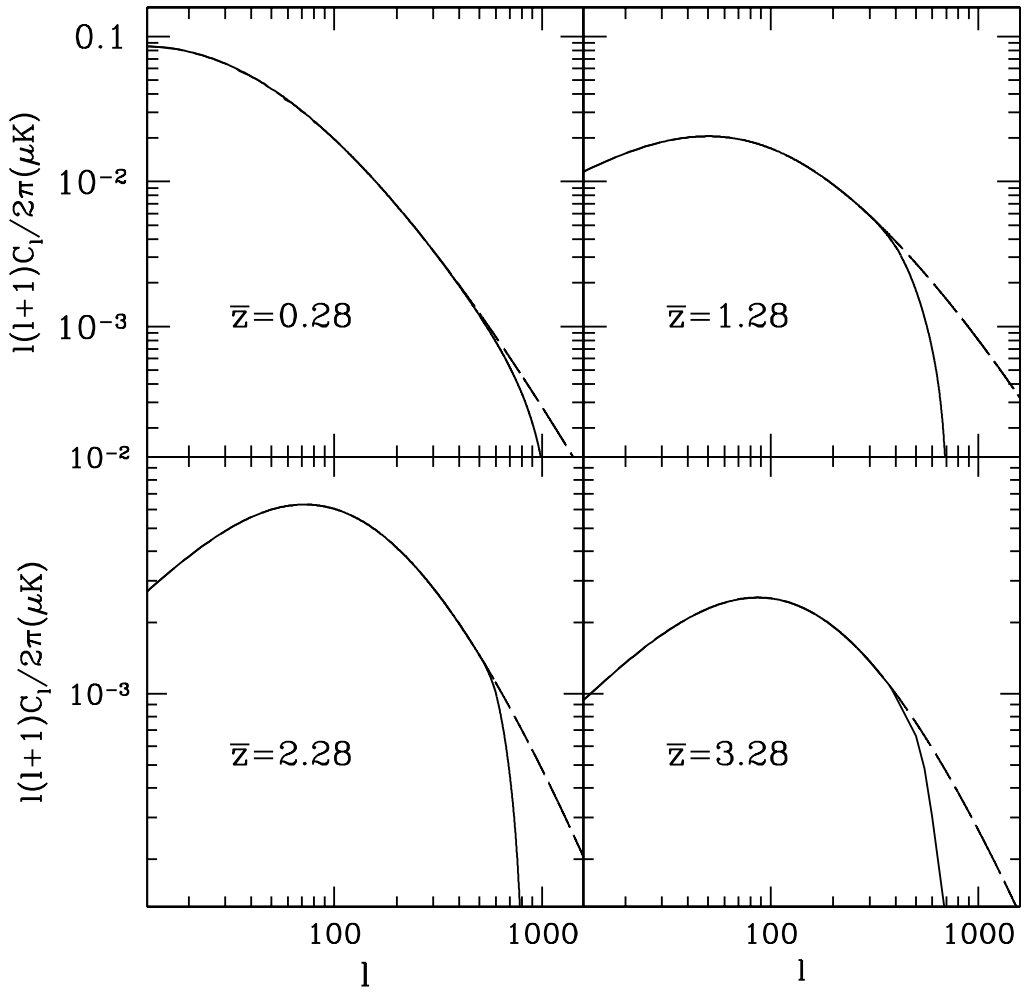


Figure 3.6: The cross-correlation power spectrum of galaxy samples at different $\bar{z}$ with the CMB. The dashed lines are given by linear theory. The solid lines are the sum of the linear theory and the non-linear contribution, which is given by our model fitted to the L-BASICC simulation. The non-linear effect begins to appear at $l \sim 500$. It rapidly makes the cross power spectrum become negative.

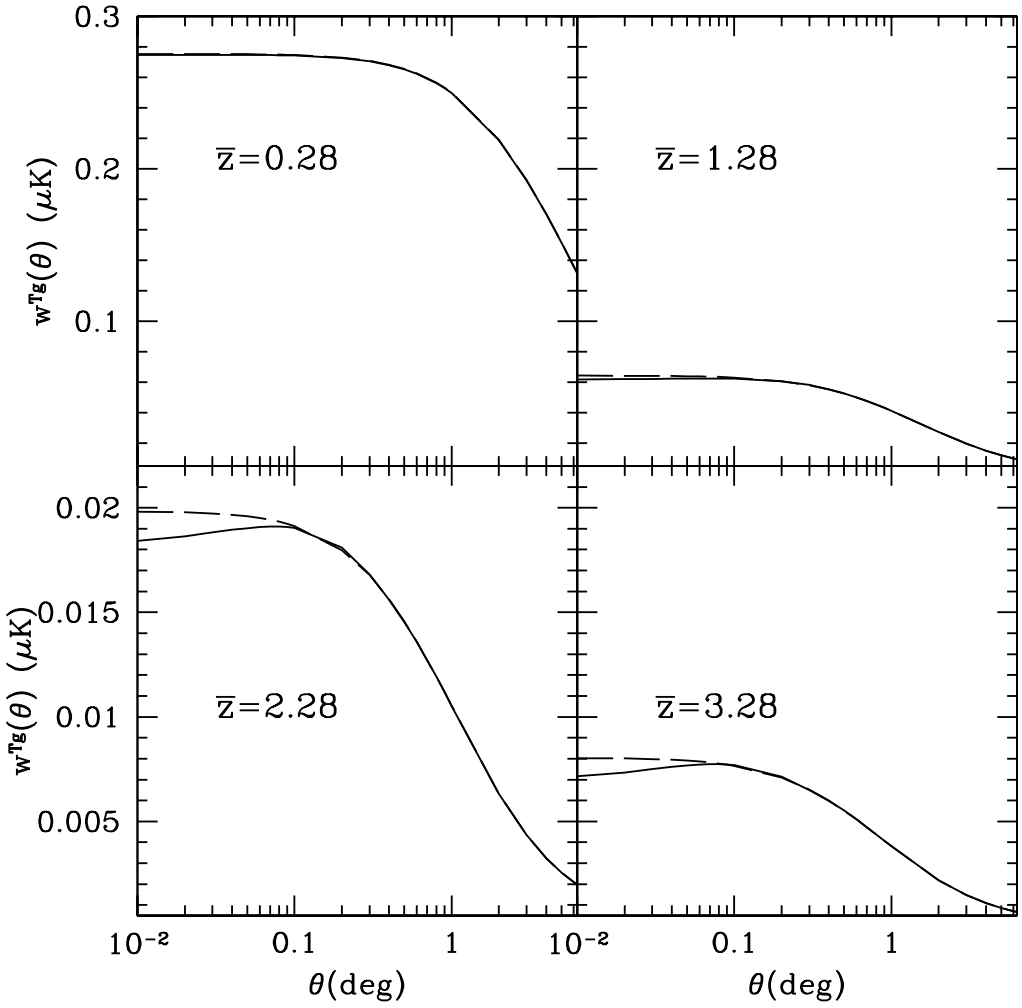


Figure 3.7: The cross-correlation of galaxy samples at different $\bar{z}$ with the CMB in angular space. The non-linear effect suppresses the ISW effect at sub-degree scales. It is negligible at low redshifts and large scales.

turns negative at $l \sim 1000$. This result is consistent with that obtained by Nishizawa et al. (2008) who used a similar method to illustrate the impact of the ISW and RS effects on the CMB-weak lensing cross-correlation. In angular coordinates, shown on the right-hand panel, the RS effect is negligible at $\theta > 1^\circ$ at all redshifts. For the high redshift samples, it becomes important at sub-degree scales for the high redshift samples where it suppresses the cross-correlation power spectrum by about $5 - 10\%$ at acrminute scales.

The statistical significance of current measurements of the CMB-LSS cross-correlation is not yet high enough to detect the effects we are discussing. Most current measurements can only determine the cross-correlation at degree scales or above (e.g. Cabré et al., 2006). Future CMB or SZ surveys with high resolution might be able to resolve this contribution.

## 3.4 Conclusions

We have used an N-body simulation to calculate the non-linear (Rees-Sciama) contribution to the Integrated Sachs Wolfe effect. The comparison of the 3-D and 2-D power spectra measured from the simulation with those given by linear theory reveals a strong nonlinear contribution whose physical scale increase with redshift. We investigated the strength of this effect on the cross-correlation of the CMB with galaxy samples in terms of angular power spectra and in angular coordinates at different redshifts. We find that there is a non-linear contribution to the cross-correlation signal at sub-degree scales. The non-linear effect alters not only the amplitude, but also the shape of the cross-correlation power spectrum. With current galaxy samples which cover relatively small volumes, it is not yet possible to disentangle the contribution of the RS effect from that of the ISW effect within the noise. However, in future surveys like Pan-STARRS and LSST, for which the number of galaxies and the sky coverage will increase dramatically, the error bars on the cross-correlation will be much smaller. In this case, the importance of the Rees-Sciama effect may become significant for high redshift samples. The effect of the non-linear cross-correlation at scales of arcminutes would contaminate the SZ signal in the CMB and this could confuse its interpretation (e.g. Fosalba et al., 2003; Diego et al., 2003; Myers et al., 2004; Lieu et al., 2006; Cao et al., 2006; Bielby and Shanks, 2007).

Our analysis is based on a simulation that assumes a ΛCDM cosmology. The

non-linear contribution depends on the values of the cosmological parameters. In a flat universe with a cosmological constant, the RS effect will become increasingly dominant relative to the ISW effect as the value of $\Omega_\Lambda$ decreases. In the most extreme case, if $\Omega_\Lambda = 0.0$, the ISW effect will vanish, leaving only the RS effect (Seljak, 1996). The analysis of this chapter could be generalized either using renormalised perturbation theory (e.g. Crocce and Scoccimarro, 2006), or simulations with different dark energy models. In any case, more general modelling of the non-linear effect will be required for an accurate interpretation of future measurements of the LSS-CMB cross-correlation.

# Chapter 4

# *Full-sky map of the ISW and Rees-Sciama effect from Gpc simulations*

## 4.1 Introduction

The Integrated Sachs-Wolfe (ISW) effect (Sachs and Wolfe, 1967) arises from the decay of the large-scale potential fluctuations as they are traversed by Cosmic Microwave Background (CMB) photons and induces secondary temperature perturbations in the CMB radiation. It occurs in both open models ($\Omega_{\rm m} < 1$) and models containing a cosmological constant ($\Omega_\Lambda > 0$) or dark energy. It has been shown to be an independent way of measuring the dynamical effect of such dark energy, but it is challenging to detect: At large scales, the ISW signal suffers from cosmic variance, as there are too few independent modes, while at somewhat smaller scales, it is entangled with the Rees-Sciama (RS) effect (Rees and Sciama, 1968), which arises from the non-linear evolution of gravitational potential perturbations. Since it is impossible to evade the cosmic variance at large scales, the information at small scales becomes valuable. Hence, to extract cosmological information from such scales, one needs to disentangle the ISW and RS effects.

Studies using N-body simulations have found that the combined ISW plus RS power spectra deviate from linear theory (ISW) at very large scales, $k \sim 0.1\ h\ {\rm Mpc}^{-1}$ at $z = 0$, with the scale of this transition becoming even larger at higher redshift. This discovery that the non-linear effect was more important at higher redshift was first made by Cai et al. (2009b) and later confirmed by Smith et al. (2009). Recent studies using both perturbation theory and semi-analytical fitting formulae indicate that the

combined ISW and RS effect has a non-trivial contribution to the overall CMB non-Gaussianity as measured by the bispectrum (e.g. Verde and Spergel, 2002; Giovi et al., 2003; Boubekeur et al., 2009; Mangilli and Verde, 2009), and the primordial-lensing-RS correlation contribution may yield an effective non-Gaussianity parameter $f_{\rm NL}$ of 10 (Mangilli and Verde, 2009). All these results suggest that the RS effect is a very important supplement to the ISW effect even at very large scales.

Observational evidence for a possible contribution from the RS effect at large scales comes from the combined study of the SDSS LRG samples and the CMB (Granett et al., 2009). These authors report a 4-$\sigma$ detection of the ISW and RS signal at the scale of 4 degrees, somewhat higher than expected from the concordance flat $\Lambda$CDM universe. There are also attempts to attribute the extreme CMB cold spot to the ISW and RS effects (e.g. Martinez-Gonzalez and Sanz, 1990; Martinez-Gonzalez et al., 1990; Rudnick et al., 2007; Inoue and Silk, 2006, 2007; Tomita and Inoue, 2008; Masina and Notari, 2009b,a). However on theoretical grounds such an explanation seems unlikely as the estimated sizes of the non-linear structures responsible for the cold spot are typically $>$ 100 Mpc, which is too large to occur in a $\Lambda$CDM universe with Gaussian initial conditions (See also Cruz et al., 2005; McEwen et al., 2005; Cruz et al., 2006; McEwen et al., 2006; Cruz et al., 2007; McEwen et al., 2008, for discussion of non-Gaussianity.). Hence it is still unclear whether or not the combined ISW and RS effects can generate cold spots of a few degrees with the right amplitudes and whether such large-scale non-Gaussianity can arise from large-scale structure. Therefore, a full understanding the ISW and Rees-Sciama effect is crucial in understanding the oddities of these observations. Meanwhile, the increase in sensitivity of the forthcoming CMB experiments opens possibilities of exploiting CMB temperature fluctuations down to arcmin scales (Planck[1], ACT[2], SPT[3] and APEX-SZ[4]), at which the ISW and RS effect may also entangle with other large-scale astrophysics of interest, i.e. lensing (e.g. Verde and Spergel, 2002; Nishizawa et al., 2008; Mangilli and Verde, 2009) and the Sunyaev-Zel'dovich (SZ) effect (Sunyaev and Zeldovich, 1972) (e.g. Cooray, 2002a; Fosalba et al., 2003; Bielby et al., 2009). To disentangle all these effects is the key to thoroughly exploiting the information encoded in these upcoming CMB measurements.

[1] www.sciops.esa.int/PLANCK/

[2] http://www.physics.princeton.edu/act/

[3] http://pole.uchicago.edu/

[4] http://bolo.berkeley.edu/apexsz

N-body simulations are the ideal tool for investigating the phenomena discussed above as they deal accurately with the non-linear regime. In particular, a full sky map of the ISW and RS effects together with the full underlying 3-dimensional lightcone will give a direct handle on their observable effects. Maps of the ISW effect have been constructed from both simulations and observations (Barreiro et al., 2008; Granett et al., 2009). Yet most of them simply adopt the linear approximation, using only the density field to estimate the time derivative of the potential. We will show in this chapter that these linear maps are far from accurate. There are also maps constructed from ray-tracing through simulations (Tuluie and Laguna, 1995; Puchades et al., 2006), but they are limited by their small simulation box sizes and therefore are not sufficient to explore very large-scale structures. A full sky map of the RS effect has been constructed using a constrained high-resolution hydrodynamical simulation to understand the RS effect in the very local universe (Maturi et al., 2007a). Their map is useful for understanding the RS effect from within the radial distance of 110 Mpc, which is a very small volume. Maps from the ray-tracing of large cosmological volumes are still missing.

In this chapter, we develop a new method of constructing a full sky lightcone of the time derivative of the potential, $\dot{\Phi}$, using a large N-body simulation. Our method of computing $\dot{\Phi}$ is fully non-linear and so should model the complete RS effect as well as the ISW component. Our Gpc box size simulation provides sufficient number of independent large scale modes to fully investigate the ISW effect. We ray-trace through the lightcone to produce maps of temperature fluctuations induced by the ISW and RS effects. Our maps are the first to cover a large range of scales and cosmic time with high accuracy. In this chapter, we use these maps to investigate the ISW and RS effects. The maps will also be a valuable resource for understanding CMB secondary non-Gaussianity arising from large-scale structure. They may also prove useful for disentangling lensing and SZ effects from the ISW and RS effects.

The chapter is organized as follows. In §4.2, we present the basic physics and the mathematical description of the ISW and RS effects. In §4.3, we describe our method of computing CMB temperature perturbations from our N-body simulation and ray-tracing to produce full sky maps from lightcone data. In §4.4 we identify and discuss three characteristic non-linear features of the temperature perturbations. Full sky maps are presented in §4.5. Finally, in §4.6, we discuss our results and draw conclusions.

## 4.2 the ISW and Rees-Sciama effect

In a ΛCDM universe, the dominance of the cosmological constant, $\Lambda$, causes the expansion factor of the universe, $a$, to grow at a faster rate than the linear growth of density perturbations, $\delta$. Consequently the cosmological constant has the direct dynamical effect of causing gravitational potential perturbations, $\Phi \propto -\delta/a$, to decay. The ISW effect is caused by the change in energy of CMB photons as they traverse these linearly evolving potentials. A CMB photon passing through an overdense region, or cluster, will gain more energy falling into the potential well than it later loses climbing out of the evolved shallower potential well. Therefore, overdense regions correspond to hot regions in a linear ISW map. The converse is true for a photon passing through an underdense region. Here the potential fluctuation is positive and the CMB photon loses more energy climbing the potential hill than it subsequently regains from its descent. Therefore, underdense regions appear cold in a linear ISW map. Non-linear growth of the density perturbations modifies this picture, producing additional temperature perturbations known as the RS effect. In overdense regions the accelerated non-linear growth of structure acts to increase the depth of the potential wells resulting in a reduction in the CMB temperature, partially cancelling the ISW effect. In contrast, in underdense regions the RS effect enhances the ISW effect as saturation of the density contrast in voids further suppresses growth of the gravitational perturbation. We will discuss other situations in which the RS effect makes a significant contribution and analyze the morphology of the resulting features in the sky maps in §4.5. We have laid down basic equations for the computing the ISWRS effect in the last chapter. For the convenience of illustration in this chapter, we summarised them in the following.

The net induced ISWRS temperature fluctuation along a direction $\hat{n}$ can be written as

$$\Delta T(\hat{n}) = \frac{2}{c^3}\bar{T}_0 \int_0^{r_{\rm L}} \dot{\Phi}(r,\hat{n})\, a\, dr, \tag{4.1}$$

where $\dot{\Phi}$ is the time derivative of the gravitational potential, $c$ is the speed of light, $r_L$ is the comoving distance to the last scattering surface and $a$ the expansion factor.

To accurately compute $\dot{\Phi}$ from our simulation we make use of the Poisson equation expressed in comoving coordinates, $\bigtriangledown^2\Phi(\vec{x},t) = 4\pi G\bar{\rho}(t)a^2\delta(\vec{x},t)$, which can be written in Fourier space as

$$\Phi(\vec{k},t) = -\frac{3}{2}\left(\frac{H_0}{k}\right)^2 \Omega_{\rm m}\frac{\delta(\vec{k},t)}{a}. \tag{4.2}$$

Here $\bar{\rho}(t)$ is the mean density of the universe, $\delta$ is the density contrast $\delta \equiv (\rho - \bar{\rho})/\bar{\rho}$, $H_0$ and $\Omega_{\rm m}$ are the present values of the Hubble and matter density parameters and G is the gravitational constant. Taking the time derivative yields

$$\dot{\Phi}(\vec{k},t) = \frac{3}{2}\left(\frac{H_0}{k}\right)^2 \Omega_{\rm m}\left[\frac{\dot{a}}{a^2}\delta(\vec{k},t) - \frac{\dot{\delta}(\vec{k},t)}{a}\right]. \tag{4.3}$$

Combining this with the Fourier space form of the continuity equation, $\dot{\delta}(k,t) + i\vec{k}\cdot\vec{p}(\vec{k},t) = 0$, we have

$$\dot{\Phi}(\vec{k},t) = \frac{3}{2}\left(\frac{H_0}{k}\right)^2 \Omega_{\rm m}\left[\frac{\dot{a}}{a^2}\delta(\vec{k},t) + \frac{i\vec{k}\cdot\vec{p}(\vec{k},t)}{a}\right], \tag{4.4}$$

where $\vec{p}(\vec{k},t)$ is the Fourier transform of the momentum density divided by the mean mass density, $\vec{p}(\vec{x},t) = [1+\delta(\vec{x},t)]\vec{v}(\vec{x},t)$. Equation (4.4) enables us to compute $\dot{\Phi}$ (including the contributions of both the linear ISW effect and the non-linear RS effects) to high accuracy using the density and momentum fields of our simulation. We will refer to the results obtained using equation (4.4) as the ISWRS.

We wish to contrast these ISWRS predictions with the corresponding results from linear theory. In the linear regime, $\dot{\delta}(\vec{k},t) = \dot{D}(t)\delta(\vec{k},z=0)$, where $D(t)$ is the linear growth factor. Substituting this into equation (4.3) yields

$$\dot{\Phi}(\vec{k},t) = \frac{3}{2}\left(\frac{H_0}{k}\right)^2 \Omega_{\rm m}\frac{\dot{a}}{a^2}\delta(\vec{k},t)[1-\beta(t)], \tag{4.5}$$

where $\beta(t)$ denotes the linear growth rate $\beta(t) \equiv d\ln D(t)/d\ln a$. This equation represents the conventional way of modelling the ISW effect and uses only the information from the density field. It is equivalent to assuming that the velocity field is related to the density field by the linear approximation $\vec{p}(\vec{k},t) = i\dot{\delta}(k,t)\vec{k}/k^2 \approx i\beta(t)\delta(k,t)\vec{k}/k^2$. We will refer to results obtained using this linear approximation for the velocity field as LAV. Note that with this LAV approximation, $\dot{\Phi}$ simply scales with time according to the ISW linear growth factor $G(t) = \dot{a}D(t)[1-\beta(t)]/a^2$.

In the LAV approximation the density field $\delta$ directly determines the potential field $\Phi$ and its derivative $\dot{\Phi}$. Hence the morphology of the $\dot{\Phi}$ field is determined directly by the form of the density field $\delta$ with overdense regions ($\delta > 0$) corresponding to negative regions of $\dot{\Phi}$ and vice-versa for underdense regions. In contrast, for the exact calculation, represented by equation (4.4), this correspondence is broken and the dynamics of the density field play an additional direct role in determining $\dot{\Phi}$. This is fully discussed in §4.4.

## 4.3 Constructing full sky maps

In this section, we describe our method of constructing full sky maps of the ISWRS effect using our large simulation.

### 4.3.1 The Gpc simulation

To thoroughly investigate the ISWRS effect, we need to use a simulation of adequately large box size to include the very large scale perturbation modes (hundreds of Mpc) necessary to verify convergence with linear theory. At the same time, we need sufficiently high resolution to investigate the effects of small scale non-linearity on the structures we resolve in our sky maps. Moreover, for high accuracy ray-tracing, we need the redshift spacing of the simulation outputs to be small enough, so that interpolation between neighbouring redshifts does not introduce significant systematic errors.

The N-body simulation we have chosen is of $2200^3$-particles in a 1 $h^{-1}$Gpc periodic box. It is of a $\Lambda$CDM cosmological model, with $\Omega_\Lambda = 0.74$, $\Omega_\mathrm{m} = 0.26$, $\Omega_\mathrm{b} = 0.044$, $\sigma_8 = 0.8$ and $H_0 = 71.5$ km s$^{-1}$ Mpc$^{-1}$, chosen for consistency with recent CMB and large scale structure data (Sanchez et al., 2009). The simulation, run on the COSMA supercomputer at Durham, was designed in order to make mock galaxy catalogues for forthcoming surveys (e.g. Pan-STARRS1 and EUCLID) and as such resolves the dark matter halos of luminous galaxies (Baugh et al. 2009, in prep). The simulation has a softening length (plummer equivalent) of 0.023 $h^{-1}$Mpc which provides more than adequate resolution for our purposes. The initial conditions were set up at redshift $z = 49$, evolved using GADGET (Springel et al., 2005) and output at 50 snapshots, 48 of which lay between $z = 0$ and $z = 10$, where we mainly focus our analysis. The redshift intervals between neighbouring simulation outputs correspond to about 100 $h^{-1}$ Mpc in radial comoving distance. We have verified that this is adequate to ensure that the errors induced by interpolating $\dot{\Phi}$ between snapshots are less than 2% at Mpc scales and even less at larger scales.

### 4.3.2 Map construction

Our method of constructing the ISWRS sky maps has two stages. First, at each output redshift, we construct an estimate of $\dot{\Phi}$ on a cubic grid. In the second stage we propagate light rays from the observer and as we move along each ray we interpolate

$\dot{\Phi}$ from the grids and accumulate the $\Delta T$ defined by the integral of equation (4.1) along the past lightcone of the observer. Finally, we use HEALPix (Górski et al., 2005) to visualize the $\Delta T$ map in spherical coordinates. We now describe these steps in more detail.

#### 4.3.2.1 Cartesian Grids

We construct the density field, $\delta(\vec{x})$, by assigning the mass of each dark matter particle to a 3D mesh of cubic grid cells using the cloud-in-cell assignment scheme (Hockney and Eastwood, 1981). We apply the same assignment scheme to accumulate the momentum density field, $\vec{p}(\vec{x})$, by assigning the vector momentum of each particle to a cartesian grid. Then we perform four independent Fast Fourier Transforms to compute the Fourier space versions of of the density field $\delta(\vec{k})$ and three components of momentum field, $\vec{p}(\vec{k})$. These are then combined using equation (4.4) to yield the $\dot{\Phi}$ field in Fourier space. Finally, we do an inverse Fourier transform to obtain $\dot{\Phi}(\vec{x})$ in real space on a cubic grid. We repeat the final two operations using equation (4.5) to obtain the alternative LAV $\dot{\Phi}$ field. This whole process is then repeated for each of the 50 simulation outputs.

For our 1 $h^{-1}$ Gpc simulation, we have used a grid of $1000^3$ cells each of 1 $h^{-1}$ Mpc on a side. The resolution of N-body the simulation is significantly greater and would warrant using a finer grid. However this would be very demanding of both machine memory and hard disk space and is not necessary to accurately to resolve structures over 10 $h^{-1}$ Mpc, which is the smallest scale we are concerned with in this paper.

#### 4.3.2.2 Ray tracing through the lightcone

The next step is to choose a location for the observer and propagate rays through the simulation. We choose to place the observer at the corner of the simulation box at Cartesian coordinate (0,0,0). We then used HEALPix (Górski et al., 2005) to generate the directions of 3 145 728 evenly distributed rays, corresponding to an angular pixel scale of $(6.87')^2$ which is sufficient to resolve to a spherical harmonic scale of $l \sim 1000$. For each ray we accumulate the integral given by equation (4.1) by taking fixed discrete steps in comoving radial distance. At the location of each step we find the two output snapshots that bracket the lookback time at this distance. Using the Cartesian grids at each of these outputs we use the cloud-in-cell assignment scheme (Hockney and Eastwood, 1981) to obtain the values of $\dot{\Phi}_1$ and $\dot{\Phi}_2$ at the

chosen position on the ray at these two lookback times. Note that if the position along the ray takes us outside the simulation box we use the simulation's periodic boundary conditions to map the location back into the box. Finally to estimate $\dot{\Phi}$ at the lookback time corresponding to the position on the ray we linearly interpolate $\dot{\Phi}(t)/G(t)$ with comoving radial distance, $r$, using

$$(r_2 - r_1)\frac{\dot{\Phi}}{G} = (r_2 - r)\frac{\dot{\Phi}_1}{G_1} + (r - r_1)\frac{\dot{\Phi}_2}{G_2}. \tag{4.6}$$

Here $G$, $G_1$ and $G_2$ are the linear growth factors for $\dot{\Phi}$ at the lookback time corresponding to the position on the light ray and the two neighbouring outputs that bracket it. The values of $r$, $r_1$ and $r_2$ are the corresponding radial comoving radial distances. This interpolation scheme guarantees that we recover the linear theory result exactly when $\dot{\Phi}$ is evolving according to linear theory.

The maps that we present in §4.5 are constructed and analysed using the HEALPix package (Górski et al., 2005). We show maps corresponding to the contribution of the integral in equation (4.1) over different finite intervals of comoving radial distance. If we were to integrate over a comoving distance larger than the 1 $h^{-1}$Gpc box size of our simulation the periodic boundary conditions of the simulations would create artifacts in the maps. For instance, in directions corresponding to principal axes of the simulation box the light ray would pass through the same location of space every 1 $h^{-1}$Gpc. The contributions to $\Delta T(\hat{n})$ from these replicas would add coherently and lead to larger fluctuations along these special directions than on average. In similar applications some authors choose to rotate, flip and shift the replicated simulation box. While this avoids the artificial coherence between one replica and the next it generates other problems including discontinuities of $\dot{\Phi}$ at box boundaries. We have chosen to evade this difficulty by mainly focusing on generating and analyzing maps with a maximum radial depth equal to the simulation box size of 1 $h^{-1}$Gpc. It may still remain the case that the same structure can be seen in more than one direction, but this does not affect the mean power spectrum of the map and only produces non-gaussian features on angular scales approaching the angular size subtended by the simulation box. Hence the power spectra and small scale features of the maps that we analyze are not affected by the periodic nature of the simulation.[5]

[5]In fact, we find that if we ignore this issue and produce power spectra directly from maps projected over a depth of 7000 $h^{-1}$Mpc or more they do not differ significantly from those built up from the power spectra of successive 1000 $h^{-1}$Mpc slices. Hence at least for angular power spectra

It is also important to determine that the resolution of the maps we produce are not compromised by the spatial and temporal resolution of the simulation or our chosen size of grid cell and integration step. The pixel size of our HEALpix maps is $6.87'$ and matches the linear size of our Cartesian grid cells at an angular diameter distance of 500 $h^{-1}$ Mpc. Thus we would expect that beyond 500 $h^{-1}$ Mpc our sky maps are not lacking any small scale features due to the limited resolution of our cubical grids. We have tested this using a smaller simulation of the same resolution but grided using 0.5 rather than 1 $h^{-1}$ Mpc cells. This test indicates that at $l = 100$, the larger, default, choice of cell size suppressed the power in the maps made from the innermost 250 $h^{-1}$Mpc by just 10%. As we ray-trace further in radial direction the accuracy improves, being within 10% for $l \sim 1000$ for maps extending to 1000 $h^{-1}$Mpc. Additional tests have shown that it is this cell size which is limiting factor in the resolution of our maps. For instance we have checked that the maps are essentially unchanged if one makes the integration step size smaller than our default choice or if we have more closely spaced simulation outputs. The full resolution of the N-body simulation could be exploited by using a finer mesh but this is not only computational demanding but also unnecessary for the resolution of the maps we present and analyze.

## 4.4 The Effects of Non-linearity

In this section we compare our full non-linear estimates of the ISWRS effect with those of the LAV approximation. We both quantify and characterise the features that are generated by non-linear gravitational evolution and elucidate the physical processes by which they are generated.

Fig. 4.1 shows the temperature maps at three different redshifts that result from computing the contribution to the ISWRS integral equation (4.1) from a $100h^{-1}$ Mpc thick slice of the Gpc simulation. The top row are the full ISWRS calculation in which $\dot{\Phi}$ is computed using equation (4.4), while the middle row are the result of using the LAV approximation for $\dot{\Phi}$ given by equation (4.5). The LAV differs slightly from the ISW contribution to the temperature fluctuations because to compute the ISW one should really use the linear theory prediction for density field in equation (4.5),

our box size is sufficiently large and the evolution of $\dot{\Phi}$ sufficiently rapid that the superposition of periodic replicas is not a concern.

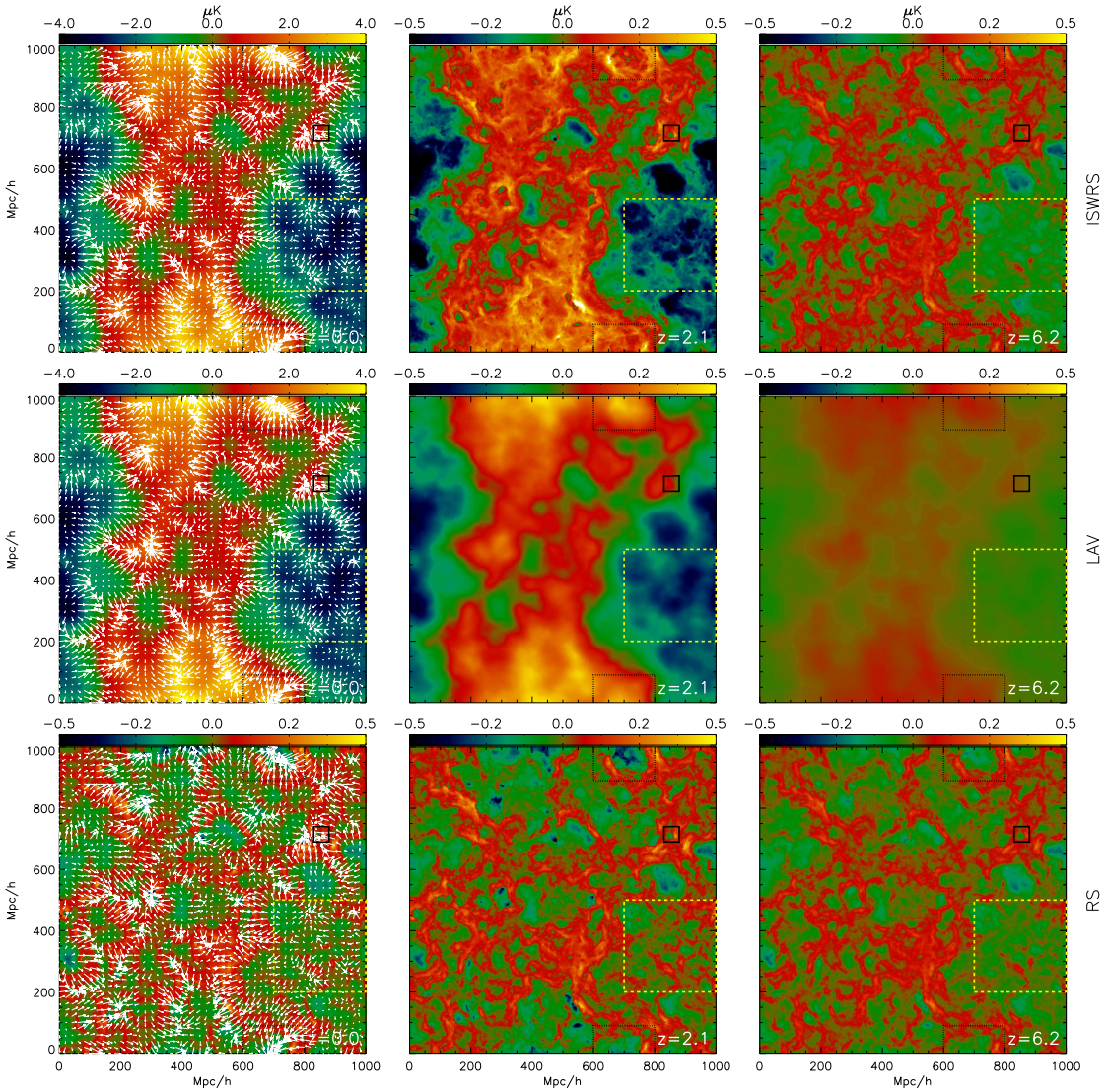


Figure 4.1: Maps of $\Delta T$ generated from a slab of thickness $\Delta r = 100h^{-1}$ Mpc taken from our Gpc simulation. From the left to the right, they are maps at $z = 0.0$, 2.1, 6.2 respectively. From the top to the bottom, they are maps constructed using equation (4.4), which includes the ISW and Rees-Sciama effect (ISWRS), maps constructed using linear approximation for the velocity field, equation (4.5), (LAV), and residual maps of the top panels minus the middle panels, leaving essentially the Rees-Sciama (RS) contribution to the temperature fluctuations. Note the individual temperature scales for each panel. At $z = 0$, we also indicate the momentum field, averaged over the same slice of the simulation, by the over plotted arrows. The three square boxes indicate the three regions we show in detail in Fig. 4.3 (solid-black box), Fig. 4.5 (dotted-black box) and Fig. 4.6 (dashed-yellow box).

whereas for the LAV we use the actual non-linear density field, but assume the velocity field is related to the density as in linear theory. However the difference between the LAV and the true ISW contribution is extremely small, as we shall see when we compare their power spectra in §4.5. Consequently the bottom row of panels, which are the residual produced by subtracting the LAV maps from the corresponding ISWRS maps, are essentially the RS contribution to the temperature fluctuations.

Looking first at the LAV maps, we see that the hot (red/yellow) and cold (blue/green) spots have a large coherence scale, approaching the size of our simulation box. The coherence scale is much larger than that of the underlying density field simply because of the $k^{-2}$ factor in equation (4.3) which arises from the Poisson equation relating $\Phi$ and $\delta$. As explained at the beginning of §4.2 hot (cold) spots in these maps are induced by the decay of the gravitational potential in overdense(underdense) regions caused by the dynamical effect of the cosmological constant, $\Omega_\Lambda$. As we move to the higher redshift slices the amplitude of the LAV/ISW fluctuations are greatly reduced. This is easily understood. As redshift increases $\Omega_\Lambda$ becomes smaller such that linear theory predicts density perturbations grow as $\delta \propto a$ and the corresponding potential perturbations $\Phi \propto -\delta/a$ are constant. For $\dot{\Phi} = 0$ there are no ISW fluctuations as CMB photons traversing such a potential well will lose just as much energy leaving the perturbation as they gain on entering it.

The RS contribution to the temperature fluctuations, shown in the bottom row of Fig. 4.1, have a much shorter coherence scale than the ISW fluctuations. Their evolution with redshift is much more gradual than for the ISW fluctuations. For the redshift $z = 0$ slice they are a minor contribution to the overall ISWRS map (top row), but they become a significant contribution at redshift $z = 2.1$, generating small scale structure within the smooth large scale ISW fluctuations. At $z = 6.2$ the RS fluctuations are almost completely dominant and while they are on a smaller scale than the ISW fluctuations they still produce filamentary structures which can be seen to be one hundred to a few hundreds of $h^{-1}$ Mpc across. These panels give a visual confirmation of the two-point statistics presented in Cai et al. (2009b), which demonstrated that both the importance and physical scale of the RS effect become greater with increasing redshift.

Fig. 4.2 compares the ISWRS and LAV temperature perturbations by comparing their contributions along three randomly chosen light rays (avoiding the principal

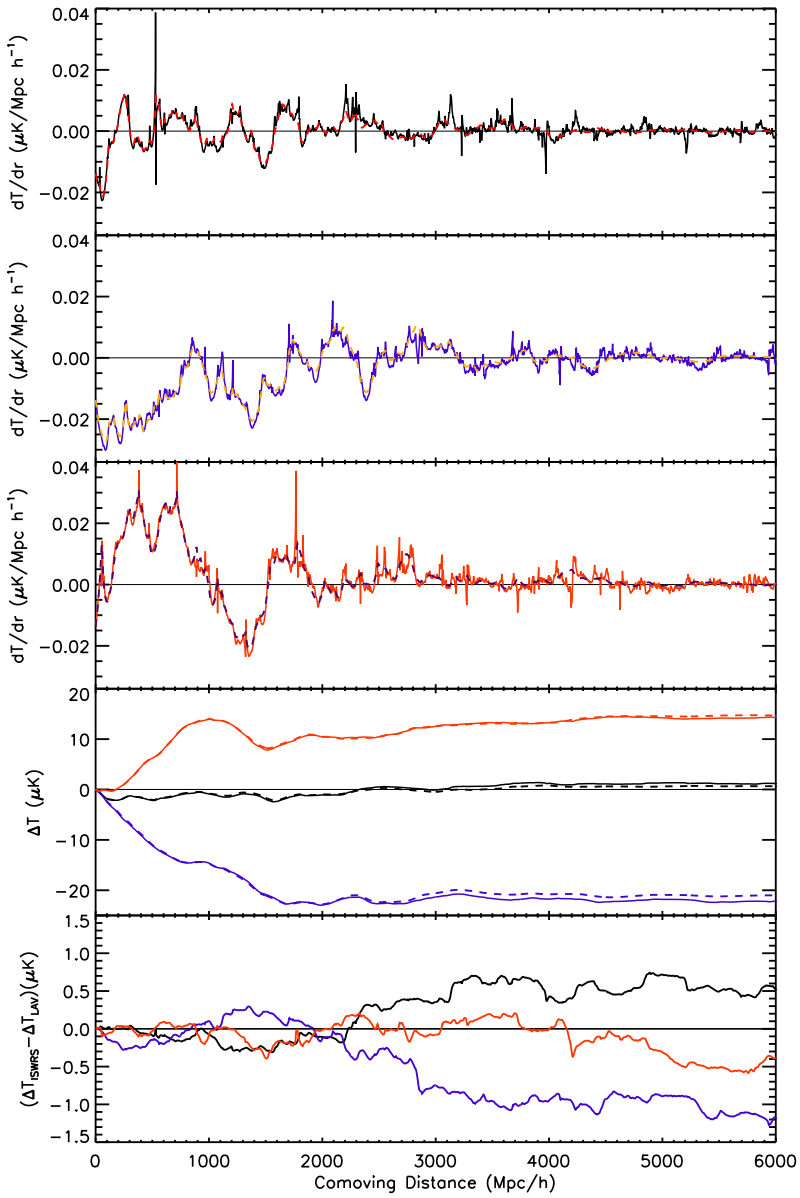


Figure 4.2: Temperature perturbations along three rays, shown in black, blue and red from $z = 0$ to $z = 5.8$, corresponding to the comoving distance from $r_c = 0$ to $r_c = 6000\ h^{-1}$ Mpc. Top three panels show the temperature perturbations per unit comoving distance along each of the radial direction. Solid lines show the results of full ISW and Rees-Sciama effects (ISWRS) and dash lines are results of the linear approximation for the velocity field (LAV). The fourth panel from the top shows the accumulated temperature perturbations along the radial direction for ISWRS (solid lines) and LAV (dash lines). The bottom panel shows differences between these accumulated ISWRS and LAV temperature perturbations.

axes of our periodic simulation box). In each of the top three panels the solid line shows the overall ISWRS perturbation and the smoother dashed line the LAV contribution from $z = 0$ to $z = 5.8$, corresponding to the comoving distance from $r_c = 0$ to $r_c = 6000\ h^{-1}$ Mpc. As in the maps of Fig. 4.1 we see that the LAV contribution varies more smoothly and rapidly damps in amplitude as one progresses along the rays to higher redshift. The RS contribution produces high-frequency fluctuations around the LAV predictions with the amplitude of these high-frequency fluctuations decreasing with redshift at a much more modest rate. The lower two panels of Fig. 4.2 show that while a large portion of the high-frequency RS signal cancels out when accumulated along the line of sight, persistent residuals of the order of 1 $\mu$K are also accumulated with a large contribution coming from the redshift range around a radial distance of about 2000 $h^{-1}$ Mpc.

In order to identify the non-linear physical processes that give rise to the persistent features in the ISWRS maps we have studied the momentum field of our simulation. The overlaid white arrows in the left-hand panels of Fig. 4.1 indicate the projected momentum field in this slice of the simulation. At higher redshifts we find that the orientation of the momentum vectors are similar but their amplitude increases, roughly in accord with the expected linear growth rate factor, $\beta$. In the LAV panel (middle row) we see that on large scales the momentum field is well correlated with the temperature perturbations and hence with the $\dot{\Phi}$ field. Dark matter particles are moving towards hot lumps (overdense regions, potential wells) and flowing away from cold lumps (underdense regions, potential hills). This is the scenario expected in linear theory. However if one looks at the smaller scale features evident in the ISWRS (top panel) maps one finds that this correlation between temperature and momentum does not always hold. In fact, at high redshift violations of the correspondence expected in linear theory are very strong. Hence, guided by the momentum field we have identified three interesting non-linear phenomena in the ISWRS maps, which are related to dipoles, convergent flows and divergent flows. Three regions exhibiting these phenomena are highlighted by the square boxes in Fig. 4.1 (one split across the periodic boundary of our simulation). We zoom in and study each in detail in the following subsections.

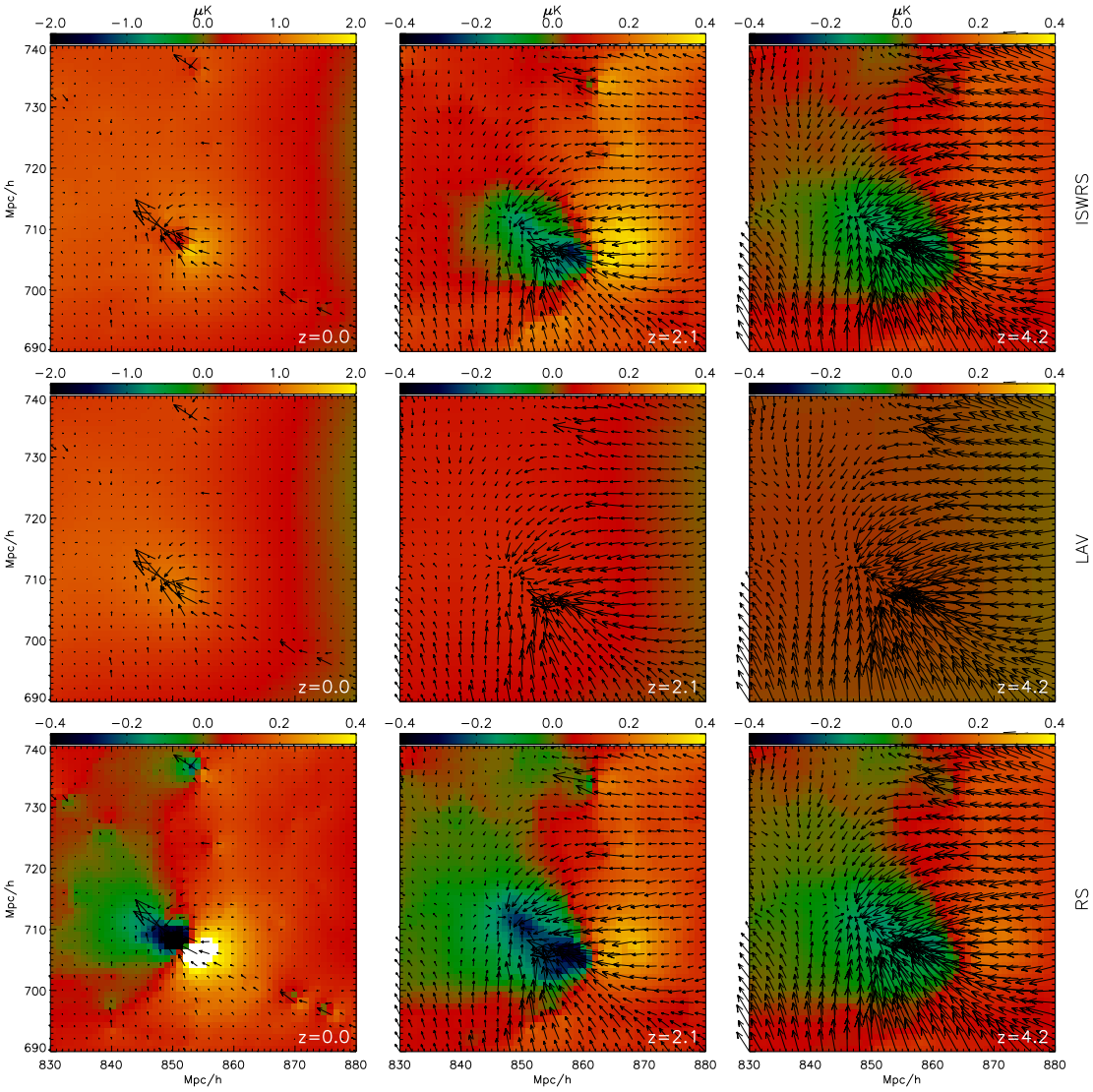


Figure 4.3: Maps of $\Delta$T in a slice of thickness $\Delta r$=50$h^{-1}$ Mpc with an area of $50\times50$ [$h^{-1}$ Mpc]$^2$. The $x$ and $y$ labels give the exact coordinates of this set of maps in the full-box maps shown in Fig. 4.1. From the left to the right, they are maps at $z = 0.0$, 2.1, 4.2 respectively. From the top to the bottom, they are maps constructed using equation (4.4), which includes the ISW and Rees-Sciama effect (ISWRS), maps with linear approximation for the velocity field, equation (4.5), (LAV), and residual maps of the top panels minus the middle panels, which is essentially the Rees-Sciama (RS) contribution. The overplotted arrows show the projected momentum field of the slice.

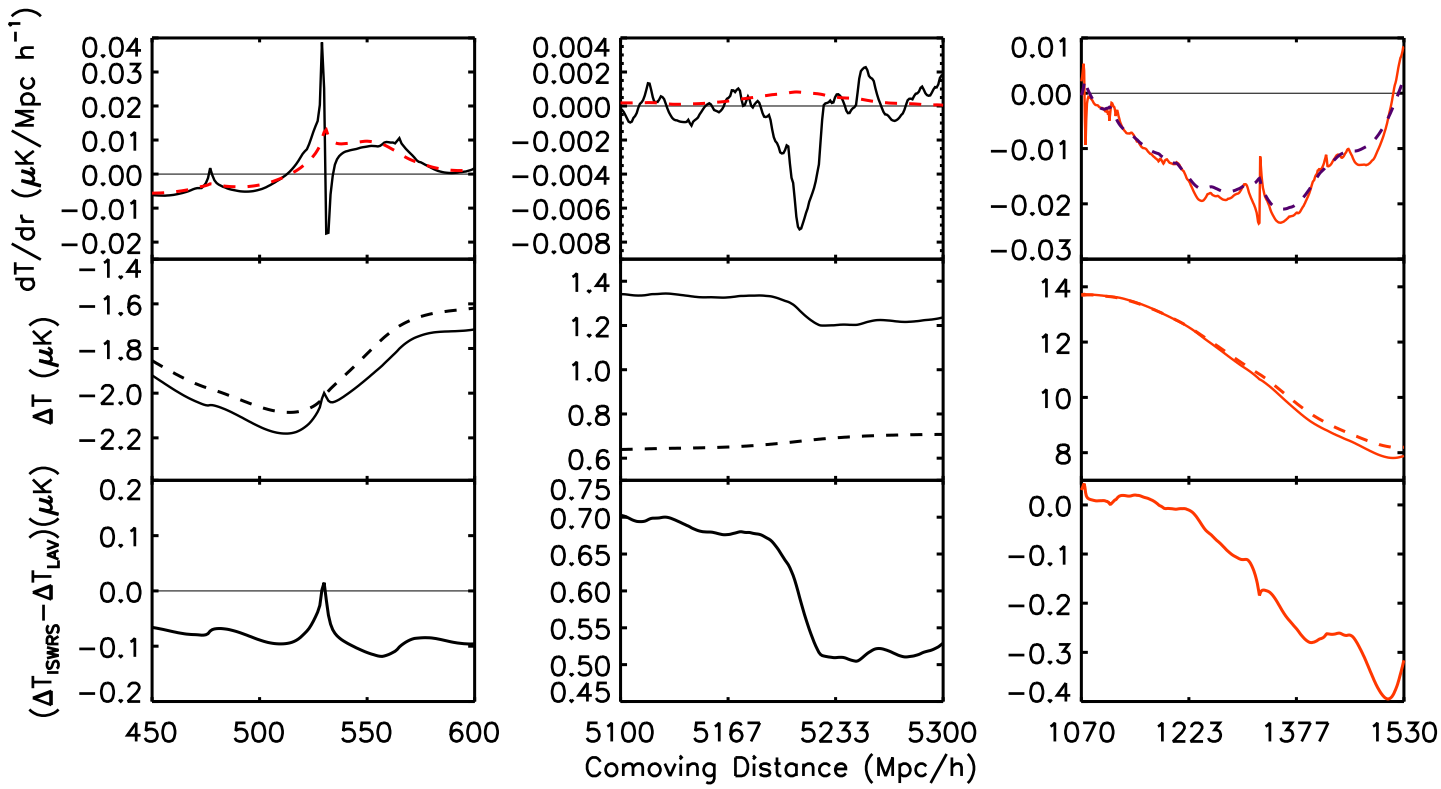


Figure 4.4: Segments of three rays shown in Fig. 4.2, with the distances shown on the $x$-axis. Top panels show the temperature perturbations per unit comoving distance in these chosen directions. Solid lines show the results of full ISW and Rees-Sciama effects (ISWRS) and dashed lines are results of the linear approximation for the velocity field (LAV). Middle panels show the accumulated temperature perturbations along the radial direction for ISWRS (solid lines) and LAV (dashed lines). Bottom panels shows the accumulated difference between the ISWRS and LAV perturbation. The left panel is an example of dipole, the middle panel is a convergent flow and the right panel is a divergent flow around an empty void.

### 4.4.1 Dipoles

In RS maps, at scales of tens of Mpc, large lumps of dark matter moving perpendicular to the line of sight give rise to dipole features, i.e. a cold spot on the leading part of the lump and a hot spot on the trailing part. Fig. 4.3 shows zoomed-in maps of the ISWRS, LAV and RS temperature perturbations at redshifts $z = 0$, 2.1 and 4.2 for a 50 $h^{-1}$Mpc region around one such dipole. The overplotted momentum vectors clearly show the bulk motion of a large lump of dark matter. We also see from the length of the arrows that this velocity is being damped and so decreases with decreasing redshift. The LAV maps are very smooth, showing no sign of dipole feature at all, while the strikingly large dipole with the amplitude of $\sim 1$ $\mu$K is clearly visible in ISWRS maps (top row), particularly at the higher redshifts. The physical origin of these dipole features, which are just a special case of the RS effect, can be understood in terms of the evolution of the gravitational potential, $\Phi$, on either side of the moving mass. At a fixed position ahead of the moving mass $\Phi$ decreases as the mass and its gravitational potential well approaches. This will create a CMB cold spot as CMB photons passing through this point will gain less energy falling into the potential well than they subsequently lose climbing out of the then deeper well. Conversely, behind the mass the $\Phi$ is increasing (becoming less deep) and so CMB photons gain more energy than they lose and this creates a hot spot.

As the maps we present in Fig. 4.3 are just the contributions to $\Delta T$ from a thin, 50 $h^{-1}$Mpc, slice of our simulation one might worry that this artificial truncation gives rise to artificial edge effects. We have checked that this is not the case by making corresponding maps projected through a depth of 1 $h^{-1}$Gpc, the box size of the periodic simulation. We find that the dipole features are still clearly visible, but of course they are somewhat perturbed by superposition of other perturbations along the longer line of sight. This finding is consistent with the accumulated difference between the ISWRS and LAV $\Delta T$ shown earlier in Fig. 4.2 (bottom panel), which although they have some small scale variation remain roughly constant for $r_{\rm c} > 3000$ $h^{-1}$Mpc.

The amplitude of the temperature fluctuation generated by such dipoles are not large, but their characteristic dipole signature might enable them to be detected (Rubiño-Martín et al., 2004; Maturi et al., 2006, 2007b). Dipoles generated by moving galaxy clusters, which can equally be thought of as 'moving lenses' were predicted

by Birkinshaw and Gull (1983) and later discussed by Gurvits and Mitrofanov (1986). Their detectability in the CMB and possible applications, such as measuring transverse motions of dark matter, have been further explored by Tuluie and Laguna (1995); Tuluie et al. (1996); Aghanim et al. (1998); Molnar and Birkinshaw (2000); Aso et al. (2002); Molnar and Birkinshaw (2003); Rubiño-Martín et al. (2004); Cooray and Seto (2005); Maturi et al. (2007b). These studies considered only dipoles on the scale of galaxy clusters while our simulations reveal dipoles of $\sim \mu$K amplitude on scales ranging from 10 $h^{-1}$Mpc to a few tens of $h^{-1}$Mpc, the larger of which are seeded by bulk motions on scales far larger than galaxy clusters.

Moving dark matter lumps will perturb the energies of CMB photons even if moving along rather than transverse to the line of sight. Examples of the perturbations such bulk motions cause are evident at several points along the rays shown in Fig. 4.2. One sees a sharp peak followed very closely by a deep dip. The left-hand panels of Fig. 4.4 show a close-up view of one these features. Following the ray on the top panel from the right to the left (i.e. moving in the direction of a CMB photon), the line dips and then peaks, indicating a lump of dark matter is moving in the opposite direction to the CMB photon. The local potential on the lump's leading part is getting deeper (cooling down photons) while on the trailing edge the potential is becoming shallower (heating up photons). The accumulated $\Delta T$ (middle panel) is boosted and then suppressed as the ray passes through and net effect is extremely small. This is to be contrasted to the case discussed previously when the lump moves transverse to the line of sight and for which there is no cancellation.

### 4.4.2 Convergent Flows

In the RS and the higher redshift ISWRS maps of Fig. 4.1 we see several examples of cold regions surrounded by hot rings or filaments which are centred on converging velocity flows. These features are larger in scale than the dipoles, ranging from scales of tens to hundreds of Mpc. Fig. 4.5 shows zoomed-in maps of the ISWRS, LAV and RS temperature perturbations and overlaid velocity vectors at redshifts $z = 0$, 2.1 and 6.2 for a 200 $h^{-1}$Mpc box centred on one such feature selected from Fig. 4.1. In the LAV maps (middle row) we see only a smooth hot lump, centred on the convergent flow, whose amplitude increases towards low redshift as $\Omega_\Lambda$ becomes increasingly important. In contrast the RS contribution to the temperature perturbations (bottom row) is negative at the centre of the convergent flow and is

surrounded by a positive shell. Its amplitude evolves with redshift much more weakly than the amplitude of the LAV perturbation. It is strongest in the central panel, decreasing at the lowest redshift due to the damping of non-linear growth rate by the late time acceleration of the universe. At all but the lowest redshift this RS perturbation is a significant contribution to the overall ISWRS maps (top row). At high redshift the RS completely dominates over the LAV contribution turning the hot spot predicted by linear theory into a cold spot, almost 200 $h^{-1}$Mpc in extent, with amplitude of order a $\mu$K surrounded by a hot shell. Even in the redshift $z = 2.1$ slice, the RS contribution drastically changes the morphology of the LAV hotspot, producing a cold region in the very centre of the flow that is surrounded a hot filamentary shell.

The explanation of this counter-intuitive conclusion that overdense regions can become cold spots surrounded by hot-rings, rather than the hotspots predicted by the ISW, involves principally the same physics as is responsible for the dipoles. In the $\Lambda$CDM model overdense regions grow as the result of the inflow of lumpy material, often along filaments. Each of these inflowing lumps will give rise to a dipole feature. On the leading edge of the lump the potential is decreasing and CMB photons lose energy, while on the trailing edge the potential is increasing and CMB photons are heated. The only difference is that dipoles seen on the sky are indicators of lumps of dark matter with large transverse momentum, while these larger scale cold regions surrounded by hot rings are produced by larger scale coherent convergent flows. One can imagine splitting the convergence flow into many small lumps of dark matter moving towards the same centre, the cold region in the centre is just the result of stacking of many leading parts of those lumps, while the hot ring consists of their trailing parts. Our findings regarding the morphology of the RS effect in converging flows are in general agreement with analytic models of forming clusters that have been discussed by many authors (e.g. Martinez-Gonzalez and Sanz, 1990; Lasenby et al., 1999; Dabrowski et al., 1999; Inoue and Silk, 2006, 2007).

The maps shown in Fig. 4.5 are the contribution to the $\Delta T$ perturbation of just a 100 $h^{-1}$Mpc slice of our simulation. Again one should consider whether this truncation gives rise to artificial edge effects that would qualitatively effect the appearance the cold spots and hot rings. In particular if the slice artificially removes a foreground or background section of the hot shell this will enhance the visibility of the cold central region. We have directly tested whether this is a strong effect by

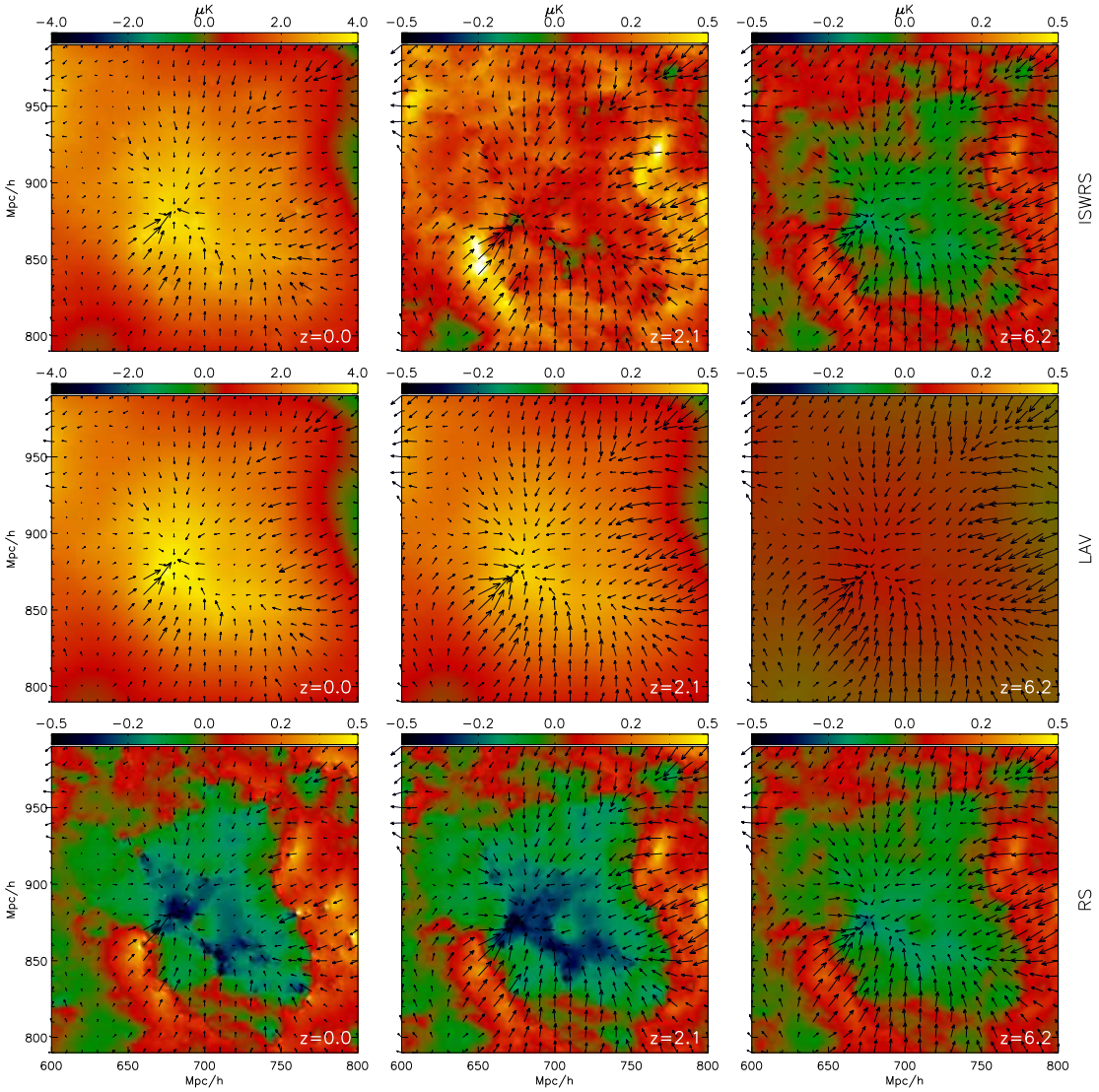


Figure 4.5: Like Fig. 4.3 but for slice of thickness $\Delta r$=100$h^{-1}$ Mpc, with an area of a $200\times200$ $[h^{-1}\ \mathrm{Mpc}]^2$ centred on a convergent flow. From the left to the the panels are of maps at $z = 0.0$, 2.1, 6.2 respectively. Note that the region we show here lies at the boundary of our simulation box (see Fig. 4.1. To show it properly, we shifted our simulation box along the $y$-axis by $-100\ h^{-1}$ Mpc using the periodic boundary conditions, so that the $y$-axis ranges shown in maps correspond the combination of 890 to 1000$h^{-1}$ Mpc and 0 to 90$h^{-1}$ Mpc in the original simulation box.

making untruncated maps whose depth is the full 1000 $h^{-1}$Mpc size of the periodic simulation. We find that while there are some cases where the heating and cooling cancel each other out, normally the visibility and contrast of the cold spot and hot ring features is not strongly affected. This is perhaps to be expected as the hot shell is diluted, being spread over a much larger area than is subtended by the cold spot. Moreover, the dominance of the cold spots can be seen directly in the plots of the $\Delta T$ contributions along particular lines of sight. An example of a ray passing through a cold spot is shown by the middle column of Fig. 4.4. In the top panel the broad peak predicted by the LAV (dashed line) corresponds to an overdense region in the simulation. There is a convergent flow around this overdense region that gives rise to both the sharp central dip and surrounding upward fluctuations seen in the ISWRS result (solid line). The lower panels show that the difference between ISWRS and LAV perturbations is strongly dominated by the central cold spot.

### 4.4.3 Divergent Flows

Divergent flows surrounding voids or underdense regions also produce characteristic features in the ISWRS and RS maps. However their effect is not simply the reverse of that of the convergent flows. Instead the non-linear behaviour in these void regions always acts to enhance to the LAV perturbation producing stronger cold spots. Fig. 4.6 shows zoomed-in ISWRS, LAV and RS temperature maps of 300 $h^{-1}$Mpc region centred on such a cold spot. This region is underdense and the LAV maps (middle row) show the expected linear ISW behaviour of a cold spot which grows in amplitude with decreasing redshift as $\Omega_\Lambda$ increases and the potential hill associated with the underdensity decays. The RS contribution (bottom row) also produces a cold spot at the centre of the region, but surrounded by a hot filamentary shell. Thus, perhaps counter-intuitively, the pattern of the RS contribution for these divergent flows is the same and with the same sign as for the convergent flows discussed above. Again the amplitude of the RS contribution evolves with redshift much more weakly than the LAV contribution. At $z = 0$ the LAV contribution to the ISWRS is overwhelmingly dominant, but at higher redshift the RS effect contributes by reinforcing the linear effect in the centre of the cold spot and suppressing it in the outer regions.

The reason the effect of non-linearity in an underdense region is not simply the reverse of its effect in an overdense region is because the two situations are not symmetrical. The overdensity in an overdense region is unbounded while in a underdense

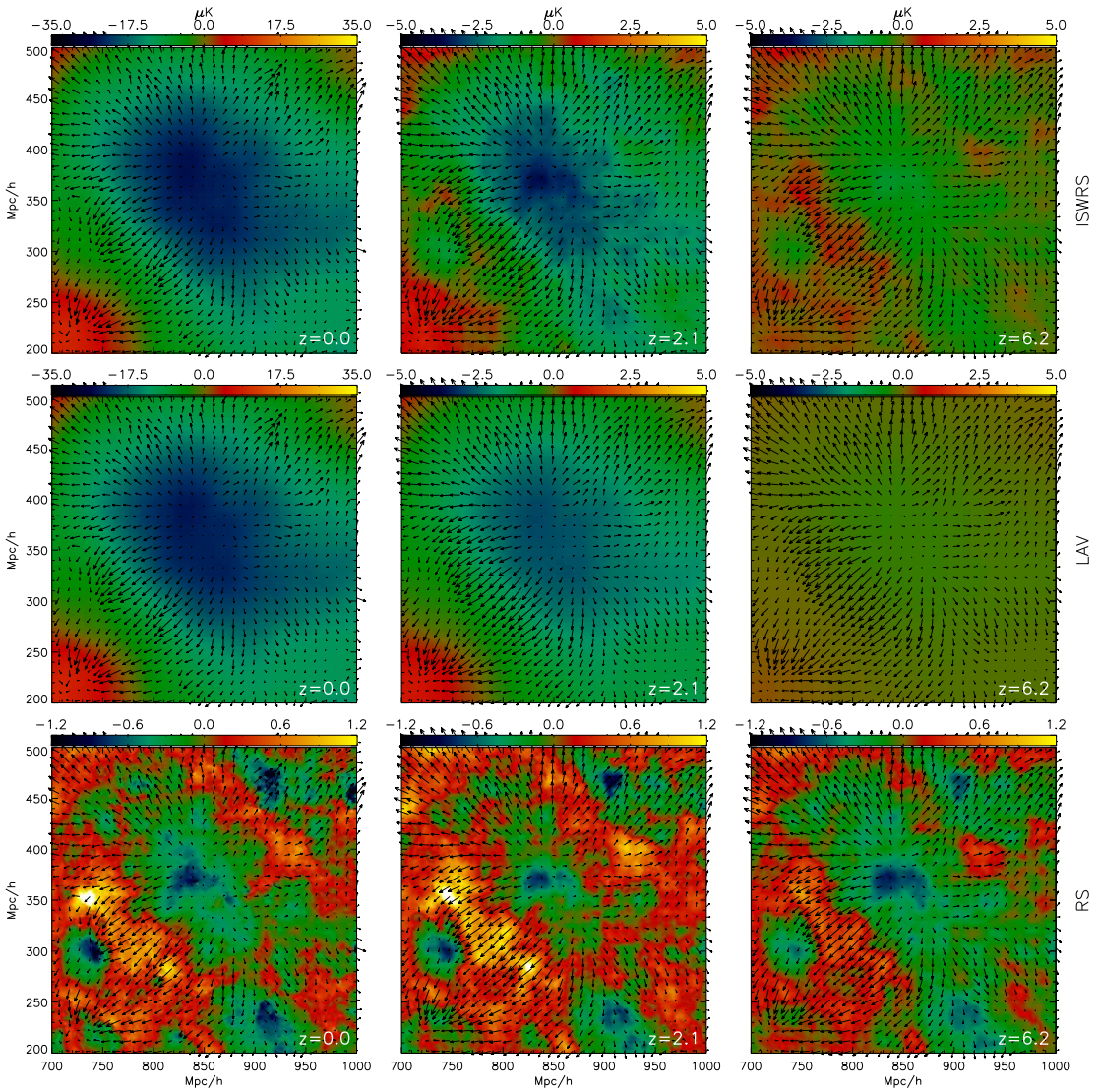


Figure 4.6: As Fig. 4.3, but for a slice of thickness $\Delta r$=1000$h^{-1}$ Mpc, with an area of $300 \times 300$ $[h^{-1}\ \mathrm{Mpc}]^2$ centred on a divergent flow. From the left to the the panels are of maps at $z = 0.0$, 2.1, 6.2 respectively.

region the density cannot drop below zero, $\delta > -1$. It is this saturation of the density contrast in voids that prevents the perturbation growing as fast as linear theory would predict and so enhances the rate of decay $\Phi$.

### 4.4.4 Overview of non-linearity

A useful summary of the three physical effects we have discussed above is given by the schematic diagrams plotted in Fig. 4.7. They depict the gravitational potential, $\Phi \propto -\delta/a$, at a baseline reference epoch, say when the CMB photon enters the region, and both the LAV and full non-linear predictions for the evolved potential at a later time, say when the CMB photon exits the region. These schematics yield a straightforward interpretations of each of the phenomena with have identified in the ISWRS and RS maps.

In void regions the ISW effect is easily understood as the result of the linear decay of the gravitational potential. CMB photons are cooled as they lose more energy climbing the initial potential hill of the void region than they subsequently regain on departing the now shallower potential hill. This cooling is depicted by the heavy arrows in the right-hand panel of Fig. 4.7. One would expect non-linearity to accelerate the growth of $\delta$ and hence increase the rate of growth of the potential hill. This is what we observe to occur at the edge of the voids and leads to a component of heating of the CMB photons in this outer shell, as depicted by the light upward arrows. However, once the centre of a void region become almost empty, i.e. $\delta \approx -1$, the local density contrast must stop growing, as it can not become any more empty. In this case, the expansion of the universe will reduce the height of the potential hill, just as it does in the linear regime in voids. Thus in the centre of voids the RS effect has the same sign as the linear ISW effect and the two reinforce each other to produce cold spots at the centre of voids.

In overdense regions such as galaxy clusters the linear decay of the gravitational potential well results in the heating of CMB photons as depicted by the heavy arrows in the central panel of Fig. 4.7. The effect of non-linear infall and growth of the density perturbation is to shrink the scale of the potential well while deepening its central value. In the centre of the cluster this non-linear growth acts in opposition to the linear decay of the potential and cools the CMB photons, depicted by the downward light arrow. We have seen that at high redshift this effect can be stronger than the linear ISW effect, resulting in cold spots centred on overdense regions. At

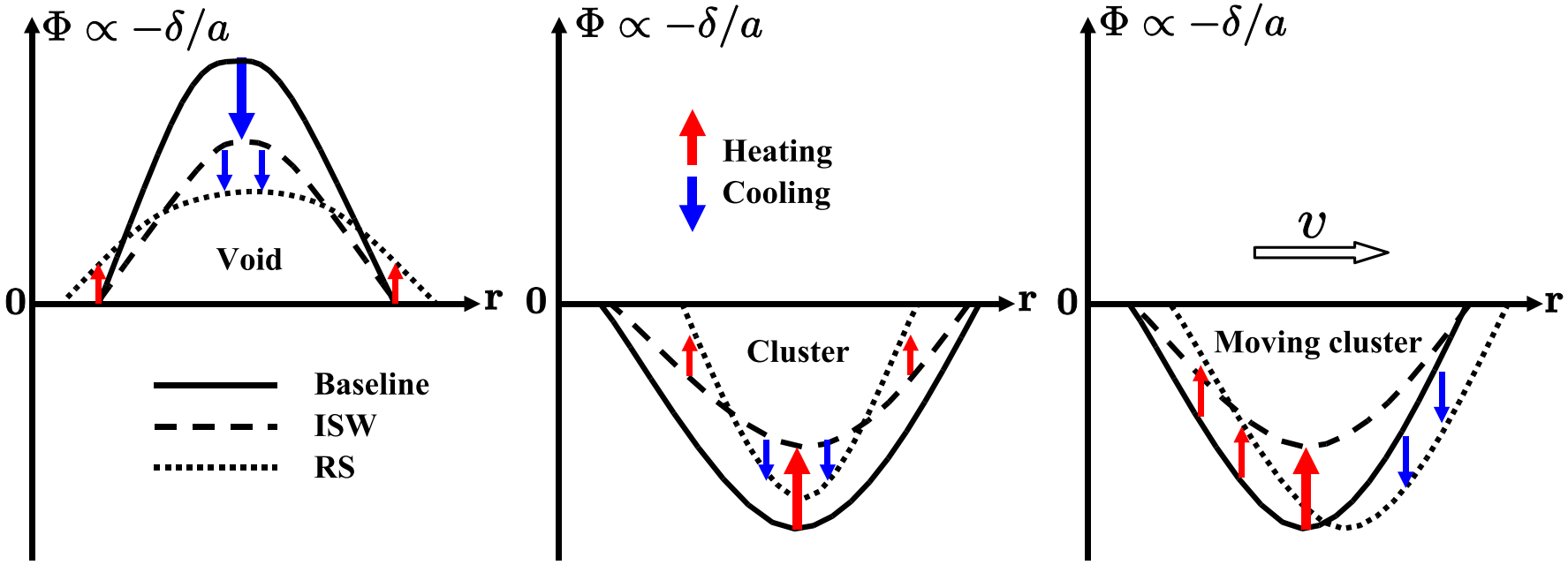


Figure 4.7: Schematic diagrams of the evolution of the gravitational potentials that produce the three characteristic features of the non-linear RS effect discussed in §4.4. The solid lines depict for a void (left), cluster (middle) and moving cluster (right) the gravitational potential at a reference epoch, say when a CMB photon enters the potential. The dashed and dotted lines indicate predictions for the evolved potential at a later point, say when the CMB photon exits the region. The dashed lines are the linear prediction of the LAV approximation and the dotted line represents the fully non-linear result. The heavy up and down arrows indicate the heating or cooling of the CMB that is predicted by the LAV approximation (essentially the linear ISW effect). The lighter arrows indicate the RS contribution to the temperature perturbations, i.e. the difference between the full non-linear and LAV contributions.

larger scales, the inflowing region shrinks the scale of potential well and results in a further reduction in the depth of the potential well, reinforcing the linear effect. Hence in an outer shell around the cluster the non-linear effect heats CMB photons. This latter effect can also be considered as the superposition of set of dipoles arising from lumps in a surrounding inflowing region.

The right-hand panel of Fig. 4.7 depicts the situation that gives rise to a characteristic dipole perturbation of the CMB. A moving cluster, or other overdense region, gives rise to a moving potential well. Linear theory does not model the movement of the potential well and would instead predict a simple static decaying potential well, resulting in a hot spot as indicated by the heavy upward arrows. In contrast the movement of the potential well leads to a rapid deepening of the potential well on the leading edge of the cluster and a corresponding rapid increase of the potential on the trailing edge. This gives rise to cooling of the CMB photons on the leading edge and heating on the trailing edge as indicated by the light arrows.

## 4.5 Sky maps

We have used the methods described in §4.3 to construct full sky maps of the ISWRS effect using both the density and velocity fields, and using the LAV approximation. We have also generated maps of the RS effect, by subtracting the LAV maps from the corresponding ISWRS maps. In all of the sky maps we have removed both the monopole and dipole using the REMOVE_DIPOLE subroutine of HEALPix (Górski et al., 2005).

The top panel of Fig. 4.8 shows the ISWRS map made by integrating along the line-of-sight of the observer over the range $0 < z < 0.17$, corresponding to distances from the observer, $r_c$, in the range $0 < r_c < 500h^{-1}$ Mpc. We see that the whole sky is dominated by a few large hot and cold features with amplitudes of a few $\mu$K to 10 $\mu$K, as expected from linear theory. The bottom panel shows the ISWRS map integrated from $0.17 < z < 0.57$, corresponding to $500 < r_c < 1500\ h^{-1}$ Mpc. The typical angular size of the features in this shell is smaller than in the top panel. As we will discuss later in this subsection, the smaller angular size of the features in the bottom map relative to the top map is due largely to the fact that the there is a cut-off in the power spectrum of the simulation used to build the sky maps. Unlike the real universe there is no power contributing to our maps on scales larger than

the fundamental modes of the simulation. This defect can easily be remedied: as the missing modes are essentially in the linear regime, it would be straightforward to simply add additional longer wavelength modes by hand before doing the line-of-sight projection to make the maps. This extra power however would be the same in maps of the ISWRS effect and the LAV approximation, and so would vanish identically from the maps of the RS effect. For this reason we have chosen not to add these linear modes to the ISWRS and LAV maps.

The corresponding maps, but with the LAV approximation, are shown in Fig. 4.9. Comparing and contrasting Fig. 4.8 with Fig. 4.9, we see that the large-scale distribution is essentially identical, but differences are apparent on smaller scales. The difference map made by subtracting the LAV map from the ISWRS map to reveal the RS effect, is shown in Fig. 4.10. In the top panel, covering the range $0 < z < 0.17$, we see some striking large-scale structures with amplitudes that are about $1\mu$K, which is about 10% of the amplitude of the features seen in the ISWRS and LAV maps themselves. A few large dipoles, ranging from a few degrees to over 10 degrees are clearly visible, indicating the large-scale bulk flow of matter in the local universe of our observer. The bottom panel shows the RS effect for a projection covering the range $0.17 < z < 0.57$. Many more dipoles are visible, with typical angular scales of a few degrees. In addition the map has large-scale filamentary structure which is coherent over lengths up to tens of degrees. The typical amplitude of these features is a few $\mu$K, again about 10% of the amplitude of the features in the corresponding ISWRS and LAV maps.

In Fig. 4.11 and Fig. 4.12 we show a patch of sky of size $40 \times 40$ degrees, for the redshift intervals of $0.57 < z < 1.07$ ($1500 < r_c < 2500h^{-1}$Mpc) and $1.07 < z < 1.78$ ($2500 < r_c < 3500h^{-1}$Mpc). For comparison, at $r_c = 3h^{-1}$ Gpc, the simulation box-size subtends an angle of about 18 degrees on the sky. We find, as expected, that the intensity of ISWRS and LAV maps drops with increasing redshift. However, the intensity of RS maps remains similar so that it is becomes relatively more important.

We now look at the one and two-point statistics measured from the maps. The results are summarised in the five Figs. 4.13 - 4.17 which correspond to the projections over the following respective ranges in redshift: $0 < z < 0.17$, $0.17 < z < 0.57$, $0.57 < z < 1.07$, $1.07 < z < 1.78$, and $0 < z < 10.3$. Starting with the bottom left-hand panels, we see that the histograms of the temperature fluctuations of the ISWRS and LAV maps are highly non-Gaussian at low redshift (particularly in Fig. 4.13

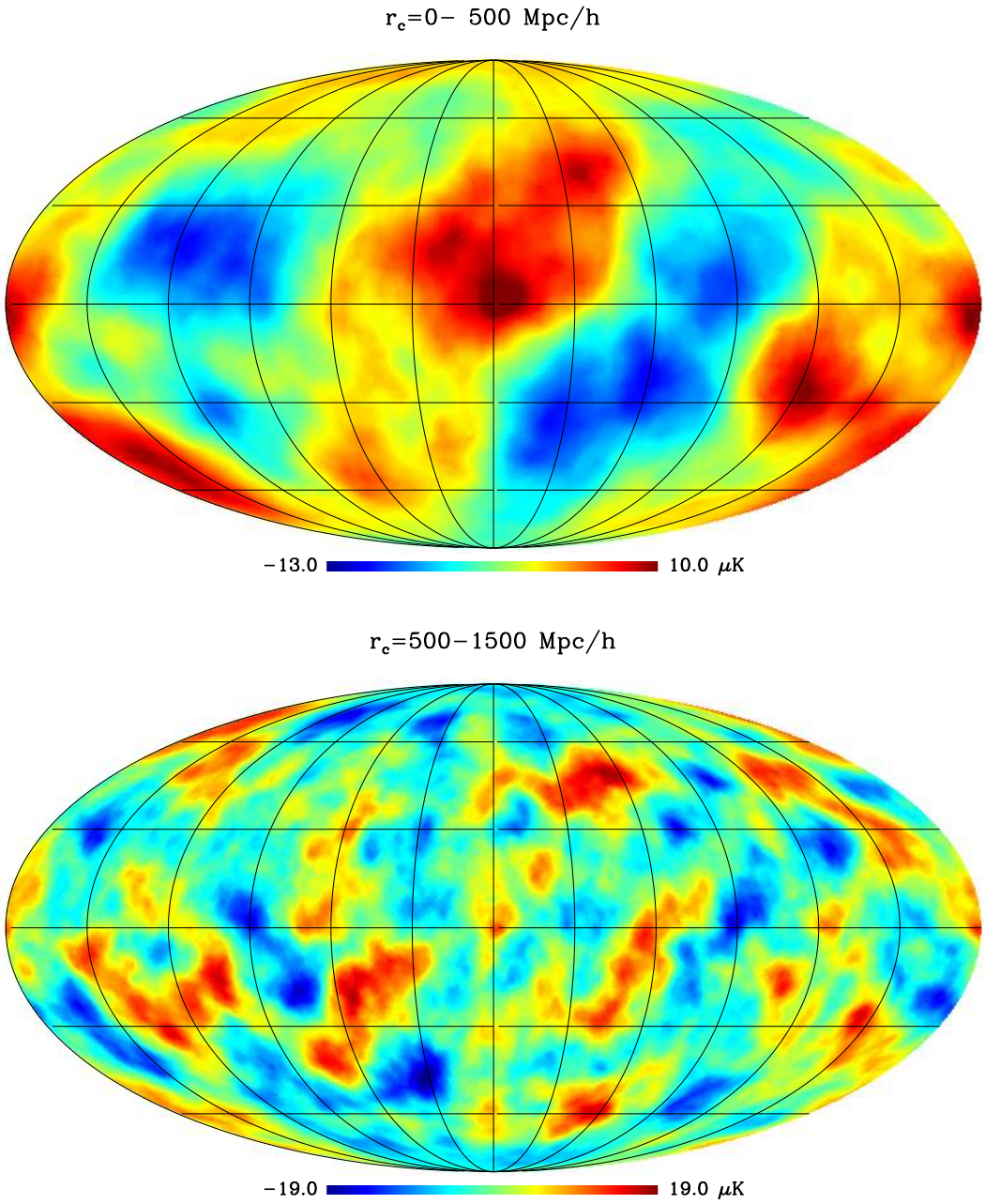


Figure 4.8: Full sky maps of the predicted CMB $\Delta T$ due to the ISW and Rees-Sciama effects (ISWRS) made from our simulation. The upper plot is made by ray-tracing through our simulation over the redshift interval $0 < z = 0.17$, which corresponds to a range of comoving distance from the observer of 0 - $500h^{-1}$ Mpc. In the lower plot the projection is for the range $0.17 < z < 0.57$ (corresponding to the range 500 - $1500h^{-1}$ Mpc in comoving distance). These maps, and all subsequent sky maps, use the Mollweide projection to represent the sky on a plane, with each pixel having an area of $(6.87')^2$. The grid spacing is 30° in both longitude and latitude. For reference the box-size of our simulation is 1000 $h^{-1}$ Mpc.

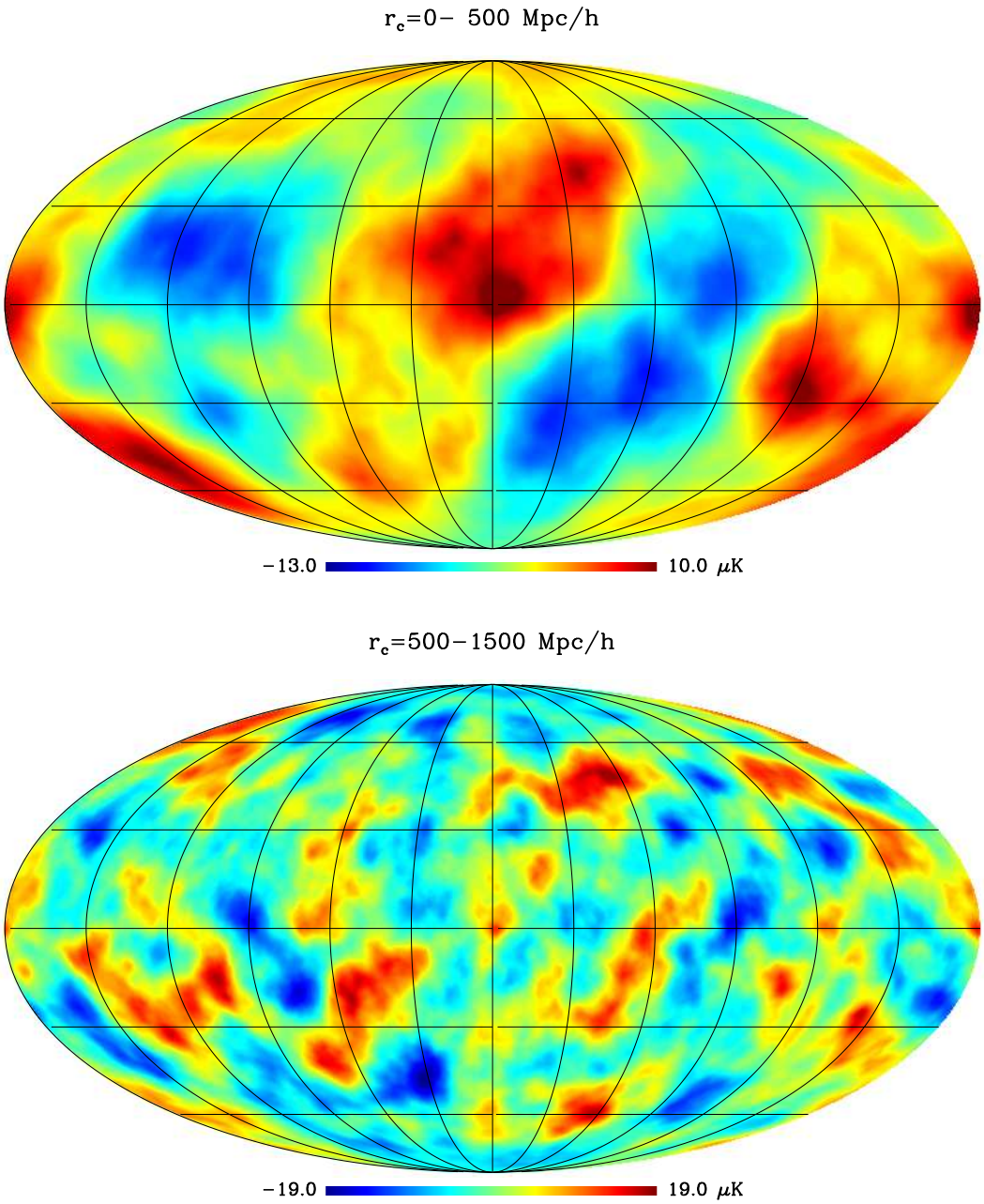


Figure 4.9: The same as Fig. 4.8 but showing the full sky maps of the predicted CMB $\Delta T$ due to the ISW effect constructed using the linear approximation for the velocity field (LAV).

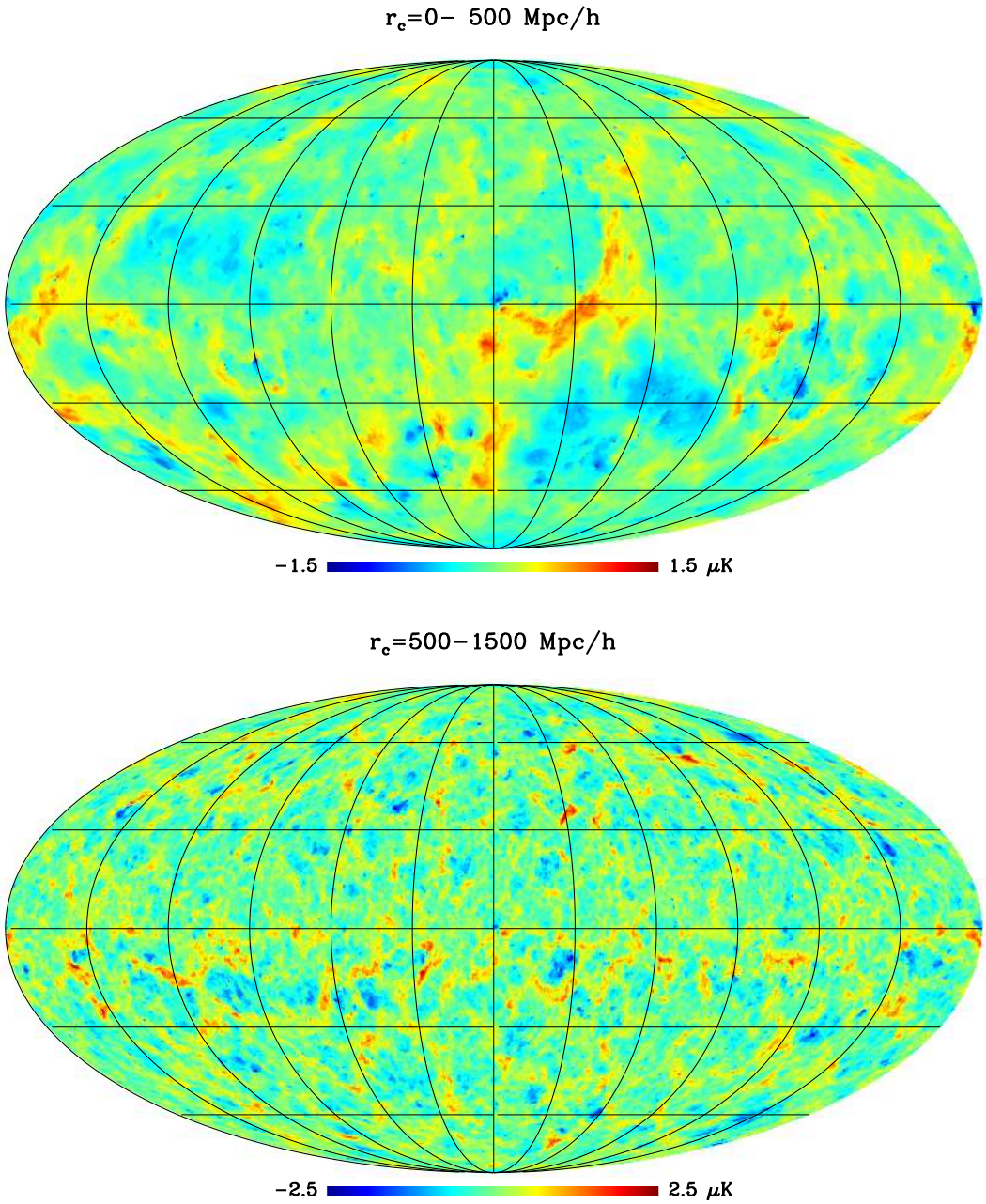


Figure 4.10: The Rees-Sciama (RS) effect, made by subtracting the maps in Fig. 4.9 from the corresponding map in Fig. 4.8. Note, because the simulation volume is only 1000 $h^{-1}$ Mpc on a side, that the same features may appear several times.

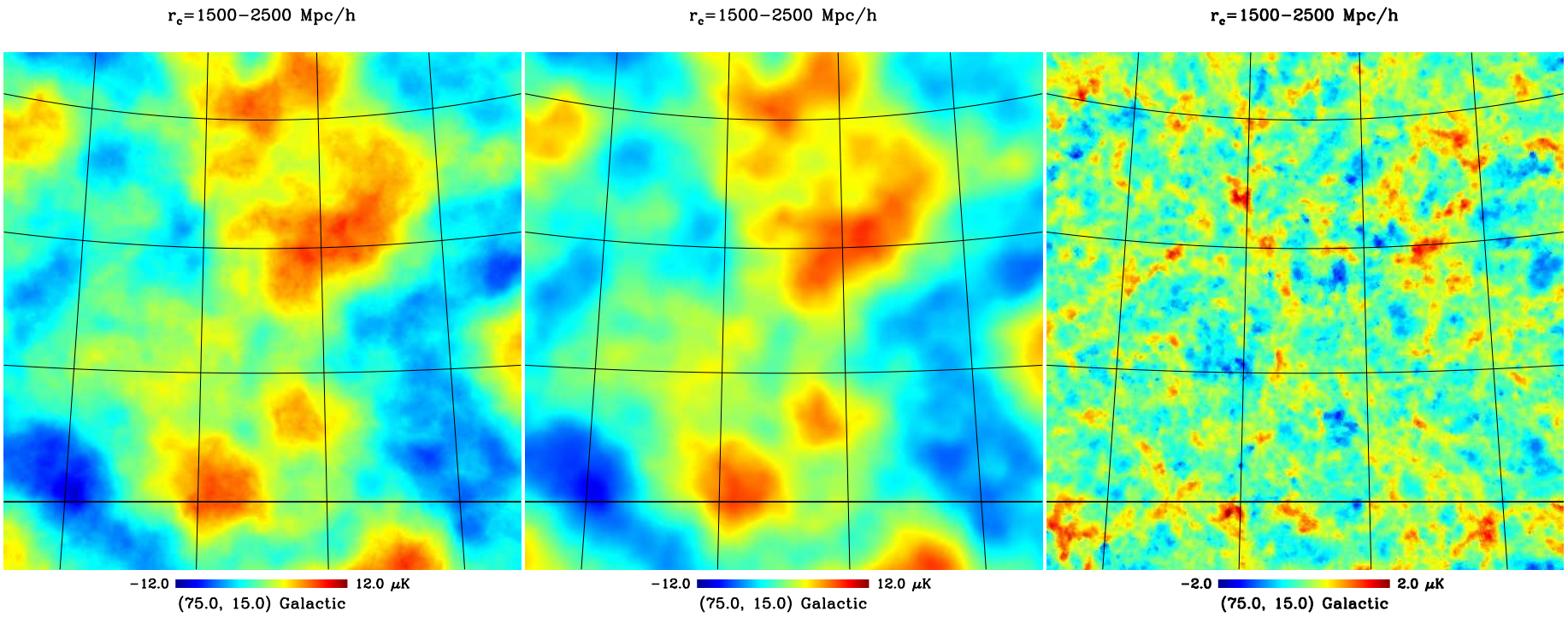


Figure 4.11: Sky maps from left to right of: (i) the ISW and Rees-Sciama effects (ISWRS); (ii) the linear approximation for the velocity (LAV); (iii) the Rees-Sciama (RS) effect. The projection is over the range $0.57 < z < 1.07$, corresponding 1500 - $2500h^{-1}$ Mpc comoving distance from the observer. The grid spacing is 10° in both longitude and latitude.

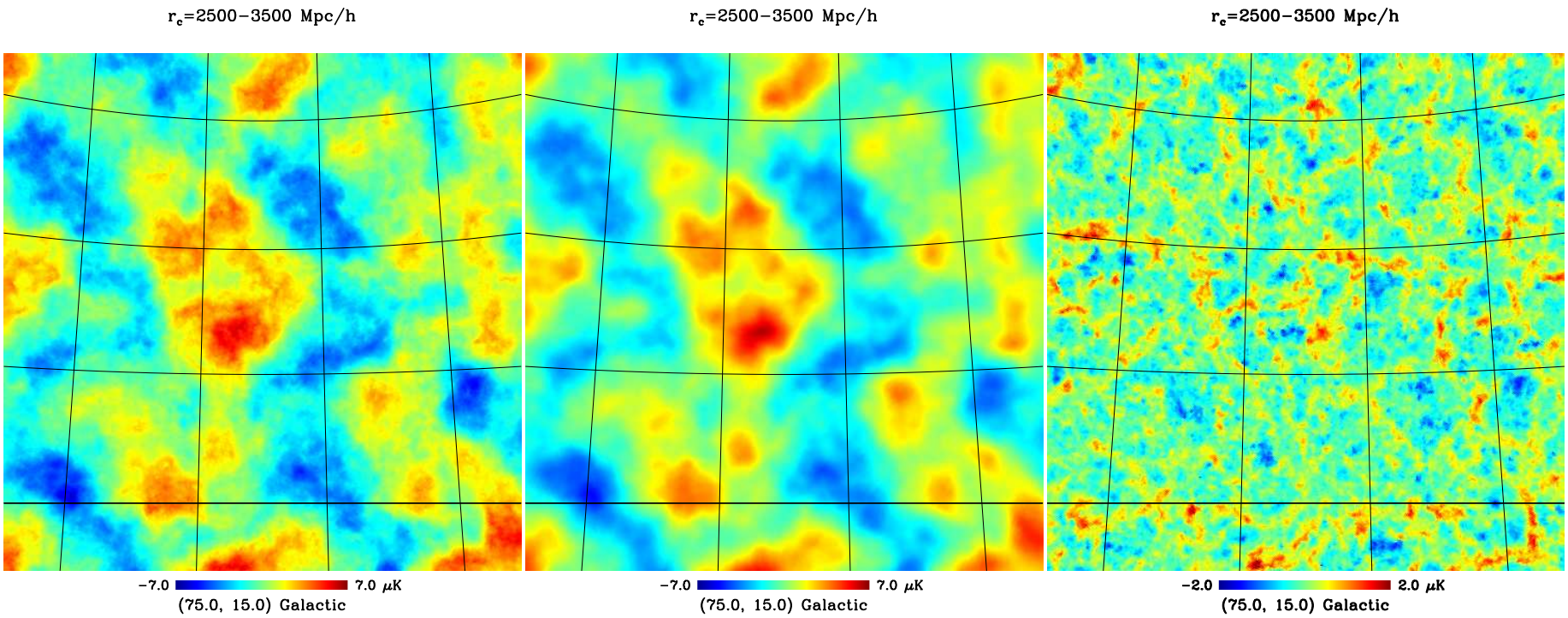


Figure 4.12: The same as Fig. 4.11 but projecting over the range $1.07 < z < 1.78$, corresponding to the comoving range 2500 - $3500h^{-1}$ Mpc. Note, because the simulation volume is only 1000 $h^{-1}$ Mpc on a side, that the same features necessarily appear at small angular scales as in the previous figure.

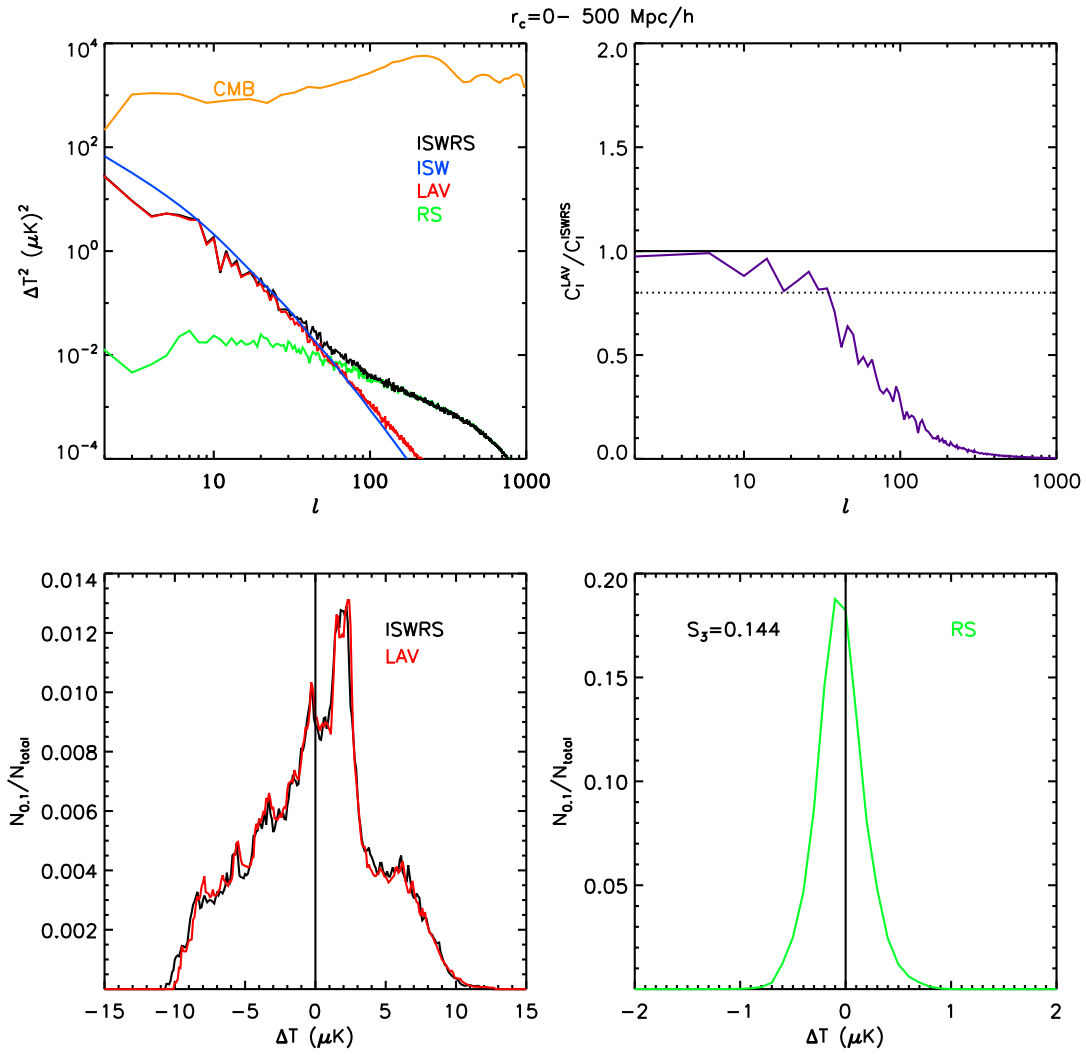


Figure 4.13: Statistics of the ISWRS, LAV and RS maps shown at the top panel ($0 < z < 0.17$) of Fig. 4.8, Fig. 4.9 and Fig. 4.10. Top-left: angular power spectra. The orange line at the top is the WMAP5 measurement of the CMB. The ISWRS power spectrum is shown in black line. The red line is the power spectrum of the map constructed by applying the linear approximation to the velocity field (LAV), i.e. equation (4.3). The blue line is the linear theory prediction for the same redshift interval. Top-right: The ratio of the LAV and ISWRS in the top-left panel. Bottom-left: the histogram of pixel temperatures of the IWRS (black) and LAV (red) maps. We divided the number of pixels within each bin of $0.1\mu$K by the total number of pixels. Bottom-right: the histogram of pixel temperatures of the residual map (RS). $S_3$ is the skewness of the map temperature.

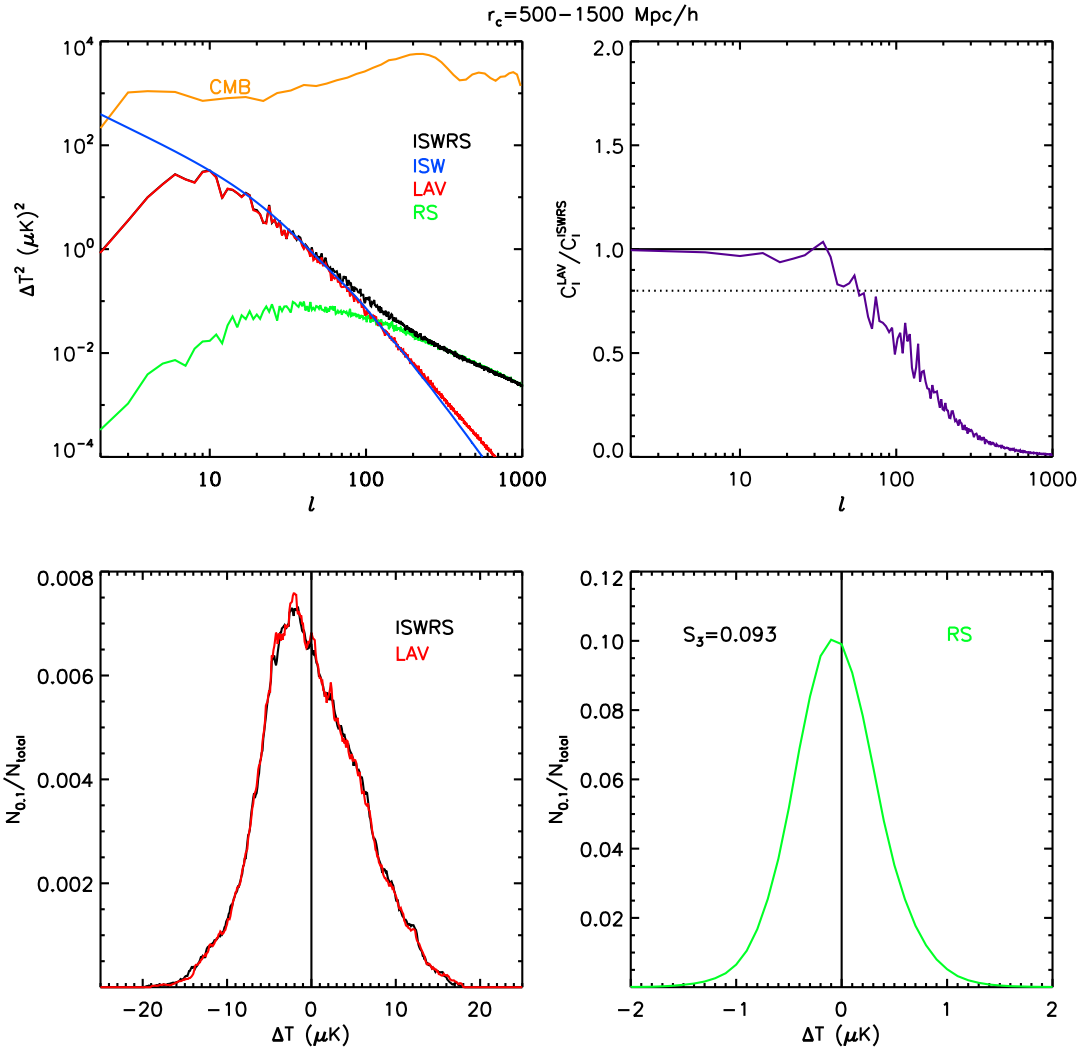


Figure 4.14: The same as Fig. 4.13 but showing the statistics for the maps in the bottom panel, projecting over the range $0.17 < z < 0.57$, of Figs 4.8, 4.9 and 4.10.

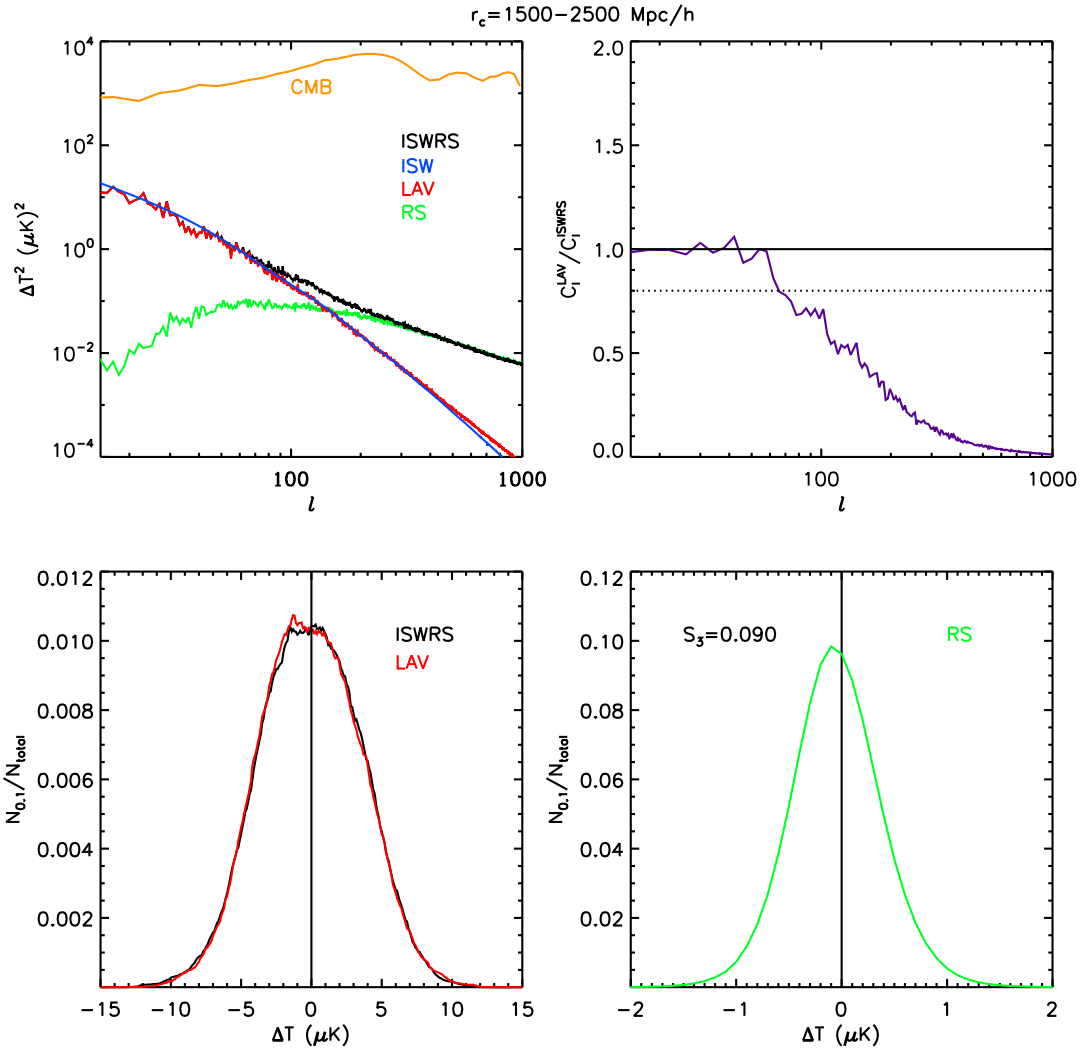


Figure 4.15: The same as Fig. 4.13 but showing the statistics for the maps in Fig. 4.11, projecting over the range $0.57 < z < 1.07$, corresponding to the comoving distance from 1500 to $2500h^{-1}$ Mpc.

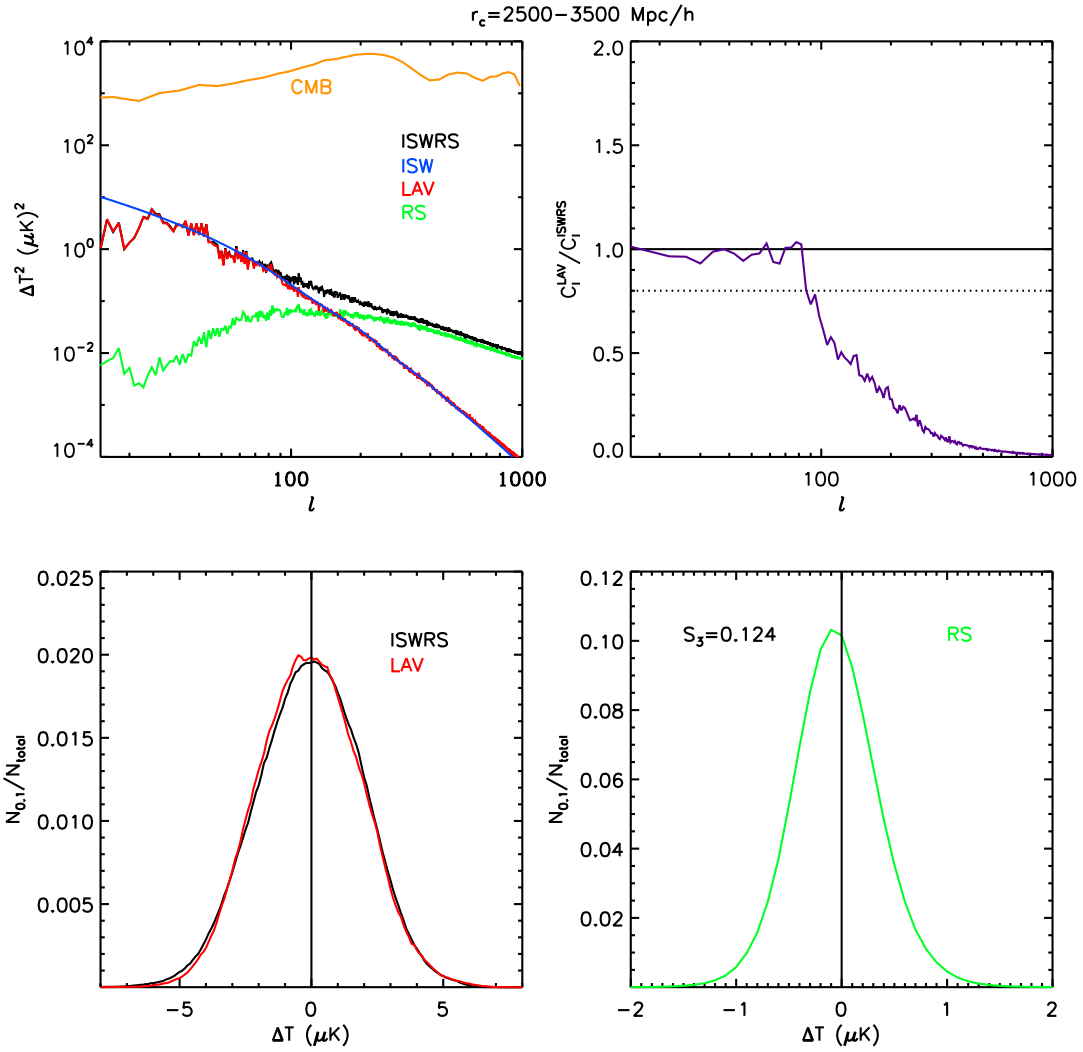


Figure 4.16: The same as Fig. 4.13 but showing statistics of maps shown in Fig. 4.12, projecting over the range $1.07 < z < 1.78$, corresponding to the comoving distance from 2500 to $3500h^{-1}$ Mpc.

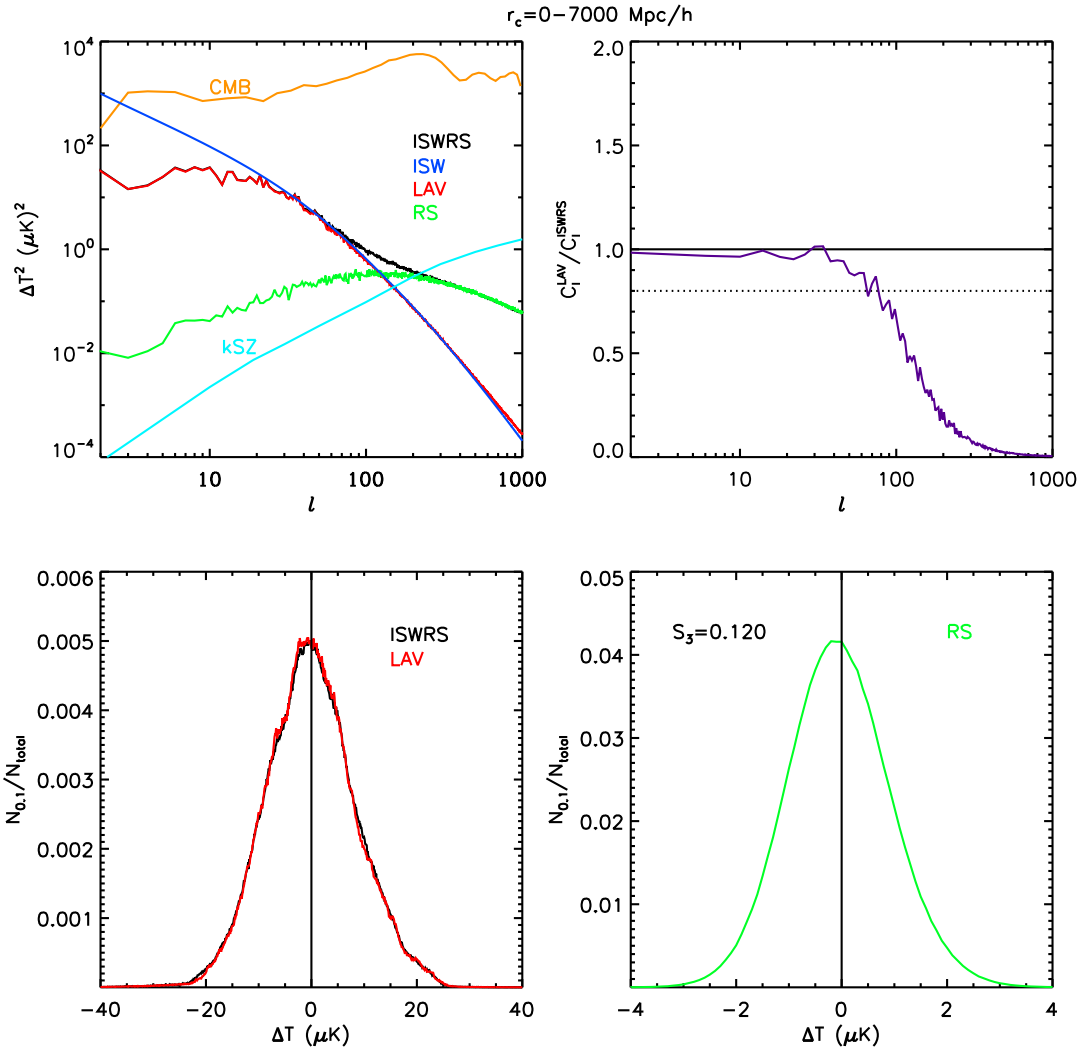


Figure 4.17: The same as Fig. 4.13 but showing statistics of maps from $z = 0.0$ to $z = 10.3$, corresponding to the comoving distance from 0 to $7000h^{-1}$ Mpc. The cyan line, in the top left panel, indicates the predicted kinetic SZ effect from Cooray (2001)

and Fig. 4.14), but are closer to Gaussian at higher redshifts. At low redshift the distributions are significantly skewed and irregular due to the fact that only a small number of features contribute to these maps. It is to be expected that potential variations in our local universe will also generate similar large-scale temperature fluctuations in the observed CMB and these too will be non-Gaussian. To quantify this effect on the observed CMB it is necessary to investigate the contribution of the local environment on scales up to at least a few hundred Mpc. See Maturi et al. (2007a) for discussion of the contribution from within 110 Mpc of Earth. At higher redshifts the relatively small size of the simulation box means that the same features will appear more than once in the maps, which will lead to some artificial residual non-Gaussianity, but only on large angular scales.

Although the one-point distributions are very similar there is a noticeble systematic difference between the histograms of the ISWRS and LAV effects at all redshifts. The ISWRS line is higher/lower than the LAV line in the negative/positive tails of the distribution. Because the monopoles of the maps have been set to zero, so the means of the distributions are the same, these features are indicative of difference in the skewness of the distributions. The bottom-right panel shows the one-point distribution of RS effect, given by the difference map formed by subtracting the LAV from the ISWRS map. The resulting distribution, which has a zero mean, is clearly skewed. Measuring the skewness of the RS distribution, $S_3 \equiv \mu_3/\sigma^3$, where $\mu_3$ is the third moment about the mean and $\sigma$ is the standard deviation of pixel temperatures, we find $S_3 \sim 0.1$ over all the redshift intervals. A positive value of skewness means the mass of the distribution is concentrated on the left of the peak, there are relatively more low values in the map temperatures. This skewness is a further indication, already visible in the RS sky maps, that the RS effect is significantly non-gaussian.

We show the results of the two-point statistics, in the form of the angular power spectrum, in the top-left panels for all five redshift ranges in Figs 4.13 - 4.17. The expected (linear) ISW angular power spectrum is shown as a blue line. Because the simulation we use to compute the maps is a periodic box, and there is no power on scales larger than the box, it is not surprising that the angular power in our maps drops below ISW prediction at the largest angular scales. The angular scale at which this departure occurs depends on the redshift range of the projection, and occurs at higher $l$ with increasing redshift. Our simulation box-size is $1000h^{-1}$ Mpc

on a side so there are waves in the simulation which are well described by linear theory. So as expected, over intermediate values of $l$, we find excellent agreement between our ISWRS (and LAV) maps and the ISW prediction. We plot the ratio of the ISWRS and LAV power in the top right panel. Using the LAV approximation significantly underestimates the power at large scales. Comparing the power in the LAV and ISWRS power spectra, we see that the LAV approximation underestimates the power by 20% at around $l = 35$ in Fig. 4.13. At higher redshift intervals the corresponding value of $l$ increases gently to around 90, for Fig.4.16. For the full projection, Fig.4.17 a 20% deviation occurs at around $l = 80$.

In Fig. 4.17 we have also plotted the power spectrum of the kinetic SZ (kSZ) effect taken from (Cooray, 2001) for a similar cosmological model. The thermal and kinetic SZ effects both arise due to Compton scattering of CMB photons off electrons in the ionized inter-galactic medium. The power spectrum of the thermal effect is about one order of magnitude greater than the kSZ effect at arc minute and degree scales (e.g. Cooray, 2001; Hu and Dodelson, 2002). However, the transfer of the thermal energy of the electrons to the CMB photons produces a characteristic distortion of CMB spectrum and so in multi-band CMB observations the SZ signal can be separated from that of the ISWRS. In contrast, the kSZ effect, which is due to the bulk motion of the ionized material, does not share this spectral signature and so cannot be separated from the ISWRS signal. At $l \approx 80$, where the RS effect begins to dominate that of the linear ISW contribution, the kSZ effect is more than an order of magnitude weaker than the ISWRS effect. However it has a much steeper power spectrum and becomes comparable to the ISWRS power at $l \sim 225$, corresponding to an angular scale of $\sim$0.5 degree. Thus on sub-degree scales both the ISWRS and kSZ effects must be considered. We note that their spatial characteristics are quite distinct. A moving lump composed of both dark matter and ionized gas moving towards/away from the observer along the line of sight will produce a kSZ hotspot/coldspot, but no RS disortion. In contrast if the lump is moving in the transverse direction it will produce a RS dipole, but no kSZ distortion.

### 4.5.1 Cold spots in the CMB?

So far, we have shown two mechanisms that can generate cold spots in the CMB maps from time-varying large-scale potentials. 1.) cold spots in overdense regions that arise from rapid convergence flow of dark matter into the centre. 2.) cold spots

in empty voids that are relevant to the slow outflow of dark matter and the expansion of the universe.

The first type of cold spot arises only in the strong non-linear regime. It will be cancelled out partly, if not completely, by its surrounding hot regions (hot rings arising from non-linearity and large-scale hot lump arising from linearity) when integrated along the line of sight. It is more significant at high-$z$. At low-$z$, when the linear ISW effect dominates, the amplitude of hot lumps is so high that the non-linear cold regions are very likely to be buried away [see Figs. 4.1, 4.5 and the full sky maps]. Note however that at high-$z$ of the ΛCDM universe, or in cosmologies without dark energy, such cold regions are only surrounded by hot rings. They are more likely to be detected. See also early studies of non-linearity in cluster regions (Martinez-Gonzalez et al., 1990; Martinez-Gonzalez and Sanz, 1990; Panek, 1992; Saez et al., 1993; Arnau et al., 1994; Fullana et al., 1994; Quilis et al., 1995; Quilis and Saez, 1998; Lasenby et al., 1999; Dabrowski et al., 1999). For overdense regions, around galaxy clusters and superclusters, we expect to see a temperature decrement at high-$z$, and a temperature increment at low-$z$. The typical amplitudes of these ISWRS features are a few $\mu$ K to over 10 $\mu$ K in the amplitude of $\Delta T$.

The second type of cold spot may arise in both the linear and non-linear regimes, and the sign of the linear and non-linear effects are the same. The total effect is more significant at low-$z$ as the linear effect is strongest there. Therefore, the second type of cold spots are expected to be "colder" and is more likely to be apparent in maps where the integration is along the whole line of sight. As shown by our nearby full sky maps, the decrement of temperature given by non-linearity in void regions is around 10%.

We now revisit CMB anomalies found in observations, in particular, the very cold spot found in the southern hemisphere (Vielva et al., 2004; Cruz et al., 2005; McEwen et al., 2005; Cruz et al., 2006; McEwen et al., 2006; Cruz et al., 2007; McEwen et al., 2008). This cold spot is estimated to have a temperature decrement of 73 $\mu$K at 4° resolution contributed by CMB secondary effect (Cruz et al., 2005). Previous studies have concluded that a void region within $z < 1$ at the order of 100 Mpc is needed to contribute $\Delta T/T \sim 10^{-5}$ via gravitational effects (Rudnick et al., 2007; Inoue and Silk, 2006, 2007; Tomita and Inoue, 2008; Masina and Notari, 2009a,b; Granett et al., 2009). However, such a huge void is very unlikely in the concordance cosmology.

As shown from our simulation, it is possible that the ISWRS effect can give rise

to cold regions of over 100 Mpc in extent due to void regions at low-$z$. The voids do not need be completely empty to give rise to cold regions. As long as the local density growth rate is slower than the expansion of universe, the region will appear cold. In recent times when the dark energy has begun to dominate these voids become most prominent. The temperature decrement contributed by such regions may be up to $20\mu$K, or $\Delta T/T$ close to $10^{-5}$, as has been shown in our sky maps. This amplitude however is still well below 73 $\mu$K . Therefore, we conclude that the temperature decrement due to the ISW and RS effect in voids in the concordance cosmology is not sufficient to explain the CMB cold spot, even though the size of such regions is of order a few degrees. Note that we just have one such large cold region in our simulation box $(1000\ h^{-1}\mathrm{Mpc})^3$. To have better understanding of large voids, one may need larger box simulations.

Another extreme CMB cold spot is associated with the Corona Borealis supercluster. A temperature decrement of $\Delta T = 230 \pm 23\mu$K was found in the Very Small Array (VSA) observation at 33 GHz with the scale of about $30 \times 20$ arcmin$^2$ (Génova-Santos et al., 2005, 2008). It is in direction of a known supercluster but with no known galaxy clusters. The same amplitude of decrement occurs in the WMAP5 temperature map (Génova-Santos et al., 2008). The origin of the cold spot is not clear. Observations from the MITO (Millimetre & Infrared Testa Grigia Observatory) telescope inferred that the thermal SZ effect may contribute 25% of the signal (Battistelli et al., 2006). Recent studies using gas-dynamical simulations conclude that the thermal SZ effect from Warm Hot Intergalactic Medium (WHIM) is much smaller. The kinetic SZ effect of the supercluster is also negligible (Flores-Cacho et al., 2009). From our simulation, it seems also unlikely that the ISWRS effect can give rise to temperature decrement of such a large amplitude, if we assume that the supercluster is to contribute most of the ISWRS signal along that direction. If we assume the convergence flow of matter in the supercluster region is comparable to that of our simulation, then the temperature decrement given by non-linearity can just be the order of a few $\mu$K. Even without the cancellation of the linear ISW effect, they can at most contribute a few percent of the total temperature decrement found in these observations.

## 4.6 Conclusion and discussion

Our aim was to fully investigate the gravitational effect that CMB photons suffer when passing through the evolving non-linear gravitational potential, $\Phi$, of intervening large-scale structure. We have developed a method of using large cosmological N-body simulations to compute the time derivative of the potential, $\dot{\Phi}$, along the past lightcone of an observer. By integrating along light rays we have created full sky maps, both using the full non-linear calculation of $\dot{\Phi}$ and an alternative in which the dark matter velocity field is assumed to be related to its density field by the normal linear theory relation. By comparing the results of the two calculations we were able to fully assess the linear Integrated Sachs-Wolfe (ISW) and non-linear Rees-Sciama (RS) contributions to the induced CMB temperature fluctuations.

In general, in a $\Lambda$CDM universe, the linear ISW effect is dominant at low redshift where the accelerating expansion, driven by dark energy, causes the decay of perturbations in the gravitational potential. The propagation of CMB photons through these decaying potential wells/hills produces hot/cold regions of the order of $10\mu$K on scales of hundreds of Mpc. At low redshift the non-linear (RS) effect produces only small scale perturbations to this large-scale pattern. However with increasing redshift the RS contribution decreases in amplitude much more slowly than does the contribution from the ISW effect, which vanishes as $\Omega_{\rm m}(z)$ approaches unity. Hence the importance and scale of the RS effect becomes larger at higher redshift, confirming Cai et al. (2009b) and Smith et al. (2009). We have shown that the origin of the RS effect is dominated by the non-linear relation between the velocity and density field rather than the non-linearity of the density field itself.[6] Our investigation of the RS effect has revealed three distinct non-linear phenomena that give rise to corresponding characteristic features in the temperature perturbation maps.

- Dipoles are produced by the transverse motion of large lumps of dark matter, with typical sizes of tens of Mpc, much larger than the scale of galaxy clusters.

- Convergent flows, on the scale of up to $100h^{-1}$Mpc, around non-linear overdense regions give rise to cold spots of order $\mu$K surrounded by hot filamentary

[6]The fact that to accurately model $\dot{\Phi}$ and the growth of large-scale structure requires more accurate modelling of the large-scale velocity field than is provided by linear theory may suggest that using redshift space distortions to measure the growth rate of density perturbations, $\beta$, may also not be sufficiently accurate.

shells. At high redshift these can be strong enough to dominate over the linear ISW effect and change the sign of the temperature perturbation centred on overdense regions.

- Divergent flows around void regions are characterised by RS contributions consisting of hot rings around cold central regions, where the density contrast of the void is nearly saturated ($\delta \approx -1$). This is a small effect at low redshift, but acts to strengthen the cold spots produced by the linear ISW effect.

Unfortunately none of these effects can easily be detected individually. At low redshift these phenomena make only 10% changes to the temperature perturbations predicted by the linear ISW effect. At very high redshift they are completely dominant, but their amplitudes are very low. We find they contribute to cold spots of comparable physical scale to those reported in the literature, but their amplitudes are many times smaller.

It may be possible to detect these large-scale features induced by the non-linear velocity field by employing stacking techniques. The detectability of RS kinematic features produced by merging clusters has been discussed by Rubiño-Martín et al. (2004) and Maturi et al. (2007b). They conclude that around a thousand clusters would be needed to detected the RS signal. This is due to having to overcome the contaminating effects of the kSZ effect and possibly lensing. However we have found imprints of the RS perturbations on scales of a few tens of Mpc, much larger than the merging cluster scale, and with slightly larger amplitudes. Thus these large-scale features might be more easily detected, requiring the coaddition of less objects.

From our all sky maps we find that the RS contributions to the overall power spectrum of temperature perturbations becomes important for $l > 80$ (a few degrees) and completely dominates for $l > 200$. At still smaller scales the kinetic SZ effect is expected to dominate and at such scales a full treatment would have to incorporate additional modelling of this contribution. The RS contribution to the temperature maps is strongly non-gaussian with a skewed one-point distribution. In future work it will be interesting to investigate the RS contribution to higher order statistics as its non-gaussian characteristics might limit the ability to detect primordial non-Gaussianity in the underlying primary CMB fluctuations. Combining our full sky maps with mock galaxy catalogues built from the same N-body simulations (Baugh et al. in prep.) will be a powerful tool for developing cross-correlations techniques

aimed at extracting the ISWRS signal.

# Chapter 5 | *Conclusions*

The theoretical work in this thesis lays the ground work for constraining dark energy using the next generation of galaxy redshift surveys. We have used state-of-the-art N-body simulations and semi-analytic models of galaxy formation to explore the linear and non-linear ISW effect arising from large-scale structure, and to make accurate all-sky maps of these effects for the first time. This ground work and extensions of it are needed in order to be able to determine primordial and secondary non-Gaussian signatures in the CMB for example, and to constrain the dark energy by cross-correlating galaxy samples from real surveys with the CMB.

In Chapter 2 we developed a method for constructing mock photo-$z$ galaxy surveys from the Bower06 semi-analytic model of galaxy formation. Because the model galaxy luminosity function is a good match to the observations all the way to high redshift, we are able to make realistic predictions for the PS1 survey for the galaxy number counts and the galaxy redshift distributions for each of PS1 bands. We have used the mock galaxy catalogues to investigate the likely photo-$z$ performance of PS1. We find using PS1 data alone, a photo-$z$ accuracy of $\Delta z/(1+z) \sim 0.06$ is achievable over some redshift intervals. Significant improvements in accuracy can be achieved by selecting a red galaxy sub-sample, or by adding near infrared data. We investigated how these photo-$z$ errors reduce the accuracy with which one can constrain the scale of Baryon Acoustic Oscillations. We showed that their effect was equivalent to a significant reduction in the effective volume of the survey. Despite this, the PS1 survey depth and area, covering 3/4 of the sky, mean that the survey will provide better constraints on the dark energy than any previous survey.

In Chapters 3 & 4, we disentangled the linear and non-linear ISW effects in a $\Lambda$CDM universe. Understanding these effects is crucial for the interpretation of future ISW cross-correlation measurements and to constrain the other causes of CMB secondary fluctuations.

In Chapter 3 we discovered that the non-linear ISW effect becomes important at larger and larger scales with increasing redshift. This can be seen in both the

power spectrum of $\dot{\Phi}$, and in the cross-correlation of large-scale structure with the CMB. The sign of the cross-correlation becomes negative once the non-linear effect dominates. This will affect the ISW cross-correlation measurements at high redshift, where it causes a 5-10% supression of the linear signal. It may also affect SZ measurements.

In Chapter 4 we developed a method to construct full-sky maps of the ISWRS effect by ray-tracing through simulations. We have used the maps to explore in detail the physics of the non-linear ISW effect. The non-linear ISW effect has the opposite sign to the linear ISW effect in cluster regions, and the same sign, thus boosting the linear effect, in the centres of voids. The size of these regions are found to be of order of 100 Mpc. At smaller scales, the maps reveal dipoles of cold and hot spots associated with the transverse bulk motion of matter to the line of sight. All of these non-linear effects are weak in amplitude, but the dipole effect might be detectable via its distinct spatial signature. We conclude that the total effect of ISW and RS cannot generate the extreme CMB cold spots found in observations.

## 5.1 Final words

Understanding the mystery of dark energy is the main goal of the upcoming generation of surveys in astronomy. To be able to obtain tight constraints on the equation of state of dark energy, we need to bring observational systematics down to the percent level. We have to recognise that our current understanding of photo-$z$ performance is incomplete: firstly the various methods of photo-$z$ determination perform differently (Abdalla et al., 2008); secondly, the non-Gaussian distribution of photo-$z$ errors, and the presence of catastrophic errors in photo-$z$ measurements, all need to be taken into consideration when interpreting galaxy survey data. It seems unlikely to expect a single method or a single dataset alone will lead to a significant breakthrough in the understanding of dark energy. Rather various probes, all of which are likely to suffer from different kinds of systematics, will need to be combined in order to make progress by breaking parameter degeneracies. Cross-checks from different data sets and using different statistical methods will be important.

The epoch of cosmological tomography has been opened up by the combinations of large and deep galaxy surveys, SZ surveys and other surveys of the inter-galactic medium. In terms of techniques and methods, weak lensing tomography, the galaxy

power spectrum and the BAO, redshift space distortions, the halo mass function and ISW effect are all powerful probes of some aspects. This thesis has addressed a few of these, but has mainly focused on the ISW effect from a theoretical perspective. The non-Gaussian aspect of the non-linear ISW effect, which will be an important contaminant to primordial CMB non-Gaussianity, has not been fully addressed. One approach to tackle this is to investigate the higher-order statistics of our simulated sky maps. Another important area for future study is the influence of photo-$z$ errors on the ISW cross-correlation measurements for real surveys.

Finally, using galaxy surveys, one cannot hope to probe much further than the epoch of reionization. The epoch of reionization occurs at $z \sim 11$ according to the WMAP5 polarisation measurements (Komatsu et al., 2008), when the universe is about half a billion years old. Between recombination and the first stars there is the so-called dark age. This epoch is in principle observable via the emission and absorption of the 21-cm line of neutral hydrogen. This is another exciting frontier where we are eagerly expecting observational data. Earlier still, the universe before the epoch of recombination may be probed via the neutrino background and gravitational waves, which may be possible in the more distant future.

# Appendix A | *Angular Power Spectra*

Here we derive the relationship between the 3-D power spectrum of gravitational potential fluctuations, $P_{\dot{\Phi}\dot{\Phi}}(k,t) = (2\pi)^{-3}\langle\dot{\Phi}(k,t)\dot{\Phi}^*(k,t)\rangle$ and the resulting angular power spectrum of the induced CMB temperature fluctuations. Expanding the pattern of temperature fluctuations, $\Delta T(\hat{r})/\bar{T}_0$, in terms of spherical harmonics we have

$$a_{lm} = \int \frac{\Delta T(\hat{r})}{\bar{T}_0}\, Y^*_{lm}(\hat{r})\, d\hat{r} \tag{A.1}$$

which using equation (3.1) becomes

$$a_{lm} = \frac{2}{c^2}\int Y^*_{lm}(\hat{r}) \int_0^{t_L} \dot{\Phi}(\hat{r},t)\, dt\, d\hat{r}. \tag{A.2}$$

Writing $\dot{\Phi}(\hat{r},t)$ in terms of a Fourier expansion and using the spherical harmonic expansion of a plane wave, $\exp(i\vec{k}\cdot\vec{r}) = 4\pi\sum_{lm} i^l j_l(kr)Y^*_{lm}(\hat{k})Y_{lm}(\hat{r})$ this becomes

$$\begin{aligned} a_{lm} &= \frac{2}{(2\pi)^3 c^2}\int Y^*_{lm}(\hat{r}) \int_0^{t_L}\int \dot{\Phi}(\vec{k},t)\exp(i\vec{k}\cdot\vec{r})d\vec{k}dtd\hat{r} \\ &= \frac{2\times 4\pi}{(2\pi)^3 c^2}\int Y^*_{lm}(\hat{r}) \int_0^{t_L}\int \dot{\Phi}(\vec{k},t)\times \\ &\quad \sum_{l'm'} i^l j_l(kr)Y^*_{l'm'}(\hat{k})Y_{l'm'}(\hat{r})\, d\vec{k}\, dt\, d\hat{r} \\ &= \frac{1}{\pi^2 c^2}\int_0^{t_L}\int \dot{\Phi}(\vec{k},t) i^l j_l(kr)Y^*_{lm}(\hat{k})\, d\vec{k}\, dt. \end{aligned} \tag{A.3}$$

Hence the angular power spectrum, $C_l$, is given by

$$\begin{aligned} C_l\,\delta_{ll'}\delta_{mm'} &\equiv \langle a_{lm}a^*_{l'm'}\rangle \\ &= \left[\frac{1}{\pi^2 c^3}\right]^2 \Big\langle \int_0^{r_L} a \int \dot{\Phi}(\vec{k},r) i^l j_l(kr)Y^*_{lm}(\hat{k})\, d\vec{k}\, dr \\ &\quad \times \int_0^{r_L}\int a'\dot{\Phi}^*(\vec{k}',r') i^{l'} j_l(k'r')Y_{l'm'}(\hat{k}')d\vec{k}'dr'\Big\rangle. \end{aligned} \tag{A.4}$$

Using the identity $\left\langle \dot{\Phi}(\vec{k})\dot{\Phi}^*(\vec{k}')\right\rangle \equiv (2\pi)^3\delta(\vec{k}-\vec{k}')P_{\dot{\Phi}\dot{\Phi}}(k)$ and the orthogonality relationship of spherical harmonics

$$\int_{4\pi} Y^*_{lm}(\hat{r})Y_{l'm'}(\hat{r})\, d\hat{r} = \delta_{ll'}\delta_{mm'} \tag{A.5}$$

this becomes

$$\begin{aligned} C_l\,\delta_{ll'}\delta_{mm'} &= \frac{8}{\pi c^6}\frac{2}{\pi}\int\int_0^{r_L}\int_0^{r_L} aa' P_{\dot\Phi\dot\Phi}(k,r,r') i^l j_l(kr) Y^*_{lm}(\hat k) \\ &\quad \times i^{l'} j_l(kr') Y_{l'm'}(\hat k)\, dr'\, dr\, d\vec{k} \\ &= \frac{8}{\pi c^6}\int\int_0^{r_L}\int_0^{r_L} k^2 P_{\dot\Phi\dot\Phi}(k,r,r') j_l(kr) j_l(kr') dr' dr dk \delta_{ll'}\delta_{mm'} \\ C_l &= \frac{8}{\pi c^6}\int\int_0^{r_L}\int_0^{r_L} aa' k^2 P_{\dot\Phi\dot\Phi}(k,r,r') j_l(kr) j_l(kr') dr' dr dk. \end{aligned} \tag{A.6}$$

This exact relationship can be simplified by using Limber's approximation. For small angular separations, $\theta$, at comoving distance, $r$, the wave number, $k$, can be expressed in terms of its components parallel and perpendicular to the line-of-sight and approximated by $k = \sqrt{k_\parallel^2 + k_\perp^2} \approx k_\perp$, where $k_\perp = 2\pi/r\theta \approx l/r \gg k_\parallel \sim 1/\Delta r$, namely, the power is dominated by that perpendicular to the line-of-sight and there is no correlation between different shells of $\Delta r$ along the line-of-sight. Combining this with the orthogonality relation for spherical Bessel functions,

$$\frac{2}{\pi}\int k^2 j_l(kr) j_l(kr') dk = \delta(r-r')/r^2, \tag{A.7}$$

we arrive at

$$C_l \approx \frac{4}{c^6}\int_0^{r_L} a^2 P_{\dot\Phi\dot\Phi}\left(k = \frac{l}{r}, r\right)/r^2 dr. \tag{A.8}$$

(see also Limber, 1954; Kaiser, 1992; Hu, 2000; Verde et al., 2000).

# Bibliography

F. B. Abdalla, A. Amara, P. Capak, and et al. Photometric redshifts for weak lensing tomography from space: the role of optical and near infrared photometry. MNRAS, 387:969–986, July 2008.

N. Afshordi, Y.-S. Loh, and M. A. Strauss. Cross-correlation of the cosmic microwave background with the 2MASS galaxy survey: Signatures of dark energy, hot gas, and point sources. Phys. Rev. D, 69(8):083524–+, April 2004.

N. Aghanim, S. Prunet, O. Forni, and F. R. Bouchet. Moving gravitational lenses: imprints on the cosmic microwave background. A&A, 334:409–419, June 1998.

C. Almeida, C. M. Baugh, and C. G. Lacey. The structural and photometric properties of early-type galaxies in hierarchical models. MNRAS, 376:1711–1726, April 2007.

L. Amendola, C. Quercellini, and E. Giallongo. Constraints on perfect fluid and scalar field dark energy models from future redshift surveys. MNRAS, 357:429–439, February 2005.

R. E. Angulo, C. M. Baugh, C. S. Frenk, and C. G. Lacey. The detectability of baryonic acoustic oscillations in future galaxy surveys. MNRAS, 383:755–776, January 2008.

J. V. Arnau, M. J. Fullana, and D. Saez. Great Attractor-Like Structures and Largescale Anisotropy. MNRAS, 268:L17+, May 1994.

O. Aso, M. Hattori, and T. Futamase. The Gravitational Scattering of the Cosmic Microwave Background by Dark Clusters of Galaxies. ApJ, 576:L5–L7, September 2002.

R. B. Barreiro, P. Vielva, C. Hernandez-Monteagudo, and E. Martinez-Gonzalez. A Linear Filter to Reconstruct the ISW Effect From CMB and LSS Observations. *IEEE Journal of Selected Topics in Signal Processing, vol. 2, issue 5, pp. 747-754*, 2:747–754, October 2008.

E. S. Battistelli, M. De Petris, L. Lamagna, R. A. Watson, R. Rebolo, F. Melchiorri, R. Génova-Santos, G. Luzzi, and et al. Millimeter Observation of the SZ Effect in the Corona Borealis Supercluster. ApJ, 645:826–834, July 2006.

C. M. Baugh. A primer on hierarchical galaxy formation: the semi-analytical approach. *Reports of Progress in Physics*, 69:3101–3156, December 2006.

C. M. Baugh, S. Cole, and C. S. Frenk. Evolution of the Hubble sequence in hierarchical models for galaxy formation. MNRAS, 283:1361–1378, December 1996.

C. M. Baugh and G. Efstathiou. The Three-Dimensional Power Spectrum Measured from the APM Galaxy Survey - Part One - Use of the Angular Correlation Function. MNRAS, 265:145–+, November 1993.

C. M. Baugh, C. G. Lacey, C. S. Frenk, G. L. Granato, L. Silva, A. Bressan, A. J. Benson, and S. Cole. Can the faint submillimetre galaxies be explained in the $\Lambda$ cold dark matter model? MNRAS, 356:1191–1200, January 2005.

R. Bender, I. Appenzeller, and A. Böhm. The FORS Deep Field: Photometric Data and Photometric Redshifts. *in Cristiani S., Renzini A., Williams R. E., eds, Deep Fields. Springer, Berlin*, page 96, 2001.

N. Benítez. Bayesian Photometric Redshift Estimation. ApJ, 536:571–583, June 2000.

A. J. Benson, C. S. Frenk, C. M. Baugh, S. Cole, and C. G. Lacey. The effects of photoionization on galaxy formation - III. Environmental dependence in the luminosity function. MNRAS, 343:679–691, August 2003.

R. Bielby, T. Shanks, U. Sawangwit, S. M. Croom, N. P. Ross, and D. A. Wake. Photometric Selection of Emission Line Galaxies, Clustering Analysis and a Search for the ISW effect. *ArXiv e-prints*, February 2009.

R. M. Bielby and T. Shanks. Anomalous SZ contribution to three-year WMAP data. MNRAS, 382:1196–1202, December 2007.

M. Birkinshaw and S. F. Gull. A test for transverse motions of clusters of galaxies. Nature, 302:315–317, March 1983.

J. Blaizot, I. Szapudi, S. Colombi, T. Budavàri, F. R. Bouchet, J. E. G. Devriendt, B. Guiderdoni, J. Pan, and A. Szalay. GALICS - V: Low- and high-order clustering in mock Sloan Digital Sky Surveys. MNRAS, 369:1009–1020, July 2006.

J. Blaizot, Y. Wadadekar, B. Guiderdoni, S. T. Colombi, E. Bertin, F. R. Bouchet, J. E. G. Devriendt, and S. Hatton. MoMaF: the Mock Map Facility. MNRAS, 360:159–175, June 2005.

C. Blake and S. Bridle. Cosmology with photometric redshift surveys. MNRAS, 363: 1329–1348, November 2005.

C. Blake and K. Glazebrook. Probing Dark Energy Using Baryonic Oscillations in the Galaxy Power Spectrum as a Cosmological Ruler. ApJ, 594:665–673, September 2003.

M. R. Blanton, D. W. Hogg, N. A. Bahcall, J. Brinkmann, M. Britton, A. J. Connolly, I. Csabai, M. Fukugita, and et al. The Galaxy Luminosity Function and Luminosity Density at Redshift z = 0.1. ApJ, 592:819–838, August 2003.

M. Bolzonella, J.-M. Miralles, and R. Pelló. Photometric redshifts based on standard SED fitting procedures. A&A, 363:476–492, November 2000.

L. Boubekeur, P. Creminelli, G. D'Amico, J. Noreña, and F. Vernizzi. Sachs-Wolfe at second order: the CMB bispectrum on large angular scales. *ArXiv e-prints*, June 2009.

O. Boulade, X. Charlot, P. Abbon, and et al. MegaCam: the new Canada-France-Hawaii Telescope wide-field imaging camera. In M. Iye and A. F. M. Moorwood, editors, *Instrument Design and Performance for Optical/Infrared Ground-based Telescopes. Edited by Iye, Masanori; Moorwood, Alan F. M. Proceedings of the SPIE, Volume 4841, pp. 72-81 (2003).*, volume 4841 of *Presented at the Society of Photo-Optical Instrumentation Engineers (SPIE) Conference*, pages 72–81, March 2003.

R. Bouwens and J. Silk. Models of Disk Evolution: Confrontation with Observations. ApJ, 568:522–538, April 2002.

R. G. Bower, A. J. Benson, R. Malbon, J. C. Helly, C. S. Frenk, C. M. Baugh, S. Cole, and C. G. Lacey. Breaking the hierarchy of galaxy formation. MNRAS, 370:645–655, August 2006.

R. J. Brunner, A. S. Szalay, and A. J. Connolly. Evolution in the Clustering of Galaxies for Z<1.0. ApJ, 541:527–534, October 2000.

A. G. Bruzual and S. Charlot. Spectral evolution of stellar populations using isochrone synthesis. ApJ, 405:538–553, March 1993.

G. Bruzual and S. Charlot. Stellar population synthesis at the resolution of 2003. MNRAS, 344:1000–1028, October 2003.

A. Cabré, E. Gaztañaga, M. Manera, and et al. Cross-correlation of Wilkinson Microwave Anisotropy Probe third-year data and the Sloan Digital Sky Survey DR4 galaxy survey: new evidence for dark energy. MNRAS, 372:L23–L27, October 2006.

Y.-C. Cai, R. E. Angulo, C. M. Baugh, S. Cole, C. S. Frenk, and A. Jenkins. Mock galaxy redshift catalogues from simulations: implications for Pan-STARRS1. MNRAS, 395:1185–1203, May 2009a.

Y.-C. Cai, S. Cole, A. Jenkins, and C. Frenk. Towards accurate modelling of the integrated Sachs-Wolfe effect: the non-linear contribution. MNRAS, 396:772–778, June 2009b.

L. Cao, Y.-Q. Chu, and L.-Z. Fang. Cross-correlation between WMAP and 2MASS: non-Gaussianity induced by the SZ effect. MNRAS, 369:645–654, June 2006.

K. C. Chambers. Mission Concept Statement for PS1. *Pan-STARRS Mission Concept Statement for PS1*, 23000200, December 2006.

A. L. Coil, J. A. Newman, N. Kaiser, M. Davis, C.-P. Ma, D. D. Kocevski, and D. C. Koo. Evolution and Color Dependence of the Galaxy Angular Correlation Function: 350,000 Galaxies in 5 Square Degrees. ApJ, 617:765–781, December 2004.

S. Cole, S. Hatton, D. H. Weinberg, and C. S. Frenk. Mock 2dF and SDSS galaxy redshift surveys. MNRAS, 300:945–966, November 1998.

S. Cole, C. G. Lacey, C. M. Baugh, and C. S. Frenk. Hierarchical galaxy formation. MNRAS, 319:168–204, November 2000.

S. Cole, P. Norberg, C. M. Baugh, C. S. Frenk, J. Bland-Hawthorn, T. Bridges, R. Cannon, G. Dalton, and et al. The 2dF galaxy redshift survey: near-infrared galaxy luminosity functions. MNRAS, 326:255–273, September 2001.

S. Cole, W. J. Percival, J. A. Peacock, P. Norberg, C. M. Baugh, C. S. Frenk, I. Baldry, J. Bland-Hawthorn, and et al. The 2dF Galaxy Redshift Survey: power-spectrum analysis of the final data set and cosmological implications. MNRAS, 362:505–534, September 2005.

S. Cole, A. G. Sánchez, and S. Wilkins. The Galaxy Power Spectrum: 2dFGRS-SDSS Tension? In N. Metcalfe and T. Shanks, editors, *Cosmic Frontiers*, volume 379 of *Astronomical Society of the Pacific Conference Series*, pages 57–+, December 2007.

G. D. Coleman, C.-C. Wu, and D. W. Weedman. Colors and magnitudes predicted for high redshift galaxies. ApJS, 43:393–416, July 1980.

M. Colless, G. Dalton, S. Maddox, and et al. The 2dF Galaxy Redshift Survey: spectra and redshifts. MNRAS, 328:1039–1063, December 2001.

A. A. Collister and O. Lahav. ANNz: Estimating Photometric Redshifts Using Artificial Neural Networks. PASP, 116:345–351, April 2004.

A. J. Connolly, I. Csabai, A. S. Szalay, D. C. Koo, R. G. Kron, and J. A. Munn. Slicing Through Multicolor Space: Galaxy Redshifts from Broadband Photometry. AJ, 110:2655–+, December 1995.

A. Cooray. Non-Gaussian aspects of thermal and kinetic Sunyaev-Zel'dovich effects. Phys. Rev. D, 64(6):063514–+, August 2001.

A. Cooray. Integrated Sachs-Wolfe effect: Large scale structure correlation. Phys. Rev. D, 65(10):103510–+, April 2002a.

A. Cooray. Nonlinear integrated Sachs-Wolfe effect. Phys. Rev. D, 65(8):083518–+, April 2002b.

A. Cooray and N. Seto. Did the Wilkinson Microwave Anisotropy Probe see moving local structures? *Journal of Cosmology and Astro-Particle Physics*, 12:4–+, December 2005.

E. J. Copeland, M. Sami, and S. Tsujikawa. Dynamics of Dark Energy. *International Journal of Modern Physics D*, 15:1753–1935, 2006.

M. Crocce and R. Scoccimarro. Renormalized cosmological perturbation theory. Phys. Rev. D, 73(6):063519–+, March 2006.

D. J. Croton, V. Springel, S. D. M. White, and et al. The many lives of active galactic nuclei: cooling flows, black holes and the luminosities and colours of galaxies. MNRAS, 365:11–28, January 2006.

M. Cruz, L. Cayón, E. Martínez-González, P. Vielva, and J. Jin. The Non-Gaussian Cold Spot in the 3 Year Wilkinson Microwave Anisotropy Probe Data. ApJ, 655: 11–20, January 2007.

M. Cruz, E. Martínez-González, P. Vielva, and L. Cayón. Detection of a non-Gaussian spot in WMAP. MNRAS, 356:29–40, January 2005.

M. Cruz, M. Tucci, E. Martínez-González, and P. Vielva. The non-Gaussian cold spot in WilkinsonMicrowaveAnisotropyProbe: significance, morphology and foreground contribution. MNRAS, 369:57–67, June 2006.

I. Csabai, T. Budavári, A. J. Connolly, A. S. Szalay, Z. Győry, N. Benítez, J. Annis, J. Brinkmann, and et al. The Application of Photometric Redshifts to the SDSS Early Data Release. AJ, 125:580–592, February 2003.

Y. Dabrowski, M. P. Hobson, A. N. Lasenby, and C. Doran. Microwave background anisotropies and non-linear structures - II. Numerical computations. MNRAS, 302: 757–770, February 1999.

M. Davis, G. Efstathiou, C. S. Frenk, and S. D. M. White. The evolution of large-scale structure in a universe dominated by cold dark matter. ApJ, 292:371–394, May 1985.

G. De Lucia, V. Springel, S. D. M. White, D. Croton, and G. Kauffmann. The formation history of elliptical galaxies. MNRAS, 366:499–509, February 2006.

J. M. Diego, J. Silk, and W. Sliwa. The Sunyaev-Zel'dovich effect contribution to WMAP: a cross-correlation between WMAP and ROSAT. MNRAS, 346:940–948, December 2003.

D. Dolney, B. Jain, and M. Takada. Baryon oscillations and dark-energy constraints from imaging surveys. MNRAS, 366:884–898, March 2006.

N. Drory, R. Bender, G. Feulner, U. Hopp, C. Maraston, J. Snigula, and G. J. Hill. The Munich Near-Infrared Cluster Survey. II. The K-Band Luminosity Function of Field Galaxies to z ˜ 1.2. ApJ, 595:698–711, October 2003.

G. Efstathiou, S. Moody, J. A. Peacock, and et al. Evidence for a non-zero $\Lambda$ and a low matter density from a combined analysis of the 2dF Galaxy Redshift Survey and cosmic microwave background anisotropies. MNRAS, 330:L29–L35, February 2002.

D. J. Eisenstein, I. Zehavi, D. W. Hogg, and et al. Detection of the Baryon Acoustic Peak in the Large-Scale Correlation Function of SDSS Luminous Red Galaxies. ApJ, 633:560–574, November 2005.

Z. Fan and T. Chiueh. Determining the Geometry and the Cosmological Parameters of the Universe through Sunyaev-Zeldovich Effect Cluster Counts. ApJ, 550:547–553, April 2001.

A. E. Firth, O. Lahav, and R. S. Somerville. Estimating photometric redshifts with artificial neural networks. MNRAS, 339:1195–1202, March 2003.

I. Flores-Cacho, J. A. Rubiño-Martín, G. Luzzi, R. Rebolo, M. De Petris, G. Yepes, L. Lamagna, S. De Gregori, and et al. The Sunyaev-Zeldovich effect in superclusters of galaxies using gasdynamical simulations: the case of Corona Borealis. *ArXiv e-prints*, August 2009.

P. Fosalba and E. Gaztañaga. Measurement of the gravitational potential evolution from the cross-correlation between WMAP and the APM Galaxy Survey. MNRAS, 350:L37–L41, May 2004.

P. Fosalba, E. Gaztañaga, and F. J. Castander. Detection of the Integrated Sachs-Wolfe and Sunyaev-Zeldovich Effects from the Cosmic Microwave Background-Galaxy Correlation. ApJ, 597:L89–L92, November 2003.

M. J. Francis, G. F. Lewis, and E. V. Linder. Halo mass functions in early dark energy cosmologies. MNRAS, 393:L31–L35, February 2009.

M. Fukugita, N. Yasuda, J. Brinkmann, J. E. Gunn, Ž. Ivezić, G. R. Knapp, R. Lupton, and D. P. Schneider. Spatial Variations of Galaxy Number Counts in the Sloan Digital Sky Survey. I. Extinction, Large-Scale Structure, and Photometric Homogeneity. AJ, 127:3155–3160, June 2004.

M. J. Fullana, D. Saez, and J. V. Arnau. On the microwave background anisotropy produced by Great Attractor-like structures. ApJS, 94:1–16, August 1994.

A. Gabasch, R. Bender, S. Seitz, and et al. The evolution of the luminosity functions in the FORS Deep Field from low to high redshift. I. The blue bands. A&A, 421: 41–58, July 2004.

R. Génova-Santos, J. A. Rubiño-Martín, R. Rebolo, R. A. Battye, F. Blanco, R. D. Davies, R. J. Davis, T. Franzen, and et al. Observations of the Corona Borealis supercluster with the superextended Very Small Array:. MNRAS, 391:1127–1136, December 2008.

R. Génova-Santos, J. A. Rubiño-Martín, R. Rebolo, K. Cleary, R. D. Davies, R. J. Davis, C. Dickinson, N. Falcón, and et al. A Very Small Array search for the extended Sunyaev-Zel'dovich effect in the Corona Borealis supercluster. MNRAS, 363:79–92, October 2005.

E. Giallongo, S. D'Odorico, A. Fontana, S. Cristiani, E. Egami, E. Hu, and R. G. McMahon. The Photometric Redshift Distribution and Evolutionary Properties of Galaxies up to Z ˜ 4.5 in the Field of the Quasar BR 1202-0725. AJ, 115: 2169–2183, June 1998.

T. Giannantonio and R. Crittenden. The effect of reionization on the cosmic microwave background-density correlation. MNRAS, 381:819–826, October 2007.

F. Giovi, C. Baccigalupi, and F. Perrotta. Constraining the dark energy dynamics with the cosmic microwave background bispectrum. Phys. Rev. D, 68(12):123002–+, December 2003.

K. M. Górski, E. Hivon, A. J. Banday, B. D. Wandelt, F. K. Hansen, M. Reinecke, and M. Bartelmann. HEALPix: A Framework for High-Resolution Discretization

and Fast Analysis of Data Distributed on the Sphere. ApJ, 622:759–771, April 2005.

G. L. Granato, C. G. Lacey, L. Silva, and et al. The Infrared Side of Galaxy Formation. I. The Local Universe in the Semianalytical Framework. ApJ, 542:710–730, October 2000.

B. R. Granett, M. C. Neyrinck, and I. Szapudi. Dark Energy Detected with Supervoids and Superclusters. *ArXiv e-prints*, 805, May 2008.

B. R. Granett, M. C. Neyrinck, and I. Szapudi. A Map of the Integrated Sachs-Wolfe Signal from Luminous Red Galaxies. ApJ, 701:414–422, August 2009.

L. I. Gurvits and I. G. Mitrofanov. Perturbation of the background radiation by a moving gravitational lens. Nature, 324:349–350, November 1986.

S. Hatton, J. E. G. Devriendt, S. Ninin, F. R. Bouchet, B. Guiderdoni, and D. Vibert. GALICS- I. A hybrid N-body/semi-analytic model of hierarchical galaxy formation. MNRAS, 343:75–106, July 2003.

J. C. Helly, S. Cole, C. S. Frenk, C. M. Baugh, A. Benson, C. Lacey, and F. R. Pearce. A comparison of gas dynamics in smooth particle hydrodynamics and semi-analytic models of galaxy formation. MNRAS, 338:913–925, February 2003.

P. C. Hewett, S. J. Warren, S. K. Leggett, and S. T. Hodgkin. The UKIRT Infrared Deep Sky Survey ZY JHK photometric system: passbands and synthetic colours. MNRAS, 367:454–468, April 2006.

G. Hinshaw, J. L. Weiland, R. S. Hill, and et al. Five-Year Wilkinson Microwave Anisotropy Probe (WMAP) Observations: Data Processing, Sky Maps, and Basic Results. *ArXiv e-prints*, 803, March 2008.

R. W. Hockney and J. W. Eastwood. *Computer Simulation Using Particles*. 1981.

W. Hu. Reionization Revisited: Secondary Cosmic Microwave Background Anisotropies and Polarization. ApJ, 529:12–25, January 2000.

W. Hu and S. Dodelson. Cosmic Microwave Background Anisotropies. ARA&A, 40: 171–216, 2002.

W. Hu and Z. Haiman. Redshifting rings of power. Phys. Rev. D, 68(6):063004–+, September 2003.

J.-S. Huang, K. Glazebrook, L. L. Cowie, and C. Tinney. The Hawaii+Anglo-Australian Observatory K-Band Galaxy Redshift Survey. I. The Local K-Band Luminosity Function. ApJ, 584:203–209, February 2003.

K. T. Inoue and J. Silk. Local Voids as the Origin of Large-Angle Cosmic Microwave Background Anomalies. I. ApJ, 648:23–30, September 2006.

K. T. Inoue and J. Silk. Local Voids as the Origin of Large-Angle Cosmic Microwave Background Anomalies: The Effect of a Cosmological Constant. ApJ, 664:650–659, August 2007.

A. Jenkins, C. S. Frenk, S. D. M. White, J. M. Colberg, S. Cole, A. E. Evrard, H. M. P. Couchman, and N. Yoshida. The mass function of dark matter haloes. MNRAS, 321:372–384, February 2001.

N. Kaiser. Weak gravitational lensing of distant galaxies. ApJ, 388:272–286, April 1992.

X. Kang, Y. P. Jing, H. J. Mo, and G. Börner. Semianalytical Model of Galaxy Formation with High-Resolution N-Body Simulations. ApJ, 631:21–40, September 2005.

X. Kang, Y. P. Jing, and J. Silk. Massive and Red Objects Predicted by a Semianalytical Model of Galaxy Formation. ApJ, 648:820–825, September 2006.

E. Komatsu, J. Dunkley, M. R. Nolta, and et al. Five-Year Wilkinson Microwave Anisotropy Probe (WMAP) Observations: Cosmological Interpretation. *ArXiv e-prints, 0803.0547*, March 2008.

C. G. Lacey, C. M. Baugh, C. S. Frenk, L. Silva, G. L. Granato, and A. Bressan. Galaxy evolution in the infrared: comparison of a hierarchical galaxy formation model with Spitzer data. MNRAS, 385:1155–1178, April 2008.

A. N. Lasenby, C. J. L. Doran, M. P. Hobson, Y. Dabrowski, and A. D. Challinor. Microwave background anisotropies and non-linear structures - I. Improved theoretical models. MNRAS, 302:748–756, February 1999.

A. Lawrence, S. J. Warren, O. Almaini, A. C. Edge, N. C. Hambly, R. F. Jameson, P. Lucas, M. Casali, and et al. The UKIRT Infrared Deep Sky Survey (UKIDSS). MNRAS, 379:1599–1617, August 2007.

R. Lieu, J. P. D. Mittaz, and S.-N. Zhang. The Sunyaev-Zel'dovich Effect in a Sample of 31 Clusters: A Comparison between the X-Ray Predicted and WMAP Observed Cosmic Microwave Background Temperature Decrement. ApJ, 648:176–199, September 2006.

D. N. Limber. The Analysis of Counts of the Extragalactic Nebulae in Terms of a Fluctuating Density Field. II. ApJ, 119:655–+, May 1954.

E. V. Linder. Baryon oscillations as a cosmological probe. Phys. Rev. D, 68(8): 083504–+, October 2003.

M. Loverde, L. Hui, and E. Gaztañaga. Magnification-temperature correlation: The dark side of integrated Sachs-Wolfe measurements. Phys. Rev. D, 75(4):043519–+, February 2007.

A. V. Macciò, C. Quercellini, R. Mainini, L. Amendola, and S. A. Bonometto. Coupled dark energy: Parameter constraints from N-body simulations. Phys. Rev. D, 69(12):123516–+, June 2004.

R. K. Malbon, C. M. Baugh, C. S. Frenk, and C. G. Lacey. Black hole growth in hierarchical galaxy formation. MNRAS, 382:1394–1414, December 2007.

A. Mangilli and L. Verde. Non-Gaussianity and the CMB Bispectrum: confusion between Primordial and Lensing-Rees Sciama contribution? *ArXiv e-prints*, June 2009.

E. Martinez-Gonzalez and J. L. Sanz. CMB Anisotropies Generated by Cosmic Voids and Great Attractors. MNRAS, 247:473–478, December 1990.

E. Martinez-Gonzalez, J. L. Sanz, and J. Silk. Anisotropies in the microwave sky due to nonlinear structures. ApJ, 355:L5–L9, May 1990.

I. Masina and A. Notari. The cold spot as a large void: lensing effect on CMB two and three point correlation functions. *Journal of Cosmology and Astro-Particle Physics*, 7:35–+, July 2009a.

I. Masina and A. Notari. The cold spot as a large void: Rees-Sciama effect on CMB power spectrum and bispectrum. *Journal of Cosmology and Astro-Particle Physics*, 2:19–+, February 2009b.

M. Maturi, K. Dolag, A. Waelkens, V. Springel, and T. Enßlin. The actual Rees-Sciama effect from the local universe. A&A, 476:83–88, December 2007a.

M. Maturi, T. Enßlin, C. Hernández-Monteagudo, and J. A. Rubiño-Martín. A linear-filter approach to extracting the Rees-Sciama effect in merging clusters of galaxies. A&A, 467:411–419, May 2007b.

M. Maturi, T. Ensslin, C. Hernandez-Monteagudo, and J. A. Rubino-Martin. Galaxy cluster merger kinematics by Rees-Sciama effect. *ArXiv Astrophysics e-prints*, February 2006.

J. D. McEwen, M. P. Hobson, A. N. Lasenby, and D. J. Mortlock. A high-significance detection of non-Gaussianity in the Wilkinson Microwave Anisotropy Probe 1-yr data using directional spherical wavelets. MNRAS, 359:1583–1596, June 2005.

J. D. McEwen, M. P. Hobson, A. N. Lasenby, and D. J. Mortlock. A high-significance detection of non-Gaussianity in the WMAP 3-yr data using directional spherical wavelets. MNRAS, 371:L50–L54, September 2006.

J. D. McEwen, M. P. Hobson, A. N. Lasenby, and D. J. Mortlock. A high-significance detection of non-Gaussianity in the WMAP 5-yr data using directional spherical wavelets. MNRAS, 388:659–662, August 2008.

J. D. McEwen, P. Vielva, M. P. Hobson, and et al. Detection of the integrated Sachs-Wolfe effect and corresponding dark energy constraints made with directional spherical wavelets. MNRAS, 376:1211–1226, April 2007.

S. Mei and J. G. Bartlett. Cosmological constraints from a 2D SZ catalog. A&A, 425:1–8, October 2004.

B. Mobasher, P. Capak, N. Z. Scoville, and et al. Photometric Redshifts of Galaxies in COSMOS. ApJS, 172:117–131, September 2007.

S. M. Molnar and M. Birkinshaw. Contributions to the Power Spectrum of Cosmic Microwave Background from Fluctuations Caused by Clusters of Galaxies. ApJ, 537:542–554, July 2000.

S. M. Molnar and M. Birkinshaw. Determining Tangential Peculiar Velocities of Clusters of Galaxies Using Gravitational Lensing. ApJ, 586:731–734, April 2003.

A. D. Myers, T. Shanks, P. J. Outram, W. J. Frith, and A. W. Wolfendale. Evidence for an extended Sunyaev-Zel'dovich effect in WMAP data. MNRAS, 347:L67–L72, February 2004.

A. J. Nishizawa, E. Komatsu, N. Yoshida, R. Takahashi, and N. Sugiyama. Cosmic Microwave Background-Weak Lensing Correlation: Analytical and Numerical Study of Nonlinearity and Implications for Dark Energy. ApJ, 676:L93–L96, April 2008.

P. Norberg, S. Cole, C. M. Baugh, C. S. Frenk, I. Baldry, J. Bland-Hawthorn, T. Bridges, R. Cannon, and et al. The 2dF Galaxy Redshift Survey: the $b_J$-band galaxy luminosity function and survey selection function. MNRAS, 336:907–931, November 2002.

N. Padmanabhan, C. M. Hirata, U. Seljak, and et al. Correlating the CMB with luminous red galaxies: The integrated Sachs-Wolfe effect. Phys. Rev. D, 72(4): 043525–+, August 2005.

M. Panek. Cosmic background radiation anisotropies from cosmic structures - Models based on the Tolman solution. ApJ, 388:225–233, April 1992.

J. A. Peacock and S. J. Dodds. Reconstructing the Linear Power Spectrum of Cosmological Mass Fluctuations. MNRAS, 267:1020–+, April 1994.

W. J. Percival, C. M. Baugh, J. Bland-Hawthorn, and et al. The 2dF Galaxy Redshift Survey: the power spectrum and the matter content of the Universe. MNRAS, 327:1297–1306, November 2001.

W. J. Percival, S. Cole, D. J. Eisenstein, R. C. Nichol, J. A. Peacock, A. C. Pope, and A. S. Szalay. Measuring the Baryon Acoustic Oscillation scale using the Sloan Digital Sky Survey and 2dF Galaxy Redshift Survey. MNRAS, 381:1053–1066, November 2007.

S. Perlmutter, G. Aldering, M. della Valle, S. Deustua, R. S. Ellis, S. Fabbro, A. Fruchter, G. Goldhaber, D. E. Groom, I. M. Hook, A. G. Kim, M. Y. Kim, R. A.

Knop, C. Lidman, R. G. McMahon, P. Nugent, R. Pain, N. Panagia, C. R. Pennypacker, P. Ruiz-Lapuente, B. Schaefer, and N. Walton. Discovery of a supernova explosion at half the age of the universe. Nature, 391:51–+, January 1998.

V. Petrosian. Surface brightness and evolution of galaxies. ApJ, 209:L1–L5, October 1976.

L. Pozzetti, A. Cimatti, G. Zamorani, E. Daddi, N. Menci, A. Fontana, A. Renzini, M. Mignoli, and et al. The K20 survey. V. The evolution of the near-IR Luminosity Function. A&A, 402:837–848, May 2003.

N. Puchades, M. J. Fullana, J. V. Arnau, and D. Sáez. On the Rees-Sciama effect: maps and statistics. MNRAS, 370:1849–1858, August 2006.

V. Quilis, J. M. Ibanez, and D. Saez. Galaxy clusters and microwave background anisotropy. MNRAS, 277:445–454, November 1995.

V. Quilis and D. Saez. Secondary gravitational anisotropies in open universes. MNRAS, 293:306–+, January 1998.

A. Raccanelli, A. Bonaldi, M. Negrello, and et al. A reassessment of the evidence of the Integrated Sachs-Wolfe effect through the WMAP-NVSS correlation. *ArXiv e-prints*, 802, February 2008.

A. Rassat, K. Land, O. Lahav, and et al. Cross-correlation of 2MASS and WMAP 3: implications for the integrated Sachs-Wolfe effect. MNRAS, 377:1085–1094, May 2007.

D. S. Reed, R. Bower, C. S. Frenk, A. Jenkins, and T. Theuns. The halo mass function from the dark ages through the present day. MNRAS, 374:2–15, January 2007.

M. J. Rees and D. W. Sciama. Larger scale Density Inhomogeneities in the Universe. Nature, 217:511–+, February 1968.

A. G. Riess, A. V. Filippenko, P. Challis, and et al. Observational Evidence from Supernovae for an Accelerating Universe and a Cosmological Constant. AJ, 116: 1009–1038, September 1998.

A. G. Riess, L.-G. Strolger, J. Tonry, S. Casertano, H. C. Ferguson, B. Mobasher, P. Challis, A. V. Filippenko, S. Jha, W. Li, R. Chornock, R. P. Kirshner, B. Leibundgut, M. Dickinson, M. Livio, M. Giavalisco, C. C. Steidel, T. Benítez, and Z. Tsvetanov. Type Ia Supernova Discoveries at z¿1 from the Hubble Space Telescope: Evidence for Past Deceleration and Constraints on Dark Energy Evolution. ApJ, 607:665–687, June 2004.

J. A. Rubiño-Martín, C. Hernández-Monteagudo, and T. A. Enßlin. Measuring dark matter flows in merging clusters of galaxies. A&A, 419:439–447, May 2004.

L. Rudnick, S. Brown, and L. R. Williams. Extragalactic Radio Sources and the WMAP Cold Spot. ApJ, 671:40–44, December 2007.

R. K. Sachs and A. M. Wolfe. Perturbations of a Cosmological Model and Angular Variations of the Microwave Background. ApJ, 147:73–+, January 1967.

D. Saez, J. V. Arnau, and M. J. Fullana. The Imprints of the Great-Attractor and the Virgo Cluster on the Microwave Background. MNRAS, 263:681–+, August 1993.

A. G. Sanchez, C. M. Baugh, and R. Angulo. What is the best way to measure baryonic acoustic oscillations? *ArXiv e-prints*, 804, April 2008.

A. G. Sánchez, C. M. Baugh, W. J. Percival, and et al. Cosmological parameters from cosmic microwave background measurements and the final 2dF Galaxy Redshift Survey power spectrum. MNRAS, 366:189–207, February 2006.

A. G. Sánchez and S. Cole. The galaxy power spectrum: precision cosmology from large-scale structure? MNRAS, 385:830–840, April 2008.

A. G. Sanchez, M. Crocce, A. Cabre, C. M. Baugh, and E. Gaztanaga. Cosmological parameter constraints from SDSS luminous red galaxies: a new treatment of large-scale clustering. *ArXiv e-prints*, January 2009.

W. Saunders, C. Frenk, M. Rowan-Robinson, A. Lawrence, and G. Efstathiou. The density field of the local universe. Nature, 349:32–38, January 1991.

M. J. Sawicki, H. Lin, and H. K. C. Yee. Evolution of the Galaxy Population Based on Photometric Redshifts in the Hubble Deep Field. AJ, 113:1–12, January 1997.

U. Seljak. Rees-Sciama Effect in a Cold Dark Matter Universe. ApJ, 460:549–+, April 1996.

H.-J. Seo and D. J. Eisenstein. Probing Dark Energy with Baryonic Acoustic Oscillations from Future Large Galaxy Redshift Surveys. ApJ, 598:720–740, December 2003.

S. Shen, H. J. Mo, S. D. M. White, M. R. Blanton, G. Kauffmann, W. Voges, J. Brinkmann, and I. Csabai. The size distribution of galaxies in the Sloan Digital Sky Survey. MNRAS, 343:978–994, August 2003.

R. E. Smith, C. Hernandez-Monteagudo, and U. Seljak. Impact of Scale Dependent Bias and Nonlinear Structure Growth on the ISW Effect: Angular Power Spectra. *ArXiv e-prints*, May 2009.

D. Sowards-Emmerd, J. A. Smith, T. A. McKay, E. Sheldon, D. L. Tucker, and F. J. Castander. A Catalog of Photometry for Las Campanas Redshift Survey Galaxies on the Sloan Digital Sky Survey System. AJ, 119:2598–2604, June 2000.

V. Springel, S. D. M. White, A. Jenkins, C. S. Frenk, N. Yoshida, L. Gao, J. Navarro, R. Thacker, D. Croton, J. Helly, J. A. Peacock, S. Cole, P. Thomas, H. Couchman, A. Evrard, J. Colberg, and F. Pearce. Simulations of the formation, evolution and clustering of galaxies and quasars. Nature, 435:629–636, June 2005.

M. A. Strauss, D. H. Weinberg, R. H. Lupton, and et al. Spectroscopic Target Selection in the Sloan Digital Sky Survey: The Main Galaxy Sample. AJ, 124: 1810–1824, September 2002.

R. A. Sunyaev and Y. B. Zeldovich. The Observations of Relic Radiation as a Test of the Nature of X-Ray Radiation from the Clusters of Galaxies. *Comments on Astrophysics and Space Physics*, 4:173–+, November 1972.

M. Tegmark, M. R. Blanton, M. A. Strauss, F. Hoyle, D. Schlegel, R. Scoccimarro, M. S. Vogeley, D. H. Weinberg, and et al. The Three-Dimensional Power Spectrum of Galaxies from the Sloan Digital Sky Survey. ApJ, 606:702–740, May 2004a.

M. Tegmark, M. A. Strauss, M. R. Blanton, and et al. Cosmological parameters from SDSS and WMAP. Phys. Rev. D, 69(10):103501–+, May 2004b.

J. Tinker, A. V. Kravtsov, A. Klypin, K. Abazajian, M. Warren, G. Yepes, S. Gottlöber, and D. E. Holz. Toward a Halo Mass Function for Precision Cosmology: The Limits of Universality. ApJ, 688:709–728, December 2008.

K. Tomita and K. T. Inoue. Second order gravitational effects on CMB temperature anisotropy in Λ dominated flat universes. Phys. Rev. D, 77(10):103522–+, May 2008.

I. Trujillo, N. M. Förster Schreiber, G. Rudnick, M. Barden, M. Franx, H.-W. Rix, J. A. R. Caldwell, D. H. McIntosh, and et al. The Size Evolution of Galaxies since z˜3: Combining SDSS, GEMS, and FIRES. ApJ, 650:18–41, October 2006.

R. Tuluie and P. Laguna. The imprint of proper motion of nonlinear structures on the cosmic microwave background. ApJ, 445:L73–L76, June 1995.

R. Tuluie, P. Laguna, and P. Anninos. Cosmic Microwave Background Anisotropies from the Rees-Sciama Effect in $\Omega_0 \leq 1$ Universes. ApJ, 463:15–+, May 1996.

J. A. Tyson. Large Synoptic Survey Telescope: Overview. In J. A. Tyson and S. Wolff, editors, *Survey and Other Telescope Technologies and Discoveries. Edited by Tyson, J. Anthony; Wolff, Sidney. Proceedings of the SPIE, Volume 4836, pp. 10-20 (2002).*, volume 4836 of *Presented at the Society of Photo-Optical Instrumentation Engineers (SPIE) Conference*, pages 10–20, December 2002.

L. Verde, A. F. Heavens, and S. Matarrese. Projected bispectrum in spherical harmonics and its application to angular galaxy catalogues. MNRAS, 318:584–598, October 2000.

L. Verde and D. N. Spergel. Dark energy and cosmic microwave background bispectrum. Phys. Rev. D, 65(4):043007–+, February 2002.

P. Vielva, E. Martínez-González, R. B. Barreiro, J. L. Sanz, and L. Cayón. Detection of Non-Gaussianity in the Wilkinson Microwave Anisotropy Probe First-Year Data Using Spherical Wavelets. ApJ, 609:22–34, July 2004.

M. S. Warren, K. Abazajian, D. E. Holz, and L. Teodoro. Precision Determination of the Mass Function of Dark Matter Halos. ApJ, 646:881–885, August 2006.

S. D. M. White, G. Efstathiou, and C. S. Frenk. The amplitude of mass fluctuations in the universe. MNRAS, 262:1023–1028, June 1993.

S. D. M. White and C. S. Frenk. Galaxy formation through hierarchical clustering. ApJ, 379:52–79, September 1991.

S. D. M. White, R. B. Tully, and M. Davis. Clustering bias in the nearby galaxies catalog and in cold dark matter models. ApJ, 333:L45–L49, October 1988.

N. Yasuda, M. Fukugita, V. K. Narayanan, R. H. Lupton, I. Strateva, M. A. Strauss, Ž. Ivezić, R. S. J. Kim, and et al. Galaxy Number Counts from the Sloan Digital Sky Survey Commissioning Data. AJ, 122:1104–1124, September 2001.

N. Yasuda, M. Fukugita, and D. P. Schneider. Spatial Variations of Galaxy Number Counts in the Sloan Digital Sky Survey. II. Test of Galactic Extinction in High-Extinction Regions. AJ, 134:698–705, August 2007.

D. G. York, J. Adelman, J. E. Anderson, Jr., and et al. The Sloan Digital Sky Survey: Technical Summary. AJ, 120:1579–1587, September 2000.

N. Yoshida, F. Stoehr, V. Springel, and S. D. M. White. Gas cooling in simulations of the formation of the galaxy population. MNRAS, 335:762–772, September 2002.